

Institutsbereich Geophysik, Astrophysik und Meteorologie  
Institut für Physik  
Karl - Franzens - Universität Graz  
Universitätsplatz 5, A-8010 Graz, Austria  
<http://www.uni-graz.at/igam>

W i s s e n s c h a f t l i c h e r   B e r i c h t   No. 20

# Atmosphere and Climate Explorer Mission ACE+: Humidity and Temperature Retrieval Performance Analysis

by  
Susanne Schweitzer

November 2004



Institute for Geophysics, Astrophysics, and Meteorology



Susanne Schweitzer

Atmosphere and Climate Explorer Mission ACE+:  
Humidity and Temperature Retrieval Performance  
Analysis

Diplomarbeit  
zur Erlangung des akademischen Grades einer  
Magistra der Naturwissenschaften

Supervisor:  
Univ.-Prof. Mag. Dr. Gottfried Kirchengast

Institute for Geophysics, Astrophysics, and Meteorology  
Institute of Physics, University of Graz

November 2004



## Acknowledgements

I would like to sincerely thank Prof. Gottfried Kirchengast for enabling and primely supervising this work. Furthermore I would like to thank all people who supported me in doing this work - in particular my family, my S.O. Tobias Kellner and Mag. Michael Borsche.

I would also like to thank all members of the ARSCliSys research group as well as M. Gorbunov (IAP Moscow, Russia) and N. Floury (ESA/ESTEC) for providing various figures included in this work and for their contributions to the EGOPS5 software. Valuable comments from P. Silvestrin, T. Wehr (both ESA/ESTEC), and the ACE+ Mission Advisory Group, which helped the work, are gratefully acknowledged.

The EGOPS5 software, the core tool of the performance analysis, was developed by an international consortium led by IGAM/UniGraz and involving partner teams at the Danish Meteorological Institute (Denmark), the Chalmers University of Technology (Sweden), and the IEP/University of Bremen (Germany). All colleagues in these partner teams are thanked for their contributions. EGOPS5 is based on strong heritage from EGOPS4, which was developed 1996-2003 by a consortium led by IGAM/UniGraz and involving partner teams at the Danish Meteorological Institute and TERMA Elektronik A/S (Denmark), the Met. Office (U.K.), and Austrian Aerospace GmbH (Austria) with the major funding provided by ESA.

The European Centre for Medium-Range Weather Forecasts (ECMWF) is acknowledged for providing atmospheric analyses within the scope of the Special Project "Climate monitoring by advanced spaceborne sounding and atmospheric modeling" of G. Kirchengast.

The major funding for this work and for the development of EGOPS5 was provided by ESA under ESA/ESTEC Contract No. 16743/02/NL/FF (ACEPASS study); funds also came from ESA/ESTEC Contract No. 17479/03/NL/FF (ACECLIM study). Furthermore, the START research award of G. Kirchengast funded by the Austrian Ministry for Education, Science, and Culture, managed under Program No. Y103-N03 of the Austrian Science Fund, partially supported this project.



## Abstract

The radio occultation technique is a promising method for global remote sensing of the earth's atmosphere. A special form of this measurement method is the GNSS-LEO radio occultation technique, which is being applied in many cases in order to determine atmospheric parameters such as pressure, temperature and humidity (GPS/MET, CHAMP, etc.). These parameters are derived from the bending of GNSS signals (1–2 GHz) crossing the atmosphere. One limitation of this technique, however, is an ambiguity between temperature and humidity, which is why in humid regions temperature cannot be retrieved without a-priori knowledge of humidity, and the other way around.

The LEO-LEO radio occultation technique would be able to overcome this limitation because it allows to employ frequencies around the 22 GHz water vapour absorption line. This enables to exploit the absorption of the signal due to water vapour (in addition to the bending) for the determination of atmospheric parameters.

The present work includes an introduction to the LEO-LEO radio occultation technique as well as an overview of the *Atmosphere and Climate Explorer* mission ACE+. The empirical part of this work deals with the assessment of the accuracy of temperature and humidity profiles retrieved from LEO-LEO radio occultation data assuming the ACE+ concept. In order to do this, a set of LEO-LEO radio occultation events has been simulated and evaluated using the *End-to-end Generic Occultation Performance Simulator* EGOPS5 (version E5.0.4r1). The resulting temperature and humidity profiles were compared with the original atmosphere data and statistically analyzed. It was found out that the retrieved profiles of specific humidity agree with the “true” original profiles accurate to about 10% throughout the troposphere. The temperature profiles are found accurate to about 0.5 K throughout the troposphere, and within the stratosphere (up to a height of 30 km) the accuracy is even better. Particularly important, the retrieved profiles are found essentially unbiased thanks to the self-calibrating nature of the radio occultation method. These results emphasize the great capability of the LEO-LEO radio occultation technique for atmosphere and climate science.



## Zusammenfassung

Die Radiookkultationstechnik ist eine vielversprechende Methode zur globalen Fernerkundung der Atmosphäre der Erde. Eine spezielle Form, die GNSS-LEO Radiookkultation, wird und wurde bereits vielfach zur Bestimmung atmosphärischer Parameter wie Druck, Temperatur und Feuchte eingesetzt (GPS/MET, CHAMP, etc.). Die atmosphärischen Parameter werden dabei aus der Brechung von GNSS-Signalen (1–2 GHz) in der Atmosphäre abgeleitet. Diese Methode enthält jedoch intrinsisch eine Ambiguität zwischen Temperatur und Feuchte, weshalb in feuchten Regionen der eine Parameter nicht ohne a-priori-Kennntnis des jeweilig anderen bestimmt werden kann.

Die LEO-LEO Radiookkultation könnte dieser Schwäche Abhilfe schaffen, da sie die Verwendung von Frequenzen um die 22 GHz Wasserdampfabsorptionslinie gestattet, wodurch zusätzlich zur Brechung des Signals in der Atmosphäre auch dessen Absorption durch Wasserdampf zur Bestimmung atmosphärischer Parameter ausgenutzt werden kann.

Die vorliegende Arbeit enthält eine Einführung in die Methode der LEO-LEO Radiookkultation sowie einen Überblick über die Atmosphären- und Klimsatellitenmission ACE+. Der empirische Teil der Arbeit beschäftigt sich mit einer Abschätzung der Genauigkeit von Feuchte- und Temperaturprofilen, wie sie aus LEO-LEO Radiookkultation — unter Annahme des ACE+ Konzeptes — gewonnen werden können. Dafür wurden mithilfe des *End-to-end Generic Occultation Performance Simulators* EGOPS5 (Version E5.0.4r1) eine Reihe von LEO-LEO Radiookkultations-Ereignissen simuliert und ausgewertet. Die resultierenden Temperatur- und Feuchteprofile wurden mit den ursprünglichen atmosphärischen Eingangsdaten verglichen und statistisch analysiert. Es zeigte sich, dass die gewonnenen Profile spezifischer Feuchte bis etwa zur Tropopausenhöhe auf ungefähr 10 % genau mit den “wahren” Eingangsdaten übereinstimmen. Die Temperaturprofile sind in der Troposphäre auf etwa 0.5 K genau und in der Stratosphäre (bis zu einer Höhe von 30 km) ist die mittlere Abweichung sogar noch kleiner. Insbesondere stellte sich heraus, dass die erhaltenen Profile im wesentlichen frei von systematischen Fehlern sind, was auf das Selbstkalibrationsprinzip der Radiookkultationsmethode zurückzuführen ist. Diese Ergebnisse unterstreichen das große Potential der LEO-LEO Radiookkultationstechnik für die Atmosphären- und Klimaforschung.



# Contents

<b>Introduction</b>	<b>1</b>
<b>1 The Earth's Atmosphere</b>	<b>3</b>
1.1 Composition and Structure . . . . .	3
1.1.1 Atmospheric Components . . . . .	3
1.1.2 Vertical Structure . . . . .	6
1.2 The General Circulation . . . . .	8
1.3 Weather and Climate . . . . .	10
<b>2 The LEO-LEO Radio Occultation Technique</b>	<b>15</b>
2.1 History . . . . .	16
2.2 Physical Principles and Retrieval Methodology . . . . .	20
2.2.1 Retrieval of Bending Angle and Transmission . . . . .	21
2.2.2 Retrieval of Real and Imaginary Refractivity . . . . .	26
2.2.3 Retrieval of Atmospheric Profiles . . . . .	28
2.3 Influence of Layered Structures, Clouds and Turbulence . . . . .	31
2.4 Important Properties for Atmosphere and Climate Science . . . . .	34
<b>3 The ACE+ Mission</b>	<b>37</b>
3.1 General Information . . . . .	37
3.2 The Need for ACE+ . . . . .	38
3.3 Scientific Mission Goals . . . . .	40
3.4 Measurement Concept . . . . .	42
3.4.1 Generic System Concept . . . . .	42
3.4.2 Observation Methodology . . . . .	45
3.5 Observational Requirements . . . . .	49

<b>4</b>	<b>ACE+ Performance Analysis Simulations</b>	<b>53</b>
4.1	The Simulation Tool EGOPS5 . . . . .	53
4.2	Modelling and Retrieval Structure of EGOPS5 . . . . .	58
4.2.1	Mission Analysis and Planning . . . . .	58
4.2.2	Forward Modeling . . . . .	59
4.2.3	Observation System Modeling . . . . .	63
4.2.4	Inversion/Retrieval . . . . .	66
4.3	Performance Analysis Setup . . . . .	77
<b>5</b>	<b>Performance Analysis Results and Discussion</b>	<b>87</b>
5.1	Analysis based on Climatological Atmosphere . . . . .	87
5.1.1	Clear Air . . . . .	88
5.1.2	Cloudy and Turbulent Air . . . . .	96
5.2	Analysis based on ECMWF Analysis Field . . . . .	103
5.2.1	High Latitudes . . . . .	103
5.2.2	Mid Latitudes . . . . .	110
5.2.3	Low Latitudes . . . . .	115
5.2.4	Comparison of the Performance at Different Latitudes . . . .	120
	<b>Summary, Conclusions and Outlook</b>	<b>125</b>
<b>A</b>	<b>Sample EGOPS Input Files</b>	<b>127</b>
A.1	ACE+ Constellation Two Line Element (TLE) Files . . . . .	127
A.2	Mission Analysis/Planning Input File . . . . .	127
A.3	Forward Modeling Input File . . . . .	129
A.4	Observation System Modeling Input File . . . . .	130
A.5	Inversion/Retrieval Input File . . . . .	132
	<b>List of Acronyms</b>	<b>135</b>
	<b>List of Tables</b>	<b>139</b>
	<b>List of Figures</b>	<b>141</b>
	<b>Bibliography</b>	<b>145</b>

# Introduction

The Atmosphere and Climate Explorer Mission ACE+ is a project designed for atmospheric sounding using the GNSS-LEO and LEO-LEO radio occultation technique. Proposed for the ESA *Living Planet Programme* it was selected as the top priority future *Earth Explorer Opportunity Mission* in May 2002 by ESA. However, apparently because of programmatic and cost reasons, ACE+ was not proceeded into phase B after the phase A studies 2003–2004. Therefore, ACE+ is in a hibernation status at the moment. Quite possibly, though, there will be opportunities to resume the mission in the near future.

The GNSS-LEO radio occultation technique can be used to determine atmospheric parameters such as pressure, temperature, and humidity with high accuracy, high vertical resolution, and global and even coverage. This method which has already been extensively applied in atmospheric research exploits the information contained within the bending angle of GPS, GALILEO or GLONASS signals crossing the atmosphere in order to derive the atmospheric state. But the results of this technique intrinsically contain an ambiguity between temperature and humidity, which means that humidity cannot be retrieved without a priori knowledge of temperature. And reversely, temperature cannot be accurately retrieved if humidity is unknown.

The LEO-LEO radio occultation — which is performed between two low earth orbiting (LEO) satellites — is able to remedy this ambiguity because it uses somewhat higher frequencies (X/K-band instead of L-band) which are not only refracted but also absorbed by the atmosphere. The additional information from the absorption enables accurate retrieval of temperature and humidity independently from each other and without the use of a priori knowledge, throughout the upper troposphere and down into the lower troposphere.

ACE+ would be the first mission applying the LEO-LEO radio occultation technique. It consists of four satellites circulating in two different low earth orbits which are able to perform occultation measurements on GPS and GALILEO L-band signals as well as on X/K band signals transmitted by the two LEO satellites in the higher orbit. Since the LEO-LEO radio occultation technique has never been put into practice before it is very important to investigate the capabilities of this measurement method in advance, and this work contributes to this investigation.

The main objective of this work is to assess the performance of humidity and tem-

perature retrieval achievable by LEO-LEO radio occultation in the ACE+ satellite constellation under various atmospheric conditions. The core is a statistical performance analysis carried out using the end-to-end radio occultation simulation tool EGOPS5 (version E5.0.4r1) in geometric-optics processing mode. In particular, the performance analysis is composed of two main parts. Both parts deal with the impact of clouds and atmospheric turbulence on the performance of the retrieval of humidity and temperature. The difference is that the first part of the analysis is based on a climatological atmosphere model (CIRA86aQ\_UoG), whereas the second part is based on a quasi-realistic atmospheric field (ECMWF analysis field). The results of the performance analysis contribute to the assessment of the compliance with the ACE+ requirements laid out in the ACE+ Mission Requirements Document [ESA, 2004c]. Furthermore, the results quantitatively illustrate the general potential of the LEO-LEO radio occultation technique.

The analysis presented in this work has been performed in the framework of the ACE+ Phase A Scientific Support (ACEPASS) Study on LEO-LEO Occultation Characterization [Kirchengast et al., 2002b] and is closely coupled to previous studies, in particular [Schweitzer et al., 2003] and [Kirchengast et al., 2004b]. In preparation for the analysis, this work also contains the basics of the atmosphere, a description of the LEO-LEO radio occultation technique as well as an introduction to the ACE+ mission. The general structure of the work is as follows:

As an introduction for the reader not versed in the subject of atmosphere and climate, Chapter 1 gives an overall view of the most important atmospheric properties and an explanation of what we understand as climate. Chapter 2 dives into the subject and illustrates the main characteristics of the LEO-LEO radio occultation technique. After that, an introduction to the Atmosphere and Climate Explorer mission ACE+ including its observation methodology and scientific objectives is given in Chapter 3. Finally, Chapters 4 and 5 deal with the performance analysis itself. The former one describes the structure of the analysis and gives an overview of the simulation tool EGOPS5 which has been used for the analysis. The latter one presents and interprets the results of the performance analysis. At the end of this work (see Summary and Conclusions, p. 125) all results are summarized showing the great importance of the LEO-LEO radio occultation technique in atmosphere and climate science.

# Chapter 1

## The Earth's Atmosphere

The term *atmosphere* originates from the classical Greek words  $\alpha\tau\mu\acute{o}\varsigma$  (atmos) which means vapour, and  $\sigma\varphi\alpha\tilde{\iota}\rho\alpha$  (sphaira) which means sphere. Accordingly, the atmosphere is the gaseous layer surrounding the globe. It is the most variable climate component and contains a myriad of physical and chemical phenomena which interact among themselves. For instance, circulation phenomena are mainly driven by the thermal structure, which is influenced by the global energy budget, which in turn depends, among other things, on the distribution of radiatively active components such as water vapour and carbon dioxide.

Since the atmosphere, which is closely connected with the oceans, is the main reason for the agreeable climate on the earth's surface, highly developed life would be impossible without it. The atmosphere contains various radiatively active molecules, so called greenhouse gases, which let the sun's short-wave radiation pass, but are able to absorb and reradiate the long-wave heat radiation emitted from the earth. This property results in a global warming of the the earth's mean surface temperature by about  $+33^\circ\text{C}$ . Without this so-called greenhouse effect, the earth's mean temperature would be around  $-18^\circ\text{C}$ , too cold for life as we know it from our planet to develop.

The subsequent sections give a short overview of atmospheric basics. In case of deeper interest see, e.g., [Salby, 1996], [Thompson, 1998], [Häckel, 1999], [Andrews, 2000], [Kraus, 2000], and [Schönwiese, 2003], from which the present overview is mainly drawn.

### 1.1 Composition and Structure

#### 1.1.1 Atmospheric Components

The present composition of the earth's atmosphere is a result of outgassing processes combined with biogenic processes. Via volcanoes and fissures, gases — pre-

dominantly water vapour, carbon dioxide and sulphur compounds, but no pure oxygen — escaped from the inside of the earth and joined the primeval atmosphere, the composition of which differed fundamentally from today's. Subsequently, uncombined oxygen was formed mainly by photosynthesis of green plants, where phytoplankton plays the leading role. During millions of years, chemical reactions among the gases themselves as well as with other climate components, above all the oceans, led to the present composition which is presented in Table 1.1.

The atmosphere mainly consists of gases, but also of hydrometeors such as liquid or solid water in clouds and precipitation as well as aerosols. Aerosols are liquid and solid substances suspended in the air which do not contain water, e.g., small organic particles like pollen and anorganic particles such as dust or salt crystals. Concerning the gaseous component, main constituents can be distinguished from trace constituents. The main gases are nitrogen ( $N_2$ ), oxygen ( $O_2$ ), and argon (Ar) which together make up 99.96 % of dry air. The remaining 0.04 % consist of miscellaneous trace species: spatially and temporally constant gases (hydrogen ( $H_2$ ) and the chemical inert gases neon (Ne), helium (He), krypton (Kr), xenon (Xe)) as well as spatially and temporally variable gases (e.g., carbon dioxide ( $CO_2$ ), methane ( $CH_4$ ), nitrous oxide ( $N_2O$ ), ozone ( $O_3$ ), chlorofluorocarbons (CFC's)). Water vapour, which characterizes moist air, also belongs to the group of variable gases.

Even though trace gases only occur in small quantities, most of them play an important role in climatic, meteorological, and chemical processes. For instance, the global energy balance of the earth is highly influenced by the radiation properties of a lot of trace species. Other components which are not radiatively active themselves are able to form climate-active trace gases through chemical reactions.

Water vapour is the most important trace species in the earth's atmosphere. Its concentration decreases steadily with altitude due to the increasing remoteness from water sources on the earth's surface (oceans, etc.) and because colder air aloft forces water vapour to condensate. Moreover, the temperature inversion at the tropopause hinders the exchange between troposphere and stratosphere. Therefore, water vapour is mainly confined to the troposphere. Its horizontal concentration varies temporally and spatially between 0.1 % (cold, dry polar air) and 4 % (hot, humid equatorial air). The mean value close to the surface amounts to 2.6 %. The reasons for the variability lie on the one hand in global and regional temperature differences and the associated moisture capacity (the amount of water vapour which can be held grows exponentially with increasing temperature), and on the other hand in the distribution of land and sea masses. A further reason is the relatively short atmospheric residence time of water vapour of about 10 days.

Since water is the single atmospheric constituent which can appear in all three different physical states (solid, liquid, and gaseous), it is highly important for the climatology: together with the temperature distribution, it drives the atmospheric circulation and maintains the water balance (hydrological cycle). Furthermore, it is

Constituent	Symbol	Molar mass [kg kmol <sup>-1</sup> ]	Tropospheric mixing ratio	Lifetime
<i>Main constituents</i>				
Nitrogen	N <sub>2</sub>	28.02	0.7808	10 <sup>7</sup> yr
Oxygen	O <sub>2</sub>	32.01	0.2095	10 <sup>5</sup> yr
Argon	Ar	39.95	0.0093	> 10 <sup>3</sup> yr
<i>Trace Constituents</i> (spatially and temporally constant)				
Neon	Ne	20.18	18.18 ppm	> 10 <sup>3</sup> yr
Helium	He	4.00	5.24 ppm	> 10 <sup>3</sup> yr
Krypton	Kr	83.80	1.14 ppm	> 10 <sup>3</sup> yr
Hydrogen	H <sub>2</sub>	2.02	0.52 ppm	2 yr
Xenon	Xe	131.30	0.09 ppm	> 10 <sup>3</sup> yr
<i>Trace Constituents</i> (mainly selection of radiatively active gases; variable up to highly variable)				
Carbon dioxide	CO <sub>2</sub>	44.02	370 ppm <sup>1)</sup>	5–15 yr <sup>2)</sup>
Methane	CH <sub>4</sub>	16.04	1.75 ppm <sup>1)</sup>	15 yr
Nitrous oxide	N <sub>2</sub> O	44.01	0.31 ppm <sup>1)</sup>	120 yr
Carbon monoxide	CO	28.01	50–100 ppb	60 d
Ozone	O <sub>3</sub>	48.00		
Stratosphere			5–10 ppm	30–150 d
Close to the surface			15–50 ppb <sup>1)</sup>	< 4 m
Nitrogen oxides			0.5–5 ppb	~ 1 d
Nitrogen monoxide	NO	30.00		
Nitrogen dioxide	NO <sub>2</sub>	46.01		
Sulphur dioxide	SO <sub>2</sub>	64.06	0.2–4 ppb	1–4 d
Chlorofluorocarbons				
CFC-12	CCl <sub>2</sub> F <sub>2</sub>	120.91	~ 0.5 ppb	100–150 yr
CFC-11	CCl <sub>3</sub> F	137.37	~ 0.3 ppb	50 yr
CFC-22	CHClF <sub>2</sub>	86.47	~ 0.1 ppb	13 yr

<sup>1)</sup> Concentration is rising, the given values date from 2000.

<sup>2)</sup> This value cannot be given in a consistent way, e.g., the anthropogenic share of CO<sub>2</sub> has a lifetime of about 50–200 years.

Table 1.1: Atmospheric composition close to the surface (adapted from [Reuter, 2001], complemented by [Schönwiese, 2003]). The given values are valid for aerosol-free and water vapour-free air. Usually, the tropospheric water vapour mixing ratio varies between 0.1 % and 4 %, the mean value near surface amounts to 2.6 %; the mean values of N<sub>2</sub>, O<sub>2</sub>, and Ar of moist air are 76.06 %, 20.40 %, and 0.91 %, respectively.

the most important greenhouse gas. Water vapour participates in most atmospheric processes, but nevertheless (or just because of that), its climatic mechanisms are poorly understood. Long-term accurate measurements of the global distribution of water vapour and connected state variables, which can be provided by radio occultation measurements, can help to comprehend these mechanisms.

### 1.1.2 Vertical Structure

The total mass of the earth's atmosphere amounts to  $5.1 \cdot 10^{18}$  kg. Whereas its lower limit is clearly determined by the earth's surface and the oceans, the outer limit of the atmosphere is practically impossible to define. But the balance of the gravitational pull and the centrifugal force of the earth's rotation in a height of approximately 32,000 km above the sea level is one useful value. In practice, the exobase level at about 500 km is an other useful value. There, the gas is so dilute, that the mean free path between collisions of molecules is larger than a scale height. For climate and meteorology even the mesopause near 85 km, below which 99.999 % of the air are contained, is often a sufficiently high boundary.

Mainly due to the gravity, the global mean values of pressure and density diminish approximately exponentially with increasing altitude. While the pressure amounts to 1013 hPa ( $\equiv$ 1013 mbar) at the surface, there is only half the surface pressure in a height of 5.5 km, 10 % in 16 km and a mere 1 % in a height of 32 km. Accordingly (because of the hydrostatic balance), the lower 16 km contain about 90 %, the lower 32 km even contain 99 % of the total atmospheric mass.

The vertical structure of the atmosphere (Fig. 1.1) can be seen from three different points of view: from the mixing properties of its components, the temperature behaviour and the electric charge. On the part of the mixing, the homosphere ( $\sim$ 0–100 km) can be distinguished from the heterosphere ( $\sim$ 100–500 km) and the exosphere (above  $\sim$ 500 km). The homosphere (or turbosphere) is marked by a nearly constant mixing ratio with an average molecular weight  $\overline{M}$  of  $28.96 \text{ g mol}^{-1}$ . That is why it is also called the *well mixed* region. The reason for this homogeneous distribution of constituents is the turbulence being the determining transport process within this region. In the heterosphere, the gases are stratified according to their molecular weight, so the number of heavier components decreases more rapidly with altitude than the number of lighter ones. Hence, the composition changes upwards and  $\overline{M}$  diminishes monotonically with altitude. This behaviour is a consequence of the molecular diffusion which is the dominating transport process there. The transition zone between turbulent and diffusive transport where  $\overline{M}$  is still constant is called homopause (or turbopause) and lies about 100 km above the surface. The exosphere represents the junction between the atmosphere and the interplanetary space. Its air density is very low, therefore the mean free path of molecules is very long, greater than the local scale height. Thus the molecules have great velocities, some of them — fortunately a minority — are fast enough

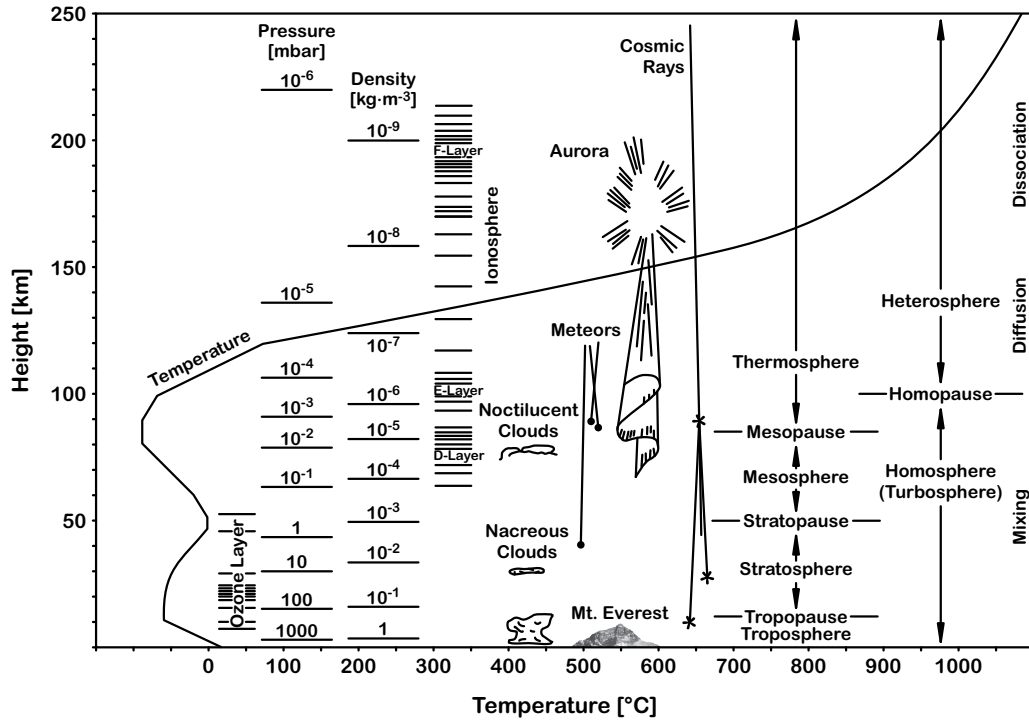


Figure 1.1: Vertical structure of the atmosphere (after [Liljequist and Cehak, 1984]).

to escape the earth's gravitational field (the earth's escape velocity amounts to  $\sim 11 \text{ km s}^{-1}$ ) and get lost in deep space.

Regarding the thermal properties, the four well-known zones troposphere, stratosphere, mesosphere, and thermosphere can be separated. The borders between the different regions are not equally sharp and the vertical extension of the layers varies with the seasons and the geographical latitude. So the upper tropospheric boundary can reach up to  $\sim 17 \text{ km}$  over the equator whereas in polar regions, it is found at a height of  $\sim 8 \text{ km}$ . Within the troposphere, temperature decreases with elevation due to the increasing remoteness from the earth's surface heating at a mean lapse-rate of  $6.5 \text{ K km}^{-1}$ . The troposphere is the region where all weather processes take place and it is characterized by convective overturning. The stratosphere lies above the tropopause and reaches up to the stratopause at a height of  $\sim 50 \text{ km}$ . In its lower part (up to  $\sim 30 \text{ km}$ ), isothermal conditions are dominant whereas in the upper part, temperature increases due to the formation of ozone. The temperature reaches a maximum at the stratopause. Contrary to the troposphere, stratospheric behaviour is controlled by radiative processes; vertical motions are weak. Within the mesosphere, temperature decreases once again up to the mesopause (in a height of  $\sim 85 \text{ km}$ ), where temperature is nearly constant. Convective motions and radiative processes are of equal importance in mesospheric

regions. According to its thermal properties, the uppermost zone is called thermosphere. It is characterized by a temperature increasing steadily with height up to about 300 km which is mainly caused by the absorption of UV radiation by molecular oxygen. From 300 km upwards, a nearly isothermal region extends up into the exosphere, controlled by a balance of eUV (extreme ultra-violet) heating and cooling by downward heat flux divergence.

The third way to split the atmosphere into layers is based on the electric charge of the air. In particular, the neutrosphere can be distinguished from the ionosphere and the protonosphere. The neutrosphere, which mainly contains electrically neutral molecules, extends from the earth's surface up to a height of about 80 km. The ionosphere lies above it and reaches up to 1000–2000 km. It is characterized by electrically charged atoms and molecules. The protonosphere borders on the upper ionospheric boundary and mainly comprises  $H^+$  protons.

Furthermore, back towards the surface, the peplosphere (from the classical Greek word πέπλος (peplos) which means mantle), where air motion is strongly influenced by the frictional force of the earth's surface, can be distinguished from the free atmosphere where movements are mainly driven by the pressure force and the coriolis force. The peplosphere is more commonly known as the *atmospheric boundary layer* and refers to the lower 1–2.5 km of the atmosphere where turbulent motions are predominant.

## 1.2 The General Circulation

The general circulation comprises all atmospheric motions maintaining the thermal equilibrium of the earth. It is connected to the oceanic circulation, together with which it controls transfers of heat, atmospheric constituents, and momentum. Therefore it plays a central role in weather and climate. The interaction between atmosphere and oceans is achieved through processes such as transfers of latent heat and moisture.

The general circulation is driven essentially by two forces: the pressure gradient force which is mainly caused by the meridionally varying radiation balance and the coriolis force which depends on the earth's rotation. The frictional force caused by the earth's surface counteracts to these two forces.

The main function of the general circulation is to even out thermal imbalances between equatorial and polar latitudes, which are due to different insolation. Because of various circumstances, low latitudes get more solar radiation than the terrestrial radiation they emit; whereas in middle and high latitudes, just the opposite is true. Consequently, low latitudes heat up whereas middle and high latitudes cool off. Thus air masses are distributed unequally around the earth which leads to an imbalance of horizontal pressure forces. That is why meridional overturning, with

air rising at low latitudes and flowing to and sinking at middle and high latitudes, develops to level out the imbalances. But on account of the coriolis force induced by the earth's rotation, the meridional air flows are deflected into zonal directions. Thus, basic air motion systems develop which characterize the earth's atmosphere and cause its horizontal stratification.

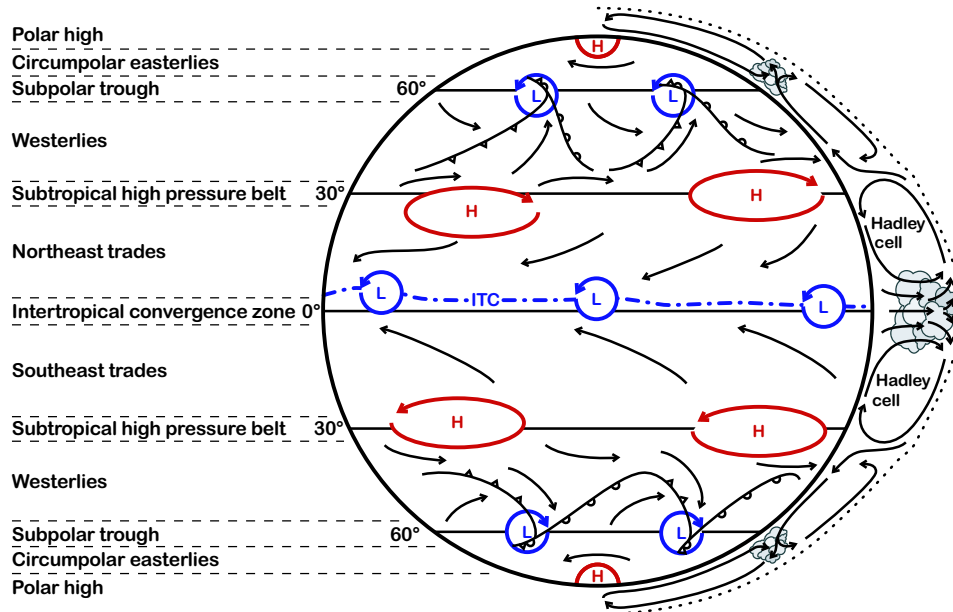


Figure 1.2: Scheme of the general circulation and resulting horizontal structure of the atmosphere. Idea taken from [Roedel, 2000] and [von Storch, H. et al., 1999].

The atmospheric circulation forms typical patterns which are shown in Fig. 1.2. Generally, zones of low and high pressure can be distinguished which are separated through circulation cells. The distribution of the individual areas on the northern hemisphere is the same as on the southern hemisphere. In particular, the following structures are discernible: because of surplus heat in equatorial regions, air rises and leaves the *equatorial trough of low-pressure* near the surface. Whilst the air that has risen is transported polewards with the *anti-trades*, it is deflected eastwards by the coriolis force. In latitudes between  $25^\circ$  and  $35^\circ$ , air-masses sink to the ground, where the so called *subtropical high pressure zone* develops. From there, the majority of the air flows back to the equator with the *trade winds*, deflected westwards by the coriolis force. Thus, the connected *Hadley cell* circulation is closed. Because the trade-winds of southern and northern hemisphere meet near the equator, the equatorial trough is associated with the *inter-tropical convergence zone* which is characterized by rising air with heavy clouds and rain. In contrast, the high pressure on the descending limb of the Hadley cell does not allow clouds, which is why corresponding subtropical latitudes are very arid. Moreover, jet streams build up on both sides of the Hadley cell in the upper troposphere — the easterly jet-streams in equatorial regions and the westerly subtropical jet-streams in the subtropics.

In middle latitudes, the *zone of west winds* borders on the subtropical highs. It is marked by high westerlies, in particular the polar jet-streams aloft. The vertical cell-circulation, which is sometimes called Ferrel cell (it has no real identity, it is purely a statistical feature), is only weakly developed and the airflow is mainly zonal. That is why meridional temperature balance is made difficult. Consequently, the *polar front* evolves as a barrier between the warm subtropical and the cold polar air, which in turn leads to an unstable airflow and further to cyclogenesis. The resulting cyclones and anticyclones support the meridional energy transport. Because the lows are mainly gathered along the polar front they form the *subpolar trough*, a convergence zone which lies between latitude  $55^\circ$  and  $65^\circ$ .

In polar regions, the *polar high pressure* develops since the radiation balance is negative there. As a result, near the surface, easterlies diverge outwards, whereas westerlies can be found aloft. These winds are part of the *polar cell*. Because the coriolis force is very strong at these latitudes, motions are strongly zonal and the meridional mass transport happens only through asymmetries in the instantaneous circulation, which either cause warm air to be deflected polewards or cold air equatorwards.

The circulation patterns described above represent the ideal situation. In reality, the atmospheric circulation is more complex. For example, the distribution of land and sea masses as well as high mountains, conditions of ice and snow and the oceanic circulation take influence. Therefore, the zonal distribution is more homogenous on the southern than on the northern hemisphere. Equally important, the seasonal variation affects the intensity of atmospheric pressure patterns resulting in poleward shifting during summer and opposite shifting during winter; zones at low latitudes are shifted more than zones at high latitudes. Additionally, a lot of subscaled circulation mechanisms overlap the global circulation, which further complicate the situation.

### 1.3 Weather and Climate

The weather is the instantaneous, local state of the atmosphere changing continuously. It is mainly driven by surface heating which is why virtually all weather phenomena occur in the troposphere. Generally, the weather is characterized by meteorological elements like atmospheric pressure, temperature, water vapour pressure, and the horizontal wind vector. These five elements are the central physical variables determining the atmospheric state. Furthermore, there are parameters which can be computed by the variables mentioned above (e.g., air density and the vertical wind component), and also variables describing additional factors (e.g., solar radiation, clouds, precipitation, aerosol, and trace gases).

Broadly speaking, the term climate refers to the entirety of the climate system's properties [Hantel, 2001]. The climate system contains all climatic processes and

comprises the following subsystems (*climate components*): the atmosphere, the hydrosphere (all kinds of water), the cryosphere (all kinds of ice), the biosphere (flora and fauna), the geosphere or pedosphere (the earth's surface down to the ground water based on the lithosphere; the earth's crust), and the anthroposphere (human influences). Of course, these components interact with each other which is the cause for the complexity of the system. In the narrower sense, climate represents the average state (at least monthly averages) of the meteorological elements. The characteristic atmospheric features of specific regions (on the local, regional, and global scale) are tried to be described by means of statistical methods. In this connection, mainly the mean value and the variability of atmospheric parameters are of interest; these are computed over periods ranging from a month over years and decades up to thousands and millions of years, depending on the aspect in consideration.

The climate is not a static entity, but varies slowly. In general, *climate variability* is distinguished from *climate change*. The former refers to fluctuations in the average state of climatic parameters which can occur on all spatial and temporal scales which go beyond the scales of weather events. The latter denotes statistically significant variations in either the average state or the variability of the climate which last a long time (typically decades and more). Both climate variability and climate change are caused on the one hand by internal interactions of the climate components and on the other hand by modifications in external radiative forcings. In this connection, internal forcing means changes due to ordinary influences which basically occur due to the difference in radiative heating between low and high latitudes. On the contrary, external forcing is caused by anomalous influences such as changes of the solar constant, volcanic eruptions, and variations in the concentration of greenhouse gases. Traditionally, the reasons for external forcings originate mainly from natural sources, but anthropogenic sources become more and more important.

In the tide of the earth's history, the climate changed often, but the last 1000 years were climatically quite stable. This stability, however, could be endangered in the next decades — there is more and more evidence that the climate is changing. The clearest signs for a change appear in the atmosphere, the most variable climate component. For instance, the global mean surface temperature and the atmospheric water vapour content are increasing, whereas stratospheric temperatures tend to decrease. According to the IPCC 2001 report [Houghton et al., 2001], the global mean surface temperature increased by  $0.6 \pm 0.2^\circ$  during the twentieth century. In comparison, temperature variations over the last millennium ranged within about half a degree. Concerning the last century, the IPCC 2001 concluded that the global warming was, up to the fifties, mainly determined by natural processes such as solar and internal climate variability. But the warming in the second half of this period cannot be explained without a contribution from the increasing amount of greenhouse gases due to human activity (see Fig. 1.3). In the future, the increase of the global mean surface temperature is estimated to be between  $1.4^\circ$  and  $5.8^\circ$

until 2100 and the atmospheric water vapour content is projected to rise by 5% until 2020.

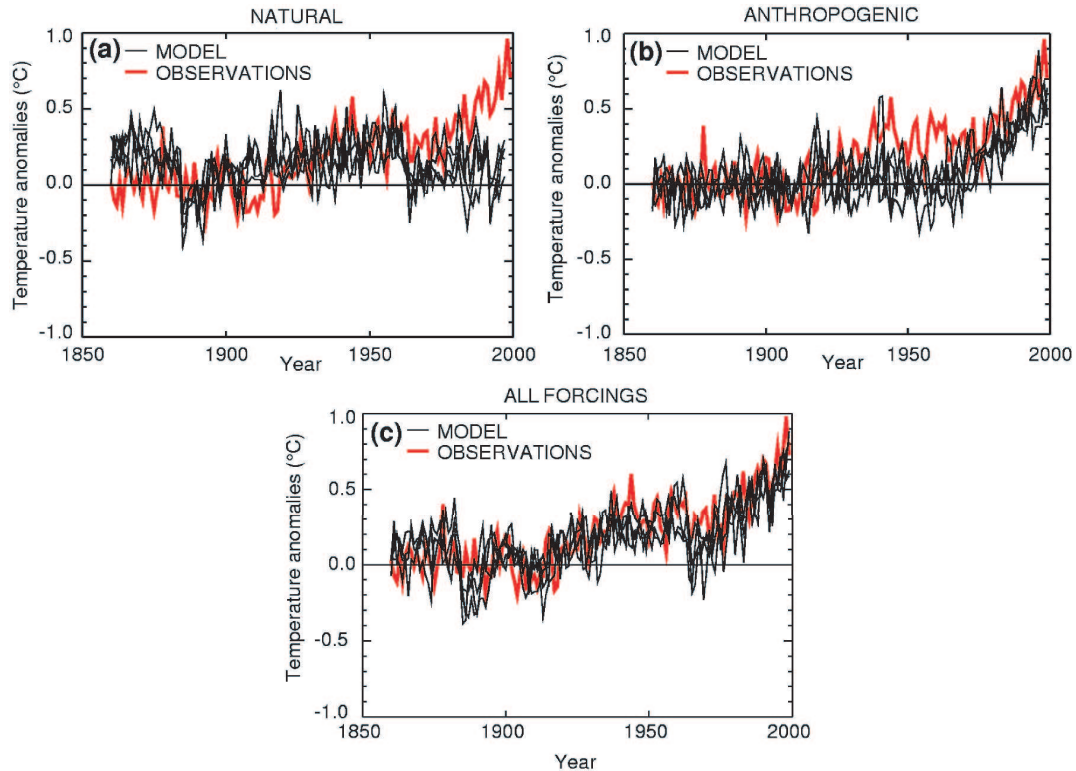


Figure 1.3: Measured changes of the global-mean near surface temperature from 1880–2000 compared with temperature simulations using climate models. The red, heavy line indicates the temperature observation, the black light lines stem from model simulations with different forcings. The simulations in panel (a) were done with only natural forcings (solar variation, volcanic activity). Those encompassed in panel (b) were done with anthropogenic forcings (greenhouse gases, sulphate aerosols). Those shown in panel (c) were done with both natural and anthropogenic forcings included. Panel (a) compared to (b) shows that anthropogenic forcings provide a plausible explanation for the more recent changes of the observed temperature. The best match of simulations with observations is obtained in (c) when both forcings are included. Source: [Houghton et al., 2001].

Humidity concentration and the atmospheric temperature field are coupled by dynamics and thermodynamics. Consequently, an increase of temperature results in more evaporation, which multiplies the atmospheric water vapour content, which in turn boosts the warming. But other effects like the cloud and ice albedo perhaps partly compensating the warming are amplified as well by global warming. This example shows the complexity of the water vapour's role in climatic processes; the so-called *humidity feedback* may amplify or attenuate other climate forcings [Harriss, 1997]. Unfortunately, these humidity feedbacks are poorly understood, not

least because traditional measurement methods of temperature and humidity are insufficient regarding accuracy and global coverage. The GNSS-LEO and LEO-LEO radio occultation could fulfil the need for adequate measurements by establishing accurate climatologies of humidity and temperature which figure centrally in climate research.



## Chapter 2

# The LEO-LEO Radio Occultation Technique

The radio occultation technique is a powerful remote sensing method, which can be used in numerous disciplines, for instance in atmosphere and climate physics, in ionosphere physics, in space physics, in geodesy, and in physical oceanography. Occultation techniques in general are useful in different ways. An overview on techniques and scientific potential was recently given by [Kirchengast, 2004]. Special forms of this measurement method are the GNSS-LEO (description of method and scientific potential in, e.g., [Kursinski et al., 1997], [Lee et al., 2001], [Steiner et al., 2001], [Hajj et al., 2002]) and the LEO-LEO radio occultation technique (description in, e.g., [Kursinski et al., 2002, 2004]). Both are satellite-based, bistatic systems to explore the earth's atmosphere in an active limb scanning mode. From the standpoint of the receiver (which is always a LEO satellite), an occultation event occurs, when the transmitting satellite (a GNSS or LEO satellite) sets or rises behind the planet, so that the transmitted radio waves pass through the atmosphere, where they are increasingly refracted and absorbed. From the measurement of the phase path and the weakened amplitude at the receiver, the atmospheric refractivity profile can be reconstructed through inversion methods from which different atmospheric parameters like density, pressure, temperature, and humidity, can be derived.

The GNSS-LEO and LEO-LEO radio occultation techniques possess an unique combination of features, such as self-calibration of the profiles, high vertical resolution ( $\leq 1$  km), even global coverage, and the high independence of weather processes, for example. Therefore, above all in climate science — in particular in atmospheric climate change analysis — it is superior to nearly every other earth sensing technique.

The subsequent sections deal with the LEO-LEO radio occultation technique. Historical (Sect. 2.1), technical (Sect. 2.2) and phenomenological (Sects. 2.3 and 2.4) aspects will thereby be considered. Detailed recent reference descriptions on the

LEO-LEO radio occultation technique and its potential have been given by [Høeg and Kirchengast, 2002], [Kursinski et al., 2002, 2004], [Kirchengast and Høeg, 2004], [Herman et al., 2004], [Kirchengast et al., 2004a, b], and [ESA, 2004a, c].

## 2.1 History

The roots of the atmospheric radio occultation technique go back to the first days of interplanetary flight in the early 1960's (see the review by [Yunck et al., 2000]). After methods to monitor charged particles and plasma in the interplanetary space were already known, scientists began to investigate the capabilities of radio links for probing planetary atmospheres [Melbourne et al., 1994]. Within the scope of NASA's Mariner III and IV missions to Mars, the first two proposals using single-frequency radio occultation for atmospheric sounding were presented: The first was a one-way observing system exploiting radio instruments aboard the Mariner spacecraft to monitor the martian ionosphere and surface properties [Fjeldbo, 1964], proposed from a group at the Stanford University in 1962. The second, a two-way radio occultation technique, which was designed for probing the atmosphere of Mars [Kliore et al., 1964], was presented by scientists of the Jet Propulsion Laboratory (JPL) in 1963. A little bit later, these two research teams in cooperation developed the Abel inversion technique (e.g., [Fjeldbo and Eshelman, 1965], [Phinney and Anderson, 1968], [Fjeldbo et al., 1971]) from the Wiechert-Herglotz method (which is used to determine the velocity of seismic waves inside the earth, see, e.g., [Kertz, 1995]). The Abel inversion (see Subsect. 2.2.2) allows to retrieve accurate refractivity profiles from radio occultation data. Furthermore, a dual-frequency approach was presented, which allows to experimentally separate dispersive ionospheric refraction effects from the mainly non-dispersive effects of the neutral atmosphere [Fjeldbo and Eshelman, 1968].

In the years after, nearly every planet of the solar system — except the earth itself — together with many of their moons and ring systems were investigated using radio occultation. On the part of American activities, the Mariner, Pioneer, and Voyager missions contributed essentially (see, e.g., [Fjeldbo et al., 1971], [Eshelman, 1973], [Kliore et al., 1975], [Lindal et al., 1983, 1987], [Marouf et al., 1986], [Tyler, 1987], and [Lindal, 1992]). Russian scientists applied radio occultation as well for probing planetary atmospheres; for example the atmosphere of Venus [Yakovlev et al., 1991].

Whereas planetary atmospheres were enthusiastically occulted since the mid 1960's, radio occultation was applied relatively late to the earth's atmosphere. The main reason for this was that the structure of the terrestrial atmosphere was quite well known in the pioneering days of the radio occultation technique; establishing the required infrastructure (transmitters, receivers, ground stations, etc.) to retrieve horizontally and vertically well resolved, accurate measurements enhancing the atmospheric data set existing back then would have had a cost exceeding the level

of interest [Kursinski et al., 1997]. As a result, the first proposals for remote sensing of the earth’s atmosphere using the radio occultation technique ([Fischbach, 1965], [Lusignan et al., 1969]) were not realized. The situation changed with the arrival of the Global Positioning System (GPS, detailed descriptions in, e.g., [Hofmann-Wellenhof et al., 2001], [Leick, 1995], and [Bauer, 1997]) and its Russian counterpart GLONASS (Global Navigation Satellite System, see [Engler et al., 1997]) in the late 1970’s: Even if their occultation capabilities were recognized only about a decade after their introduction, radio occultation for earth observation now became possible at comparatively low costs with these “transmitters of opportunity”.

In 1987, the NASA started a new earth science initiative called *Mission to Planet Earth* (now *Earth Science Enterprise*). The objective was to build up a series of earth satellites observing our planet as a complex, interdependent whole [Yunck et al., 2000]. Within the scope of this, a team of the JPL investigated the capabilities of GPS receivers on satellites for earth sciences. The result of these efforts was the GGI (GPS Geoscience Instrument, [Melbourne et al., 1988]) proposal, which was approved by NASA in 1989. Unfortunately, in 1993, GGI was dropped because of cutbacks and restructuring in the program. On the Russian part, a proposal using GPS receivers on Low Earth Orbit (LEO) satellites for sensing the earth’s atmosphere was presented by [Gurvich and Krasil’nikova, 1990; Russian original, 1987].

The first project demonstrating the GPS radio occultation technique for terrestrial atmosphere sounding was the GPS Meteorology (GPS/MET) experiment. It was developed at UCAR (University Corporation for Atmospheric Research) in Boulder, Colorado, and proposed to NSF (National Science Foundation) in 1991. Finally, in April 1995, the GPS/MET instrument, a high precision TurboRogue dual frequency receiver (TRSR-1) built by the JPL, was launched aboard NASA’s MicroLab-1 spacecraft into a low earth orbit. Within the following two years, it measured phase paths and amplitudes during the setting of the GPS-to-LEO limb through the Earth’s atmosphere. Although the GPS/MET experiment still had its weaknesses, it was very successful. About 50,000 occultations were recorded of which around 20% (estimation by [Rocken et al., 1997]) were evaluated. From the analysis of the data not only precise vertical profiles of geopotential height, density, pressure, and temperature were retrieved; precious information about the properties, the behavior, and the tracking of occultation signals was obtained as well. Subsequently, this knowledge was applied to the development of the next generation of GPS receivers.

Since the GPS/MET experiment was carried out successfully, a series of international satellite projects applying the GPS radio occultation technique have been proposed and partly realized. Some important satellite projects are listed in Table 2.1.

The GNSS-LEO radio occultation technique provides very accurate profiles of various climatic parameters; temperature profiles can accurately be retrieved through-

Mission & Act. Period	Receiver	Description
GPS/MET 1995–1997	TRSR-1	An experiment demonstrating active limb sounding (UCAR, JPL, NSF, NOAA, FAA, NASA, UNAVCO, NCAR, etc.). See Sect. 2.1 and [GPS/MET, 2004].
ØRSTED 1999–2000	TRSR-1	Danish mission (DMI, JPL, NASA, etc.). Designed primarily for magnetic field mapping. Data of poor quality because of antenna constraints (small spacecraft) and continuous GPS signal encryption. See [ØRSTED, 2004].
SUNSAT 1999–2004 ongoing	TRSR-1	South African mission, in cooperation with JPL, NASA. Carries a high-resolution imager. Same problems with the data quality as ØRSTED.
CHAMP 2000–2006 ongoing	TRSR-2	German mission (GFZ, DLR, JPL, NASA, CNES, etc.). Designed primarily for magnetometry and gravity mapping. Two aft-looking GPS antennae (7–10 dB gain), one down-looking antenna (in attempt to capture GPS ocean/surface reflections). See [CHAMP, 2004].
SAC-C 2000–2004 ongoing	TRSR-3	Argentine mission (CONAE, JPL, NASA, etc.). Carries a multispectral imager and magnetometer. Two GPS antennae (7–10 dB gain), one in fore, the other in aft velocity direction (allows rising and setting occultations); additional down-looking antenna.
GRACE 2002–2007 ongoing	TRSR-2	American-German twin satellite gravity field mission (NASA, DLR, UTCSR, GFZ, JPL, etc.). GPS antennae fore and aft, one on each spacecraft. Performs satellite-satellite ranging as well. See [GRACE, 2004].
COSMIC 2005–2009	IGOR	Interdisciplinary American-Taiwanese mission (NSPO, JPL, UCAR, NASA, NSF, NOAA, ONR, etc.) addressing meteorology, climate, ionosphere, and geodesy; constellation of six micro satellites. See, e.g., [Lee et al., 2001], [COSMIC, 2004].
METOP 2005–2019	GRAS	European component (managed by EUMETSAT) of an American/European polar-orbiting satellite system dedicated to meteorology and climatology; launch of three spacecrafts sequentially. Antenna configuration allows to capture setting as well as rising occultations. See [METOP, 2004].

Table 2.1: Some past, current, and future missions working with GPS/RO receivers.

out the upper troposphere and stratosphere ( $\sim 5\text{--}40$  km). The presence of water vapour in the lower troposphere (below  $5\text{--}7$  km), however, requires a more elaborated analysis method. Since, besides dry air, water vapour causes an additional refraction of the radio waves, the temperature information cannot be separated from the water vapour information when using just the GPS frequencies (L-band,  $1\text{--}2$  GHz). Therefore, additional information like temperature or water vapour profiles obtained from other sources, or additional assumptions such as the negligence of water vapour in polar regions is needed to remove this ambiguity. As the additional information and assumptions are only approximations to the real conditions, this would introduce slight errors. Because of this weakness, scientists developed the LEO-LEO radio occultation technique, which enables independent measurements of water vapour and temperature.

The main differences between the GNSS-LEO and the LEO-LEO radio occultation technique are the use of little higher frequencies and significantly higher signal-to-noise ratios. The LEO-LEO radio occultation for water vapour detection exploits various frequencies within and near a water vapour absorption line (e.g.,  $22.23$  GHz or  $183.31$  GHz), which are transmitted from one LEO satellite to another. During the passage through the atmosphere, the signals are not only refracted but also noticeably absorbed (in contrast to the GNSS frequencies). Besides the information included in the refraction, now additional information from the absorption is available, which refers to the atmospheric water vapour content. Thus, if refraction and absorption due to water vapour are known, accurate temperature and humidity profiles can be retrieved separately without additional assumptions or information from other sources. Limitations will be found in the lower troposphere in case of heavy clouds and turbulence, where auxiliary information will also be needed for LEO-LEO radio occultation. For a detailed description of the retrieval algorithm we developed see Section 2.2.

The first suggestion for LEO-LEO radio occultation dates back to 1969 [Lusignan et al., 1969]. Afterwards, it took a while until the first projects were proposed. One of which was the Active Tropospheric Ozone and Moisture Sounder (ATOMS, see, e.g., [Feng et al., 2001], [Herman et al., 2004]) which was submitted from a group of the University of Arizona to the NASA's Instrument Incubator Program (IIP) in 1998. It was conceived in order to provide independent water vapour and temperature profiles as well as ozone profiles. Unfortunately, the project was not implemented. Succeeding projects like WATS (Water Vapour and Temperature in the Troposphere and Stratosphere, see [ESA, 2001]), which was proposed as an Earth Explorer Core Mission to ESA in 2000, got not implemented, too. But probably in the future, some stakeholders will take heart to support this innovative earth observation methodology which is of unique importance in climate and other sciences.

## 2.2 Physical Principles and Retrieval Methodology

The LEO-LEO radio occultation method allows, among other things, to retrieve temperature independent from water vapour. Underlying principles for this will be discussed in the course of this section.

The LEO-LEO radio occultation is performed by two low earth orbiting satellites (see Fig. 2.1) in an active limb scanning mode. During the movement around the earth it regularly occurs that one satellite disappears (sets) or emerges (rises) behind the planet from the other satellite's point of view. While doing so, the radio signals which are transmitted from one spacecraft (in general the one in higher orbit) to the other traverse the planetary atmosphere. Due to the relative motion between the satellites, the atmosphere is scanned from top to surface or in opposite direction obtaining a set of observables relating to different heights (profiles). In the former case, we speak of setting occultation, in the latter of rising occultation.

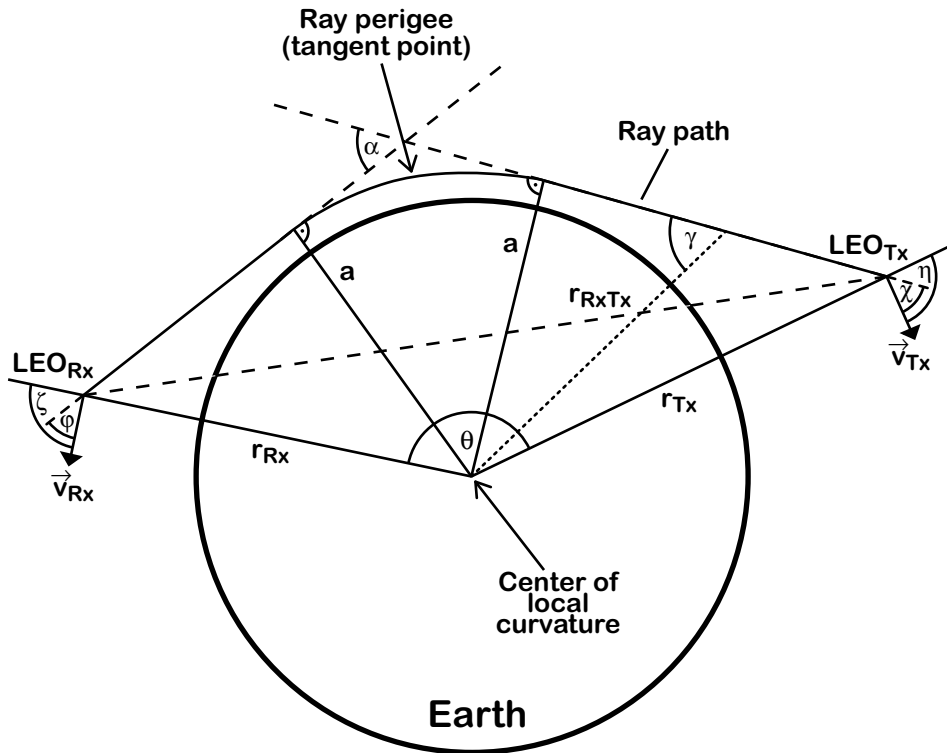


Figure 2.1: LEO-LEO occultation geometry during a setting event, defining various parameters used in the text. The geometrical situation is shown in the occultation plane, i.e., the plane spanned by the transmitter and receiver satellite position vectors  $r_{Tx}$  and  $r_{Rx}$ , respectively.

Within the atmosphere, the radio signals are refracted and absorbed. In the geometrical optics approximation, the result of the refraction is a small bending of the signal path according to Snell's law. If precise positions and velocities of the satellites are known, the bending angle can be computed using measurements of phase path (see Subsect. 2.2.1), which is the first main observable. As a consequence of the absorption, the amplitude (intensity of the signal), which is the second main observable, is weakened according to the Bouguer-Lambert-Beer law. From this measurement, the transmission can be derived (see Subsect. 2.2.1). In order to retrieve temperature independently from water vapour, the signal frequencies must lie near a water vapour absorption line where other (trace) components have nearly no influence on absorption. Therefore, the weakening of the amplitude indicates the amount of water vapour along the ray path. Particularly, the 22.23 GHz and 183.31 GHz absorption lines are suitable. Furthermore, usage of additional frequencies near absorption lines of other atmospheric components allows to retrieve vertical profiles of them, too. As an illustration, the 195.43 GHz line is suitable for ozone detection [Herman et al., 2004].

From the retrieved bending angle profile the real refractivity profile can be derived by means of the classical Abel transform. Subsequently, the imaginary refractivity profile can be computed using the real refractivity index profile together with the transmission profiles at each signal frequency via another Abel transform (see Sect. 2.2.2). Finally, by simultaneously solving the real refractivity equation, the imaginary refractivity equations (for each frequency one equation), and the hydrostatic equation profiles of temperature, total air pressure, and the partial pressure of water vapour can be derived. If enough frequencies are available, liquid water and rain rate can also be calculated.

A simple overview of the retrieval structure shortly described above is shown in Figure 2.2. A detailed description will be given in the following subsections.

### 2.2.1 Retrieval of Bending Angle and Transmission

The concept of the LEO-LEO bending angle retrieval is more or less identical to the GNSS-LEO one. Literature thus exists, e.g., from [Kursinski et al., 1997, 2000], [Steiner, 1998], [Syndergaard, 1999], and [Nielsen et al., 2003]. In contrast, the use of amplitude measurements for transmission retrieval and subsequent derivation of imaginary refractivity is a unique feature of the LEO-LEO occultation technique. Descriptions of this method can be found in, e.g., [Kursinski et al., 2002], [Nielsen et al., 2003], and [Kirchengast et al., 2004b].

Generally, there are different approaches to the retrieval of bending angle and transmission as a function of the impact parameter  $a$  (see Fig. 2.1), either based on geometric-optics (GO) or on wave-optics (WO, see, e.g., [Nielsen et al., 2003] and references therein). In the following, a geometric-optics approximation will be described. A detailed description on how the bending angle and transmission

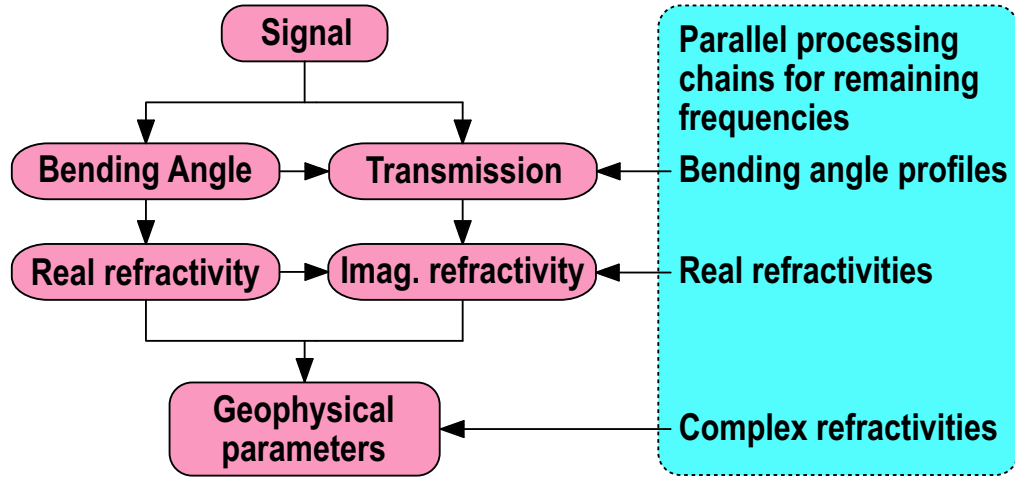


Figure 2.2: Overview of a LEO-LEO retrieval processing chain. The five upper boxes on the left represent the processing chain for a single frequency channel, whereas the box on the right represents parallel processing chains for the remaining carrier frequencies in the system. After [Nielsen et al., 2003].

retrieval is implemented in EGOPS5 used later for the simulations has been given by [Kirchengast et al., 2004b].

### Bending Angle Retrieval

The atmospheric real refractivity (Eq. 2.25) causes a bending of rays traversing the atmosphere. In particular, the real refractivity of the ionosphere is caused by vertical electron gradients and depends on the frequency; the total bending of microwaves in the bulk of the ionosphere is directed away from earth. Beneath, in the neutral atmosphere, the real refractivity results predominately from the air density and its vertical gradients. Therefore, it is equal for all frequencies and bending is usually directed towards the earth (as depicted in Fig. 2.1).

The bending angle  $\alpha$  (see Fig. 2.1) describes the change in the raypath direction accumulated along the raypath [Kursinski et al., 2000]. Generally, it is very small, reaching only  $1\text{--}2^\circ$  for rays close to the surface depending on the water vapour gradient in low altitudes. Because of this, the direct measurement of  $\alpha$  is difficult. Therefore, the bending angle is derived from accurate phase measurements at the receiver. First, from the observed phase differences  $\Delta\varphi_i$  the excess phase paths (also called phase delays)  $\Delta L_i$  of each frequency (relative to the phase paths in vacuum  $S_0$ ) will be calculated:

$$\Delta L_i(t_j) = \int_{LEO_{Tx}}^{LEO_{Rx}} n(s_i(t)) ds_i(t) - S_0(t_j) = \Delta\varphi_i(t_j)\lambda_i \quad (2.1)$$

$\Delta L_i$  is the phase delay at the frequency  $f_i$  (wavelength  $\lambda_i$ ) along the bent ray path  $s_i$  depending on the refractive index  $n$ , and  $t_j$  is the occultation event time. Since the ionospheric bending depends on the frequency, different signals travel on slightly different paths  $s_i$ .

In order to eliminate most of the ionospheric contribution to the total bending, a simple linear combination of two phase delays belonging to different frequencies can be applied, for instance (after [Foelsche, 1999])

$$\Delta L_a(t_j) = \frac{f_1^2 \cdot \Delta L_1(t_j) - f_2^2 \cdot \Delta L_2(t_j)}{f_1^2 - f_2^2}. \quad (2.2)$$

In this way, the first order contribution from the ionosphere is removed. Now, the phase delay  $\Delta L_a$  contains only the contribution of the neutral atmosphere. The remaining error depends on the state of the ionosphere and thus on the solar activity. Instead of Eq. 2.2 known as the standard correction, a similar linear correction directly applied to bending can be used: the so called bending angle correction (see, e.g., [Vorob'ev and Krasnil'nikova, 1994]).

Next, the Doppler shift  $\Delta f$ , which is caused by the relative motion of the satellites and additionally influenced by the atmospheric bending, can be derived from the phase delay  $\Delta L_a(t_j)$  via differentiation with respect to time  $t$ :

$$\Delta f(t_j)[\text{m/s}] = \frac{d(\Delta L_a(t_j))}{dt} \quad (2.3)$$

$$\Delta f_i(t_j)[\text{Hz}] = -\frac{f_i}{c} \cdot \Delta f(t_j) \quad (2.4)$$

$c$  is the velocity of light, which amounts to  $299,792,458 \text{ m s}^{-1}$ . As can be seen from Eq. 2.3, the absolute phase delay does not need to be known in order to calculate the Doppler shift, but only the phase change, which can be accurately tracked during the occultation event. This is also the reason for the intrinsic self-calibration of refractive occultation data, because each Doppler profile is an absolute measure of the atmospheric bending angle, independent from external reference or calibration data.

Next, assuming spherical symmetry of the atmosphere, the Doppler shift can be expressed by the satellites' orbital positions  $\vec{r}(t)$  and velocities  $\vec{v}(t)$ , which are known from data of GNSS Satellites (after [Syndergaard, 1999]):

$$\Delta f(t_j)[\text{m/sec}] = [v_{\text{Rx}} \cos \varphi(a_j) - v_{\text{Tx}} \cos \chi(a_j)] - \frac{dr_{\text{RxTx}}(t_j)}{dt} \quad (2.5)$$

with

$$\varphi(a_j) = \zeta - \arcsin\left(\frac{a_j}{r_{\text{Rx}}}\right) \quad (2.6)$$

$$\chi(a_j) = (\pi - \eta) - \arcsin\left(\frac{a_j}{r_{\text{Tx}}}\right) \quad (2.7)$$

- $a_j$  ... impact parameter for data sample  $j$  (time  $j$ ) which is the perpendicular distance between either of the ray asymptotes and the center of local curvature
- $r_{\text{Tx}}, r_{\text{Rx}}$  ... distance of the transmitter (Tx) and the receiver (Rx) respectively from the center of local curvature
- $r_{\text{RxTx}}$  ... distance between the transmitter and receiver satellites
- $v_{\text{Tx}}, v_{\text{Rx}}$  ... velocity of the transmitter and the receiver satellite, respectively (in the occultation plane)
- $\zeta$  ... angle between the Rx velocity and position vectors (in the occultation plane)
- $\eta$  ... angle between the Tx velocity and position vectors (in the occultation plane)

By solving Equation 2.5, the impact parameter  $a_j$  can be found, from which, finally, the bending angle  $\alpha(a_j)$  is computed using the following relation:

$$\alpha(a_j) = \theta - \arccos\left(\frac{a_j}{r_{\text{Rx}}}\right) - \arccos\left(\frac{a_j}{r_{\text{Tx}}}\right) \quad (2.8)$$

Therein,  $\alpha(a_j)$  is the bending angle for data sample  $j$ , and  $\theta$  represents the angle between the transmitter and receiver position vectors. An illustration of the variables used in Eqs. 2.5–2.8 is shown in Fig. 2.1.

Thus, if the position and velocity vectors of the satellites as well as the Doppler shift are known, the bending angle  $\alpha(a_j)$  can be derived iteratively from Eqs. 2.5–2.8. Strictly speaking, this procedure is only valid for a spherically symmetric atmospheric refractivity field. Tangential refractivity gradients due to the ellipsoidal shape of the earth will therefore affect the measurements of  $\alpha(a_j)$ . This weak spot can be handled by replacing the earth's center of mass with the ellipsoid's center of local curvature in the occultation plane at the mean geographic location of the occultation event. First order errors can be eliminated applying this so called oblateness correction (see [Syndergaard, 1998]).

### Transmission Retrieval

Radio waves passing through the atmosphere will not only be affected in their speed of propagation (leading to ray bending) but also in their amplitude because of absorption. Thus, the index of refraction  $n$  is usually complex. The influence of the amplitude is reflected in the signal intensity  $I$  being damped along the ray path according to the Bouguer-Lambert-Beer law:

$$dI = -I\kappa(l)dl \quad (2.9)$$

$$I = I_0 \cdot e^{-\int_{\text{Tx}}^{\text{Rx}} \kappa(l)dl} = I_0 \cdot e^{-\tau} \quad (2.10)$$

Here,  $I$  is the received signal intensity,  $I_0$  is the un-attenuated intensity at the transmitter Tx,  $l$  is the coordinate along the signal path,  $\kappa$  ( $= 4\pi N''/\lambda_0 \cdot 10^{-6}$ ) is the absorption coefficient along the ray path, and  $\tau$  ( $= \ln(I_0/I)$ ) is the optical thickness.

In this connection, the (fractional) transmission  $Tr$  is defined by

$$Tr = \left( \frac{I}{I_0} \right) = e^{-\tau}. \quad (2.11)$$

Thus, since the intensity  $I$  is proportional to the amplitude  $A$  squared ( $I \propto A^2$ ), the transmission can be derived from amplitude measurements.

Because the observed amplitudes  $A_i(t_j)$  contain — besides the desired loss due to absorption — loss due to differential bending (defocussing) and spherical signal spreading, amplitude data must be corrected. Applying geometrical optics, these amplitude modulations can be related to the bending angle profile  $\alpha(a_j)$  (known from Eq. 2.8) or alternatively to the satellite opening angles  $\theta(a_j)$  (see Fig. 2.1), the impact parameter profile  $a_j$ , as well as the transmitter and receiver satellite radial distances  $r_{Tx}(a_j)$  and  $r_{Rx}(a_j)$  (after [Jensen et al., 2003]):

$$A_{\text{dsm}}(a_j) = \left[ \frac{a_j}{(r_{Tx}r_{Rx})^2 \sin(\theta) \sqrt{1 - \left(\frac{a_j}{r_{Tx}}\right)^2} \sqrt{1 - \left(\frac{a_j}{r_{Rx}}\right)^2} \left| \frac{d\theta}{da} \right|_j} \right]^{\frac{1}{2}}. \quad (2.12)$$

This equation makes it possible to compute the magnitude of the amplitude modulations due to defocussing and spreading  $A_{\text{dsm}}(a_j)$ . Generally, there are various other ways to derive  $A_{\text{dsm}}(a_j)$ , using GO processing (see e. g. [Sokolovskiy, 2000], [Leroy, 2001]) as well as WO processing ([Jensen et al., 2003], [Nielsen et al., 2003]).

Subsequently, defocussing and spreading can be accounted for by multiplying the observed signal amplitudes  $A_i(t_j)$  with the inverse of Eq. 2.12. Using the corrected amplitudes, the transmissions  $Tr_i(a_j)$  at each signal frequency  $i$  containing absorption only can finally be computed. In EGOPS5, as described by [Kirchengast et al., 2004b], the following relations are applied:

$Tr_i(a_j)$  being a normalized intensity,  $A_i(t_j)$  has to be divided by a normalization amplitude at some reference height besides removing the defocussing and spreading components. A simple manner to combine these two needs is to set up a defocussing and spreading model amplitude scaled to match the signal amplitude  $A_i(a_j)$  at the reference height  $z_{\text{ref } i}$ :

$$A_i^{\text{dsm}}(a_j) = \left( \frac{A_i}{A_{\text{dsm}}} \right)_{z_{\text{ref } i}}^{\Delta z} A_{\text{dsm}}(a_j) \quad (2.13)$$

$\left( \frac{A_i}{A_{\text{dsm}}} \right)_{z_{\text{ref } i}}^{\Delta z}$  is the absorption amplitude at  $z_{\text{ref } i}$  for the frequency  $i$ , averaged over a height range  $\pm \Delta z/2$  around  $z_{\text{ref } i}$ .  $A_i^{\text{dsm}}(a_j)$  is the normalized defocussing and

spreading model amplitude. The reference height  $z_{\text{ref } i}$  has to be chosen at an altitude, where no absorption has occurred yet (25–30 km is adequate in the case of the 22 GHz water vapour line). This amplitude normalization for each individual event to a reference height is the reason for the intrinsic self-calibration of the measured amplitudes, yielding a technique well suited for long-term climate variation detection.

The desired transmissions  $Tr_i(a_j)$  at each signal frequency  $i$  related only to absorption now can be derived from the quotient  $A_i(a_j)/A_i^{\text{dsm}}(a_j)$ , corresponding to a subtraction in the [dB] space:

$$Tr_i(a_j) = -20 \cdot (\log(A_i) - \log(A_i^{\text{dsm}})) \text{ [dB]}. \quad (2.14)$$

Summing up, the transmissions as functions of the impact parameter  $a$  can be derived via GO processing executing the following steps: computation of bending angle as a function of  $a$ ; expression of signal amplitudes or intensities as a function of  $a$ ; removal of defocussing and spreading using the bending angle profile; and finally construction of the transmission profiles as a function of  $a$  using an appropriate normalization factor.

## 2.2.2 Retrieval of Real and Imaginary Refractivity

The bending angle and transmission profiles as functions of the impact parameter derived in Subsection 2.2.1 are now ready for Abelian inversions in order to retrieve the atmospheric refractivity  $N$ . The refractivity is a measure for the index of refraction  $n$ , which at microwave frequencies is close to unity in the earth's atmosphere:

$$N = (n - 1) \cdot 10^6 \quad (2.15)$$

Generally,  $N$  is a complex quantity,

$$N = N' + i \cdot N'' \quad (2.16)$$

because a medium affects both phase and amplitude of signals. The real part  $N'$  accounts for the phase changes, which lead to phase delay due to a change in the propagation velocity and due to ray bending. The imaginary part  $N''$ , however, accounts for the amplitude changes, which are caused by absorption and result in a damping of the signal. Thus, knowing bending angle and transmission profiles makes it possible to retrieve profiles of  $N'$  and  $N''$  which will be described below.

### Real Refractivity Retrieval

Assuming a spherically stratified medium the total bending angle and the real refractive index are related as follows (derivation e.g. reviewed in [Foelsche, 1999]):

$$\alpha(a_j) = 2a_j \int_{r_j}^{\infty} \frac{1}{\sqrt{r^2 \cdot (n')^2 - a_j^2}} \frac{d \ln(n')}{dr} dr \quad (2.17)$$

with

$$r = \frac{a}{n'(a) \sin \gamma}, \quad r_j = \frac{a_j}{n'(a_j)}, \quad (2.18)$$

where  $r$  is the distance from the center of local curvature and  $\gamma$  is the angle between ray path and radial direction. The tangent radius  $r_j$  is the radial distance from the center of local curvature to the tangent point (see Fig. 2.1) where  $\gamma$  equals  $\frac{\pi}{2}$ . As we see from Eq. 2.17,  $\alpha(a)$  is caused by radial variations of  $n'$ .

Since from occultation data the bending angle is known as a function of impact parameter, the inverse relation of Eq. 2.17 is required in order to obtain the real refractive index. The inversion is done using a special form of the more general Abel transform, derived by [Fjeldbo et al., 1971]:

$$n'(a_j) = \exp \left( \frac{1}{\pi} \int_{a_j}^{\infty} \frac{\alpha(a)}{\sqrt{a^2 - a_j^2}} da \right) \quad (2.19)$$

In practice, the upper limit of the integral is set to a height above which bending is (nearly) negligible. From Eq. 2.19, the real refractivity profile  $N'(z_j)$  as a function of height is now obtained via

$$N'(z_j) = 10^6 (n'(a_j) - 1) \quad (2.20)$$

with

$$z_j = r_j - R_c, \quad \text{with } r_j = \frac{a_j}{n'(a_j)}, \quad (2.21)$$

where  $z_j$  is the ellipsoidal height level corresponding to  $a_j$  and  $R_c$  is the radius of the local curvature.  $R_c$  from the bending angle retrieval has to be chosen again in order to meet the requirements of spherical symmetry and to ensure accurate ellipsoidal heights  $z_j$ .

Summing up, the real refractivity profile is derived from the bending angle profile via an Abel integral equation.

### Imaginary Refractivity Retrieval

The transmissions at each signal frequency  $i$  are related to the absorption coefficients  $\kappa_i$  via (after [Kursinski et al., 2002])

$$Tr_i(a_j) = \exp \left( -2 \int_{r_j}^{\infty} \kappa_i \frac{n'r}{\sqrt{(n'r)^2 - (n'_j r_j)^2}} dr \right), \quad (2.22)$$

where  $r$  is a function of the real refractive index ( $r(n')$ , see Eq. 2.18). Since bending angle, transmissions and real refractivity are known from the steps before, the absorption coefficient can be derived if the inverse relation from Eq. 2.22 is known.

Analogous to the real refractivity retrieval, the inversion is done using a different kind of Abel transform which leads to (after [Kirchengast et al., 2004b])

$$\kappa_i(z_j) = \frac{1}{\pi} \left| \frac{da}{dr} \right|_{a=a_j} \int_{a_j}^{\infty} \frac{d \ln(Tr_i(a))}{da} \frac{1}{\sqrt{a^2 - a_j^2}} da. \quad (2.23)$$

In practice, the upper limit of the integral is set to a height above which the log-transmission  $\ln(Tr_i(a))$  is (nearly) zero; the obvious height to choose would be  $z_{\text{ref } i} + \Delta z/2$  as defined in Eq. 2.13. Additionally, it is worth to note that the transmission appears as the derivative of its logarithm in Eq. 2.23 because the signal absorption is related to relative variations in the signal intensity and not to absolute variations. Therefore, the integral evaluation will be independent of the normalization factor used in the transmission retrieval (as long, as the defocussing and spreading is properly corrected, i.e., practically for normalization heights with negligible absorption).

Finally, the imaginary refractivity profiles  $N'_i(z_j)$  as a function of height are obtained from Eq. 2.23 using

$$N''_i(z_j) = 10^6 \cdot \frac{c}{4\pi f_i} \kappa_i(z_j). \quad (2.24)$$

Eq. 2.24 shows the standard relation between the imaginary refractivity and the absorption coefficient (see, e.g., [Schanda, 1986], [Nielsen et al., 2003]), which are proportional via the wavelength.

To conclude, profiles of the imaginary refractivity are retrieved via an Abel integral equation using the impact parameter profile, the real refractive index profile and the transmission profiles. In EGOPS5, filtering is subsequently applied in order to mitigate noise at scales  $< 1$  km (see [Kirchengast et al., 2004b]).

### 2.2.3 Retrieval of Atmospheric Profiles

From the profiles of real and imaginary refractivity derived above, atmospheric profiles of pressure, temperature, and water vapour pressure can be retrieved independently from each other. A set of equations relating the desired quantities to the refractivities as well as to each other is used for this purpose. In regions where there is no liquid water, for instance in the bulk of the upper troposphere and in the stratosphere, two frequencies are sufficient in order to resolve the desired parameters. If liquid water is present, however, at least three frequencies are needed.

At microwave wavelengths, the real refractivity  $N'$  as a function of height  $z$  is related to pressure  $p$  [hPa], temperature  $T$  [K], water vapour partial pressure  $e$  [hPa],

electron density  $n_e$  [ $\text{m}^{-3}$ ], and liquid water content  $lw$  [ $\text{g m}^{-3}$ ] via [Kursinski et al., 1997]

$$N'(z) = 77.60 \frac{p(z)}{T(z)} + 3.73 \cdot 10^5 \frac{e(z)}{T(z)^2} + 4.03 \cdot 10^7 \frac{n_e(z)}{f^2} + 1.4 lw(z), \quad (2.25)$$

where  $f$  [Hz] is the transmitter frequency. The latter term of this equation, the so-called scattering term arises from liquid water droplets. For realistic suspensions of water this term is small compared to the other terms and can therefore be neglected [Kursinski et al., 1997]. Moreover, the third, so-called ionospheric term which is mainly caused by free electrons in the ionosphere was eliminated during the bending angle retrieval through the linear combination of frequencies (see Eq. 2.2). Consequently, Eq. 2.25 is reduced to the following relation, known as the *Smith-Weintraub* formula:

$$N'(z) = 77.60 \frac{p(z)}{T(z)} + 3.73 \cdot 10^5 \frac{e(z)}{T(z)^2} \quad (2.26)$$

Therein, the first, so-called dry term exists because of the polarizability of atmospheric molecules. The other is due to the permanent dipole moment of water vapour and is therefore called moist term.

Similar to the real refractivity, the imaginary refractivity  $N''$  is connected to atmospheric parameters, too. To be precise, gaseous absorption as well as extinction by hydrometeors (water droplets, ice crystals, rain) have frequency-dependent influence on attenuation and thus on  $N''$ . The gas absorption happens because of various constituents of the atmosphere. Especially, for frequencies around the 22.23 GHz line the most important gas absorbers are water vapour and molecular oxygen, minor contributions are coming from  $N_2$ ,  $CO_2$ , and  $O_3$  [Nielsen et al., 2003]. Hydrometeors, which are located in clouds and rain, cause absorption as well as scattering of the signal. Generally, the absorption by cloud droplets is about two orders of magnitudes greater than that by ice crystals. Additionally, at frequencies around 22.23 GHz the scattering cross section of cloud droplets usually found in the atmosphere (radii from 1 to 50  $\mu\text{m}$ ) is less than 0.2% of the absorption cross section; for ice crystals, this ratio is less than 10%. Thus, the scattering of both ice and water cloud particles can be neglected and the extinction coefficient is the same as the absorption coefficient. Rain drops, however, are usually quite a bit larger than cloud droplets wherefore scattering cannot be neglected if it is raining.

The imaginary as well as the real refractivity can be parameterized using a Millimeter-wave Propagation Model, for example the *Liebe model* (MPM93, see, e.g., [Liebe et al., 1993], [Eriksson et al., 2001]) of which a macroscopic expression is:

$$(N'^{\text{mod}}(z), N''_i^{\text{mod}}(z)) = N_i^{\text{mod}}(f_i, p(z), T(z), e(z), lw(z), iw(z), rr(z)) \quad (2.27)$$

Therein,  $lw$  is the cloud liquid water content,  $iw$  is the cloud ice water content, and  $rr$  is the rain rate. Furthermore,  $N'^{\text{mod}}$ ,  $N''_i^{\text{mod}}$  and  $N_i^{\text{mod}}$  are the modelled real,

imaginary, and complex refractivities for the frequency  $f_i$ , respectively. It should be mentioned that  $N'^{\text{mod}}$  can be modelled in such a way as to make it equal to  $N'$  of Eq. 2.26.

The retrieval of atmospheric pressure, temperature, and specific humidity further requires, besides Eqs. 2.26 and 2.27, an equation relating the desired parameters to each other. This is the hydrostatic equation

$$\frac{dp(z)}{dz} = -g(z)\rho(z), \quad (2.28)$$

together with the equation of state

$$\rho(z) = \frac{p(z)m^{\text{d}}}{T_{\text{v}}(z)R}, \quad (2.29)$$

the equation of virtual temperature

$$T_{\text{v}}(z) = T(z) \cdot (1 + 0.608 q(z)), \quad (2.30)$$

as well as the equation converting water vapour pressure to specific humidity

$$q(z) = 0.622 \frac{e(z)}{(p(z) - 0.378 e(z))}. \quad (2.31)$$

Therein,  $g$  [ $\text{m s}^{-2}$ ] is the acceleration of gravity,  $\rho$  [ $\text{kg m}^{-3}$ ] is the air density,  $m^{\text{d}}$  ( $= 28.964 \text{ g mol}^{-1}$ ) is the mean molecular mass of dry air,  $T_{\text{v}}$  is the virtual temperature,  $R$  ( $= 8.3145 \text{ J K}^{-1} \text{ mol}^{-1}$ ) is the universal gas constant, and  $q$  the specific humidity.

Now, profiles of atmospheric pressure  $p(z)$ , temperature  $T(z)$ , water vapour pressure  $e(z)$  and liquid water  $lw(z)$  (if required) can be derived by simultaneously solving Eqs. 2.26–2.31. Usually, the problem can only be solved numerically: It is efficient to first compute the pressure level below the uppermost level by integration of the hydrostatic equation (assuming a specific atmospheric state in the uppermost level, e.g.,  $(p_{\text{top}}, T_{\text{top}}, e_{\text{top}} = lw_{\text{top}} = 0)$ ). Subsequently, temperature, water vapour partial pressure, and liquid water at this height can be derived from pressure and the real and imaginary refractivities, for instance by a non-linear least-squares-based optimal estimation (cf. Subsect. 4.2.4, Eq. 4.2, and [Kirchengast et al., 2004b]). For more information on least-squares optimal estimation techniques consult [Bjørck, 1996] or [Rodgers, 2000]. This procedure will then be repeated for each height step down to the surface using the atmospheric state from the previous height. Thus the desired profiles of  $p$ ,  $T$ ,  $e$  and  $lw$  are known.

The atmospheric profiles retrieval described above is implemented in a refined manner in the simulation tool EGOPS5 (overview in Chapt. 4). For a detailed description of the corresponding algorithm refer to [Kirchengast et al., 2004a, b].

## 2.3 Influence of Layered Structures, Clouds and Turbulence

The retrieval of atmospheric parameters is influenced by various factors which affect the retrieval (occasionally even rendering it useless). Effects can stem from the atmosphere, from the instruments being used, or from constraints of the chosen retrieval method. Within the scope of this work, only atmospheric aspects, which at microwave frequencies are mostly connected to the varying amount of water vapour in the lower troposphere, will briefly be considered. For information on instrumental and retrieval errors as well as for more details on atmospheric effects refer to, e.g., [Kursinski et al., 1997, 2000, 2002], [Syndergaard, 1999], [Eriksson et al., 2001], [Foelsche and Kirchengast, 2004a, b], and [Nielsen et al., 2003].

### Influence of Layered Structures

Layered structures are marked by strong vertical changes in refractivity. They appear mainly in the troposphere and are primarily due to water vapour mixing ratio fluctuations. Layered structures often bring about multipath of signals passing through them. *Atmospheric multipath* refers to a situation where different signals superpose due to variations in the bending angle. As a result, various signals containing different phases and amplitudes simultaneously reach the receiver, which is why the signals have to be ungarbled in order not to misconstrue phase and amplitude variations not related to atmospheric bending and absorption.

Atmospheric multipath is caused by refractivity gradients increasing with altitude, the second derivative of  $N$  has to be smaller than zero ( $d^2N/dz^2 < 0$ ). Such variations in the refractivity arise mostly from sharp layers of moisture, but also from sharp temperature structures, wherefore atmospheric multipath frequently occurs in the lower troposphere. In order to avoid errors in the retrieval, multipath must be dealt with: For instance through a combination of back propagation to undo the ray path crossings and multisignal detection techniques, such as the Fourier Transform [Kursinski et al., 2002], or recent more powerful methods such as Canonical Transform [Gorbunov, 2002] and Fourier Spectral Inversion [Jensen et al., 2003]. Unfortunately, multipath cannot be handled if the retrieval is based on the geometrical optics approximation only (which is described in Sect. 2.2), but wave-optical methods are needed for the bending angle and transmission retrieval instead (see, e.g., [Nielsen et al., 2003], [Gorbunov and Kirchengast, 2004]).

### Influence of Clouds and Rain

Microwaves passing clouds and rain experience extinction (absorption and scattering) as well as phase delay. Generally, clouds consist of cloud droplets and/or

ice crystals. Because the radii of typical cloud droplets lie between 1 and  $50\ \mu\text{m}$ , their interaction with electromagnetic waves at frequencies around 22.23 GHz (water vapour absorption line) is well in the Rayleigh regime (radius  $\leq 0.05\lambda$ ). Thus, the scattering cross section is less than 0.2% of the absorption cross section [Nielsen et al., 2003], even for radii up to  $100\ \mu\text{m}$ . Therefore, scattering due to cloud droplets can be neglected. Ice crystals typically have sizes below  $100\ \mu\text{m}$ . So, radio waves around 22.23 GHz interacting with them are absorbed and scattered in the Rayleigh regime, too. Consequently, absorption of ice crystals is greater by more than 90% than scattering [Nielsen et al., 2003]. Since the absorption by ice crystals additionally is about two orders of magnitude smaller than that of cloud droplets, the scattering from ice crystals can be neglected, too. As a result, the extinction due to clouds can be expressed by absorption only.

Because the absorption cross section is proportional to the particle volume and independent from the particle size, the cloud extinction is characterized only by the content of liquid water and ice water. If the extinction by clouds is not too large and the transmission is above the detection limit and if sufficient rays are available, liquid and ice water content depending on height can be retrieved from amplitude measurements. This knowledge can then be used in weather and climate sciences. Finally, it should be mentioned that the detection limit of clouds depends on the frequencies being used as well as on the cloud properties (see, e.g., [Gradinarsky et al., 2003]).

In the case of rain, scattering cannot be neglected anymore because rain drops range from about  $50\ \mu\text{m}$  up to about 2.5 mm. In fact, for frequencies around 22.23 GHz scattering dominates the extinction by rain drops. In contrast to cloud droplets, the extinction coefficient is therefore mainly defined by the drop size distribution. In practice, sufficiently heavy rain (generally happening below 3 km) will lead to strong signal attenuation and renders the amplitude signal unusable for retrieval.

### **Influence of Turbulence**

Turbulence is an irregular motion of air parcels, which is caused either by motions in the atmospheric boundary layer, or by convection in the free troposphere, or by orographic patterns. It leads to random variations of the refractive index, which in turn cause fluctuations in phase and amplitude of crossing rays, so-called *scintillations*. Particularly, dry air tropospheric scintillation is distinguished from wet air tropospheric scintillation, which refers to a situation with rain being present, too. Scintillations have an adverse effect on the retrieval results, which cannot be eliminated but mitigated — e.g. by down-weighting of the imaginary refractivity information combined with use of additional information (*best-fit temperature extrapolation*, see Subsect. 4.2.4 p. 72) and by wave-optics processing, which is able to reduce fluctuations already on the transmissions (see [Gorbunov and Kirchengast, 2004]). In the worst case, if severe signal amplitude fluctuations occur due to strong

turbulence, it will not be possible to exploit amplitude information. Generally, such cases will happen in the lower troposphere only.

### Other Atmospheric Effects

Finally, we will have a quick look at some other important atmospheric influence factors: diffraction, defocussing and critical refraction.

Since the light propagation results from the superposition of spherical radiators (Fresnel-Huygens concept), atmospheric structures smaller than the diameter of the first fresnel zone will alter phase and amplitude of these spherical waves. Vertical resolution will thus be affected. This effect is called *diffraction* and is determined by the signal frequency, the observing geometry as well as the atmospheric bending. Unfortunately, diffraction effects cannot be completely taken into account since current inversion methods are based on the ray impact parameter description. But very effective reduction of diffraction effects is possible, in geometrical optics processing via the ratio of amplitudes combined with smoothing; wave optics methods reduce refraction intrinsically, without additional treatment, and are clearly preferable for this purpose (e.g., [Gorbunov and Kirchengast, 2004]).

*Defocussing* is attributable to changes of vertical refractivity gradients (i.e., the second derivative of  $N$ ), which cause differential bending and therefore divergence (or sometimes convergence) between adjacent, initially parallel ray paths. Accordingly, the signal intensity of rays entering a region where bending increases downwards will be attenuated. Furthermore, defocussing is connected to vertical water vapour mixing ratio fluctuations and therefore it is a sensitive measure of the local refractivity scale height and humidity fluctuations [Kursinski et al., 2000]. Because, besides absorption, defocussing leads to an additional damping of the signal intensity, it is essential to remove this effect during the retrieval procedure, as done in Subsection 2.2.1.

If a signal ray path curves down into the earth's surface, this is called *critical refraction*. This effect is a consequence of a large vertical refractivity gradient (particularly  $dN/dz < -10^6/R_c$ ), which causes the radius of local curvature ( $R_c$ ) of the ray to be smaller than that of the atmosphere. Consequently, the ray cannot be observed. The main reason for critical refraction is a strong water vapour gradient, appearing mainly at the top or within the atmospheric boundary layer. Indeed, the influence of pressure and temperature gradients alone would be incapable to generate critical refraction (e.g., [Sokolovskiy, 2004]).

## 2.4 Important Properties for Atmosphere and Climate Science

The LEO-LEO and, to a lesser degree, the GNSS-LEO radio occultation technique possess a lot of unique features which are essential for atmosphere and climate research. The main characteristics are (according to [ESA, 2004a]):

- high absolute accuracy and long term stability of humidity, temperature, and pressure data due to ...
- ...intrinsic self-calibration of occultation data (Doppler shift and transmission)
- high vertical resolution of fine structures in the atmosphere
- global and even coverage with globally consistent high quality profiles, over both oceans and land
- nearly all-weather capability due to long probing wavelengths ( $> 1$  cm)
- independent measurement of humidity, temperature, and pressure vertical profiles in the free troposphere by X/K-band occultations
- radio occultation data can be used as reference data and do not need to be inter-calibrated with follow-on and non-overlapping radio occultation missions

The earth's climate is (very likely) changing, which clearly shows up in the temperature field: the global mean surface temperature is increasing, whereas the stratospheric temperature tends to decrease. Analogous to the surface temperature, the atmospheric water vapour content is growing (see [Houghton et al., 2001]). Unfortunately, the processes and feedbacks (particularly the water vapour feedback, depicted in Section 1.3) causing variations and changes in climate are still poorly understood. The main reason for this lies in the lack of high quality data of atmospheric temperature, water vapour, and pressure fields; conventional measurement methods do not have the required accuracy, resolution, and coverage in order to establish the required climatologies. Thanks to the features mentioned above, this does not apply to the GNSS/LEO-LEO radio occultation technique, which would be able to provide the data needed to identify and quantify climatic processes and feedbacks. This knowledge can then be used in order to improve climate models (better parameterization via data assimilation, etc.) which subsequently allow to make improved climate predictions. Furthermore, if data are available over a sufficiently long period, climate variability, trends, and changes can be detected.

The accurate data provided by the radio occultation technique can also be used in order to investigate the physics of specific atmospheric phenomena: for example the

exchange between the stratosphere and the troposphere, the thermodynamic structure and dynamical evolution of the winter polar vortices, the depth and thermodynamic structure of boundary layers, the sources, sinks, and coupling mechanisms of gravity waves, and many more. The findings can be included into weather and atmosphere models. All in all, the GNSS/LEO-LEO radio occultation supports the research for a better understanding of the earth's atmosphere and climate.

Besides the applications mentioned above, radio occultation measurements are of use for ionospheric and space physics, too. For more detailed information on the use of GNSS/LEO-LEO radio occultations see, e.g., [Kursinski et al., 1997], [Kirchengast and Høeg, 2004], and [ESA, 2004a].



# Chapter 3

## The ACE+ Mission

This chapter gives an insight into the *Atmosphere and Climate Explorer* mission ACE+. Section 3.1 comprises background information and Section 3.2 includes the scientific justification of this mission. The mission objectives are summarized in Section 3.3 followed by the description of the measurement methodology (Sect. 3.4) and the mission requirements (Sect. 3.5). Detailed information about the ACE+ mission can be found in, e.g., [Høeg and Kirchengast, 2002], [Kirchengast and Høeg, 2004], and [ESA, 2004a, b, c].

### 3.1 General Information

The ACE+ mission consists of four Low Earth Orbit (LEO) satellites which carry out GPS-LEO, GALILEO-LEO and LEO-LEO radio occultation in order to retrieve atmospheric parameters like pressure, temperature, and humidity profiles throughout the troposphere and the stratosphere with unprecedented accuracy. It was mainly conceived for applications in climate research. The aims include, among others, the quantification of climate variability and trends as well as the better understanding of climate feedbacks and external forcing variations. The features of the radio occultation technique such as high resolution, global and even coverage, and long term stability of the measurements (see Sect. 2.4) will thereby be the deciding factors. The novel aspect of ACE+ is the use of LEO-LEO radio occultation which was never put into practice before as well as the use of GALILEO signals for occultation measurements.

ACE+ is a mission led by P. Hoeg from the Danish Meteorological Institute (DMI) in Copenhagen (now at the Aalborg University) and G. Kirchengast from the Institute for Geophysics, Astrophysics and Meteorology (IGAM) at the University of Graz. Scientists from all over the world form an international science team. The development of the ACE+ concept benefited from the experience of several previous missions (like GPS/MET, SAC-C, CHAMP, METOP; see Table 2.1) and

mission proposals. The GNSS-LEO occultation part was inherited directly from the ACE (Atmosphere and Climate Experiment, [Høeg and Leppelmeier, 2000]), the ACLISCOPE (Atmosphere and Climate Sensors Constellation Performance Explorer, [Kirchengast et al., 1998]) and the APM (Atmospheric Profiling Mission, [ESA, 1998]) mission proposals. Concerning the novel LEO-LEO part, the concept of the preceding WATS mission proposal ([ESA, 2001]) was adopted.

Within the scope of the ESA *Living Planet Programme*, ACE+ was selected among 25 proposed missions as the top priority future *Earth Explorer Opportunity Mission* in May 2002. Contrary to expectation, ACE+ was apparently for programmatic and cost reasons not proceeded into phase B after the phase A studies (including technical and scientific feasibility studies). In May 2004 another mission, SWARM (a mission focused on the earth's magnetic field, [ESA, 2004d]), was proceeded by ESA into phase B and for implementation. Nevertheless, ACE+ is now ready for implementation thanks to the successful feasibility studies [ESA, 2004a, b].

## 3.2 The Need for ACE+

In this section, the most important reasons why a mission like ACE+ is absolutely desirable will be considered. A more comprehensive presentation can be found in [Kirchengast and Høeg, 2004].

As confirmed in the latest IPCC scientific assessment report [Houghton et al., 2001], the twentieth century was characterized by a warming trend of the mean global surface temperature. Whereas the majority of this warming is attributable to natural processes like solar and internal climate variability, the warming during the last twenty years of this century cannot be explained without the contribution of the increasing concentration of greenhouse gases mainly owing to human activities. In the future, the mean surface temperature will continue to go up, just as the atmospheric water vapour content.

Currently, the increase of the mean global surface temperature is estimated to be between  $1.4^\circ$  and  $5.8^\circ$  over the twenty-first century. On the one hand, the large span of this assessment is attributable to different scenarios underlying the climate models, accounting for future developments of economic and social aspects. On the other hand, the poorly understood internal feedbacks — above all those associated with water vapour — give rise to uncertainties in the climate models, too. Therefore, it is essential to enhance the knowledge about the mechanisms of water vapour in order to improve the understanding of climatic feedbacks defining the magnitude of climate change and the inter-annual variations in external forcing [Høeg and Kirchengast, 2002]. This can be achieved through accurate and highly resolved measurements of the global temperature and water vapour fields.

Water vapour and temperature are very important in controlling the atmospheric circulation. In particular, the influence of water vapour is chiefly due to conden-

sation and evaporation processes which drive several global and local atmospheric circulation phenomena. Furthermore, the water vapour's radiation properties are of great significance, too, since water vapour is the most important greenhouse gas. Water vapour participates in most atmospheric processes, but its mechanisms in climate change remain poorly understood. The main reason for this is the inadequacy of conventional measurement methods concerning observational accuracy, temporal and spatial resolution, long-term stability, and vertical coverage. The necessity of precise water vapour measurements becomes clear considering the uneven distribution and high variability of this atmospheric constituent (see Fig. 3.1 and Fig. 3.2), which stems from its short residence time in the atmosphere.

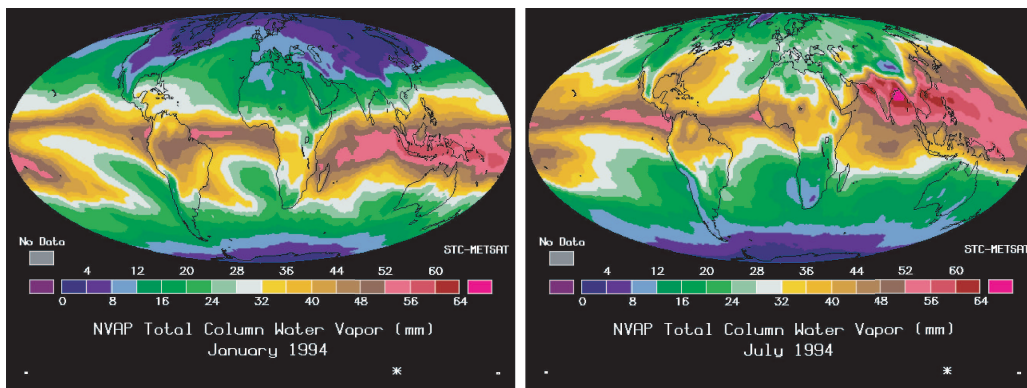


Figure 3.1: Exemplary global distribution of the vertical-column water vapour content in January (left) and July (right). Shown is the 1994 monthly mean. Source: NASA Water Vapor Project CD-Rom; Sci&Tech Corp., 1997.

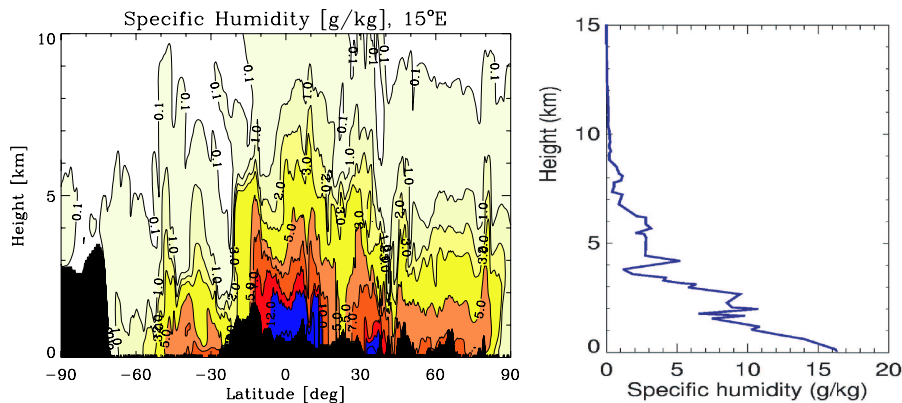


Figure 3.2: Exemplary vertical distribution of the specific humidity. Left panel: Latitude-height slice from an ECMWF analysis, September 15, 1999, 12 UTC, 79 W. Right panel: RAOB profile from Kauai, Hawaii, October 1, 2000, 12 UTC. Source: [Foelsche and Kirchengast, 2004a] (left figure) and S. Leroy/JPL, 2001 (right figure).

As indicated above, precise and global, evenly distributed, long-term stable observations of the present temperature and humidity distributions including their variability would enhance the knowledge of the climate mechanisms. This would benefit to climate change research (improved monitoring, modelling, analysis and prediction of the climate change) as well as to weather forecast. Thanks to the combined use of the GNSS-LEO and the novel LEO-LEO occultation technique, which are marked by their self-calibrating nature (see Sect. 2.4), ACE+ is the single mission which is able to yield such data at the moment. The extensive database from the mission will lead to a better understanding of climatic feedbacks and to a better assessment of the climate change.

### 3.3 Scientific Mission Goals

ACE+ is mainly conceived for applications in climate research, but other scientific fields such as weather and ionosphere research will profit, too. For that reason, there is a distinction between primary mission goals that drive the mission, secondary mission goals which are accounted for with as much dedication as possible, and spin-off benefits which are accounted for on a best-effort basis. A synopsis of the scientific objectives (taken from [ESA, 2004a, c]) will here be given.

#### Primary Mission Goals

The primary mission goals comprise all topics which are of greatest interest within the scope of the mission. These are:

- monitoring of climate variability and trends as an initial key component of long-term occultation observations of climate
- contribution to detection of climate changes and support of climate change predictions via provision of high-quality global reference data
- validation of Global Circulation Models (GCMs), both in terms of simulated mean climate and variability
- improvement, via data assimilation methods, of physics parameterizations in GCMs and of the detection of external forcing variations
- improvement of the understanding of climate feedbacks determining magnitude and characteristics of climate changes
- study of structures in troposphere and tropopause regions at high vertical resolution; in the context of atmospheric process research
- demonstration of the novel LEO-LEO occultation technique

- demonstration of the novel use of GALILEO-LEO occultation

Moreover, the understanding of several atmospheric physics and climate change processes can be improved addressing issues such as:

- global climate warming and related changes in atmospheric water vapour levels
- tropical heat and mass exchange with extra-tropical regions
- transport across subtropical mixing barriers, relevant for information on the lifetime of greenhouse gases
- stratospheric temperatures and atmospheric wave phenomena
- stratospheric temperature trends
- polar front dynamics and mass exchange together with tropospheric water vapour feedback on climate stability
- high latitude tropospheric-stratospheric exchange processes related to polar vortex conditions
- climatology of Rossby waves and atmospheric internal waves

Each of the primary mission goals is supposed to be achieved through the measurement, analysis, and interpretation of the highly precise temperature, humidity and pressure data fields provided by the ACE+ mission complemented by other suitable information.

### **Secondary Mission Goals**

The secondary mission objectives contain issues which are very important, but are not driving the mission. They will be addressed as good as possible with the available resources. The following topics are concerned:

- contribution to improved numerical weather prediction (NWP)
- support of analysis, validation, and calibration of data from other space missions

These tasks are also supported by the highly accurate data set established from the ACE+ occultation observations.

### Spin-off Benefits

The following issues will be explored on a best-effort basis, because the mission design makes them possible:

- ionospheric climate and weather, and space weather investigations using the electron density data provided by ACE+
- assessment and improvement of present water vapour attenuation models
- investigation of turbulence and its products in the lower troposphere

For a detailed explanation of these goals see, e.g., [ESA, 2004a, c].

## 3.4 Measurement Concept

This section aims at giving an overview of the operation mode of the ACE+ system. First, in Subsection 3.4.1 the system concept comprising spacecrafts, their instrumentation and ground segment will be described. Afterwards, the observation methodology, which is based on GNSS-LEO and LEO-LEO radio occultation, will be considered (see Subsect. 3.4.2). [ESA, 2004a, and b] were used as main source for this summary description.

### 3.4.1 Generic System Concept

The ACE+ mission consists of four small satellites which are launched into two different low earth orbits with two satellites each. In order to enable the LEO-LEO occultation, the satellites of the higher orbit must move in the opposite direction than those of the lower orbit. In regard to adequate inter-satellite visibility as well as to global and even coverage of the LEO-LEO occultation measurements, the following constellation geometry has proven to be favourable:

- two orbital planes with two satellites each
- two orbit altitudes:  $\sim 800$  km (transmitter satellites) and  $\sim 650$  km (receiver satellites)
- transmitter satellites counter-rotating versus receiver satellites
- sun-synchronous orbits (inclination  $\sim 98^\circ$ )
- transmitter separation angle (within the orbit) of  $\sim 180^\circ$

- receiver separation angle (within the orbit) of  $\sim 80^\circ$
- antenna field of view of  $< 10^\circ$  azimuth and steerable boresight

This constellation of which an artistic view is shown in Figure 3.3 yields about 230 LEO-LEO occultation events (setting and rising) a day and more than 7000 events a month (cf. Fig. 4.3).

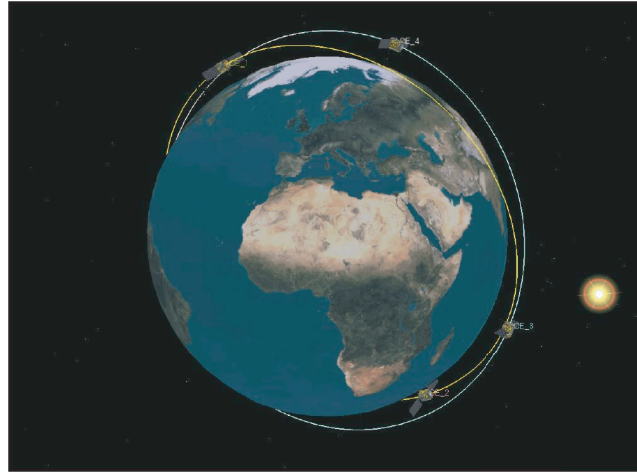


Figure 3.3: Exemplary ACE+ satellite constellation concept. Source: [ESA, 2004b].

The four ACE+ spacecraft are more or less identical but with different payloads. The satellites in the higher orbit have the capability to transmit microwave signals which are received by the lower ones. In addition, there are GNSS-LEO receivers on all spacecraft. More precisely, the main instruments are:

- GRAS-2, a specialized L-band receiver for GPS-LEO and GALILEO-LEO radio occultation measurements in the troposphere and stratosphere. Schematic and artistic illustrations of the GRAS-2 antenna, which is the successor of the GRAS instrument on MetOp, are shown in Fig. 3.4.
- LRO instrument, a LEO-LEO radio occultation instrument composed of transmitters, receivers, and antennae for X/K-band LEO-LEO radio occultation measurements. A schematic view of LRO transmitter and receiver is shown in Fig. 3.5.

Detailed information on the instruments and their performance can be found in [ESA, 2004b]. Because all four ACE+ satellites should be able to make GNSS-LEO radio occultation each spacecraft has to be equipped with a GRAS-2 receiver and related antennae. The LRO instruments, however, vary from satellite to satellite; the transmitters in the higher orbit carry an LRO transmitter and the receivers in the lower orbit an LRO receiver.

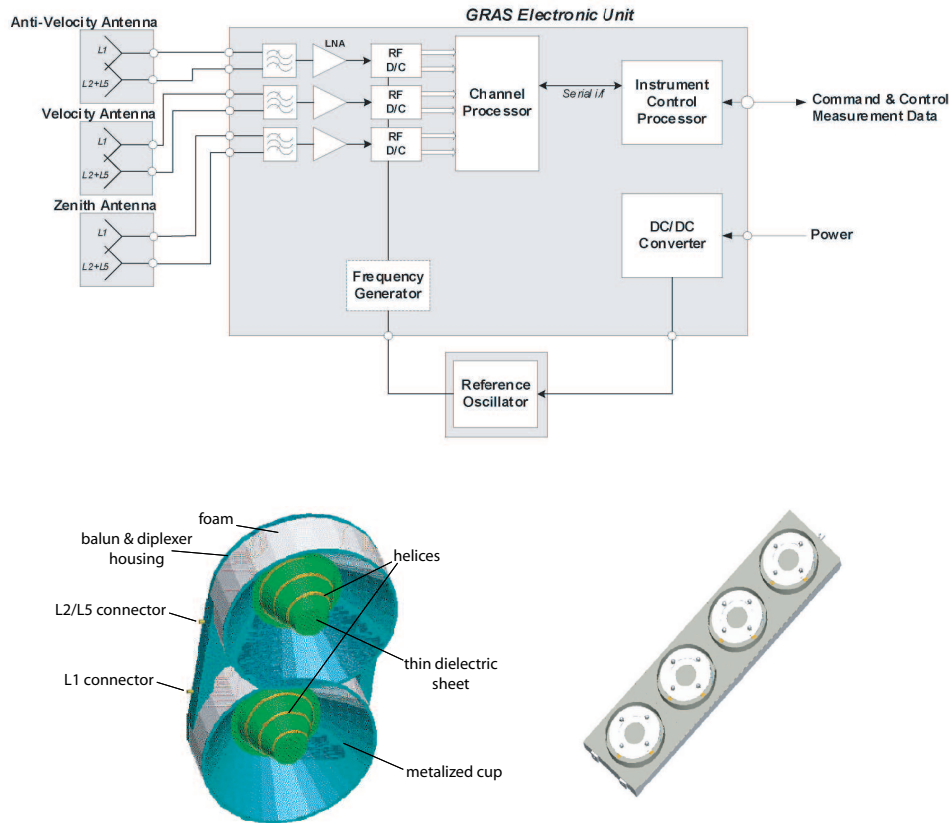


Figure 3.4: General GRAS-2 architecture (upper panel) and two options proposed for the GRAS-2 radio occultation antennae (lower panels). Source: [ESA, 2004b].

The ground segment will be based on the infrastructure being established within the scope of other satellite missions. It consists of three main parts: the Command and Data Acquisition Element (CDAE), the Mission operations and Satellite Control Element (MSCE) and the Processing and Archiving Element (PAE). The assignment of the CDAE is to receive and check all satellite commands and telemetry data. Afterwards, the formatted data (i.e., carrier phases and amplitudes, clock data, earth orientation data, etc.) are delivered to the PAE. There, the data are processed into the mission products (i.e., profiles of complex refractivity, temperature, humidity, etc., and corresponding error estimates), archived and distributed to the end user community. Users will be above all scientific institutions, but also public services, environmental agencies, industry and international user communities. The MSCE serves to classical functions such as the overall mission planning and coordination, satellite monitoring and control, on-board software maintenance and many more. For further information on the ground segment and a detailed description of the data processing see [ESA, 2004b].

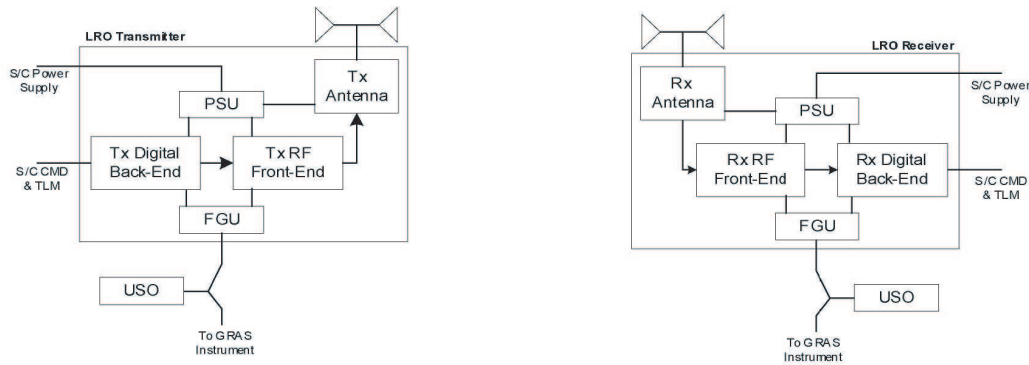


Figure 3.5: General architecture of the LRO instrument. The receiver is shown in the left panel, the transmitter in the right one. Source: [ESA, 2004b].

### 3.4.2 Observation Methodology

The measurement principle of ACE+ is based on a combination of GPS-LEO, GALILEO-LEO, and LEO-LEO radio occultation. A schematic illustration is shown in Fig. 3.6. Because the principles of the radio occultation technique have already been described in Chapter 2, only the specific characteristics of ACE+ will briefly be mentioned.

Each of the four LEO satellites is able to perform GNSS-LEO radio occultation. Assuming that all 24 GPS and 30 GALILEO satellites are active, more than 4500 occultation events a day will be performed, which are globally uniformly distributed around the globe with a horizontal resolution of about 300 km (see Fig. 3.7). The GNSS-LEO occultation yields parameters of the neutral atmosphere throughout the troposphere and stratosphere as well as the electron density of the ionosphere. Concerning the neutral atmosphere, profiles of temperature can accurately be retrieved when the humidity is low (dry air), such as in the stratosphere and the upper troposphere. In the more humid lower troposphere, however, either water vapour or temperature can be retrieved, but only if the other parameter is known from external sources. This introduces slight inaccuracies. Typically, the altitude of the border between dry and humid air varies from 6–8 km in the tropics down to  $\sim 1$ –4 km in polar regions.

With regard to climate change monitoring, the refractivity, geopotential height, and dry-temperature data provided by the GNSS-LEO occultation are very promising. For example, dry-temperature can be retrieved accurately to  $\leq 1$  K within about 5–35 km (see Fig. 3.8) with a vertical resolution of less than 1 km. The performance of the GNSS-LEO technique has already been proved extensively in the past, for instance within the scope of missions as GPS/MET and CHAMP. Literature about this exists in, e.g., [Rocken et al., 1997], [Steiner et al., 2001], [Steiner and Kirchengast, 2004], and [Wickert, 2004].

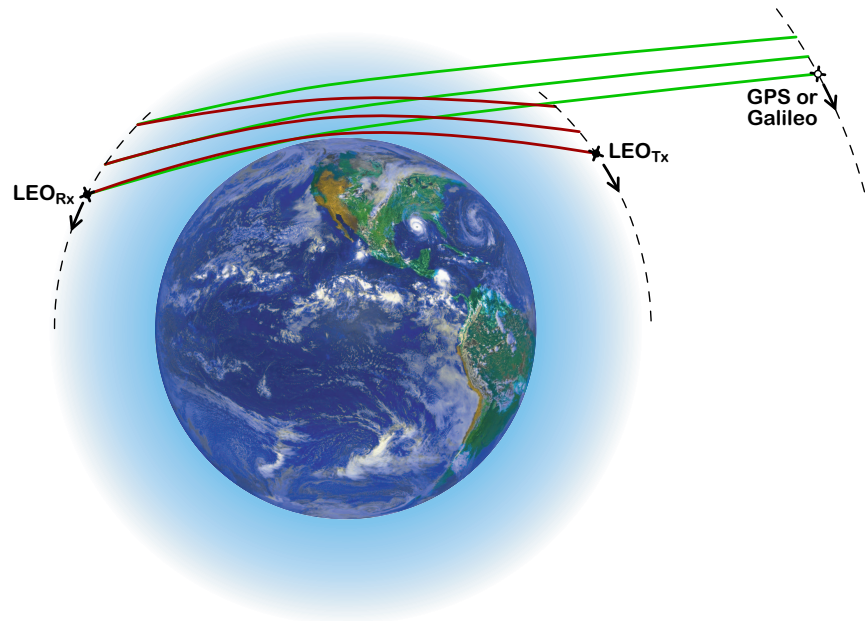


Figure 3.6: Schematic view of the ACE+ observation geometry for LEO-LEO crosslink occultation as well as GPS-LEO and GALILEO-LEO occultation. Occultation events are quasi-vertical scans through the atmosphere occurring due to the satellite motions.

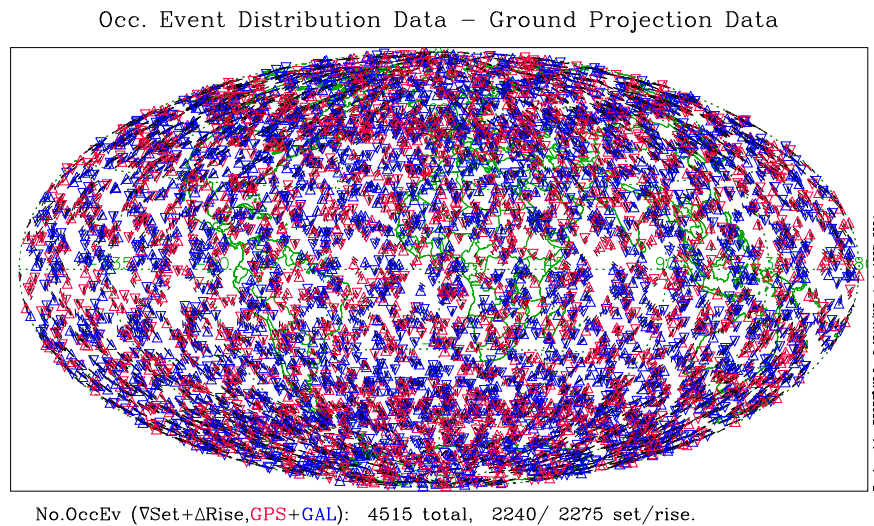


Figure 3.7: ACE+ GNSS-LEO occultation event coverage during one day. The red triangles indicate GPS-LEO events and the blue ones GALILEO-LEO events. Source: J. Ramsauer/IGAM, 2004.

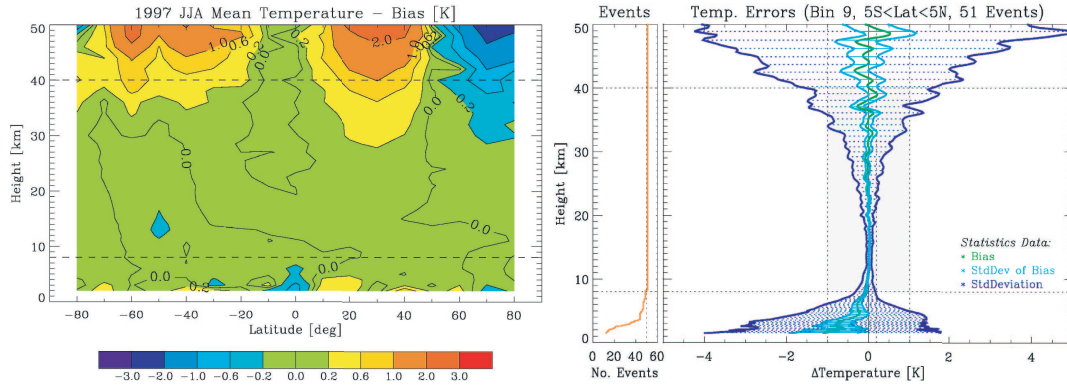


Figure 3.8: Illustration of the temperature retrieval performance using GNSS-LEO occultation data. Left panel: Latitude-Height slice of climatological residual bias errors in average profiles of dry temperature in 17 latitude bins of  $10^\circ$  width from  $80^\circ\text{S}$  to  $80^\circ\text{N}$ . Each average profile involves about 50 realistically simulated individual GNSS-LEO occultation profiles sampled by an ACE+-type satellite constellation within a full summer season (June–August). Right panel: Vertical error structure at the equator. Statistical performance result of 51 occultation events. Source: [Gobiet and Kirchengast, 2004] (left figure), A. Gobiet/IGAM, pers. communications, 2004 (right figure).

In addition to the GNSS-LEO occultation LEO-LEO occultation will be performed between the transmitter satellites in the higher low earth orbit and the receiver satellites in the lower one. In order to allow independent accurate measurements of humidity within the lower and upper troposphere, three frequency channels near the center and at the wing of the 22.23 GHz water vapour absorption line (nominally placed at 9.7, 17.25 and 22.6 GHz) will be used. Figure 3.9 shows the atmospheric absorption within this frequency range. As can be seen, water vapour dominates the absorption, but besides the ambient air (molecular oxygen and nitrogen), cloud liquid water contributes, too. That is why three frequencies are needed in order to enable the removal — if necessary — of the liquid water effect. In such a case the corresponding liquid water profile would be obtained as a by-product.

The selection of the three ACE+ frequencies complied with the following demands: The microwave cross-links must handle the expected water vapour absorption while delivering the required measurement precision [ESA, 2004a]. Since the humidity concentration is small in the upper troposphere, a signal that is very sensitive to its absorption has to be chosen in order to get measurements with sufficient precision. The frequency of 22.6 GHz is well suited for this. By contrast, the partially high water vapour abundances within the lower troposphere require less strongly absorbed signals in order to ensure that the received signal is sufficiently strong even under very moist and cloudy conditions. For this, the lower frequencies at 9.7 and 17.25 GHz are essential.

The LEO-LEO occultation is expected to deliver independent measurements of humidity and temperature throughout the free troposphere with unprecedented accuracy. A performance analysis of the retrieved data under clear, cloudy as well as under cloudy and turbulent air conditions will be subject of Chapters 4 and 5. Extensive analysis regarding instrumental errors have already been performed by, e.g., [Kirchengast et al., 2004b]. A general performance overview of both GNSS-LEO and LEO-LEO radio occultation in the ACE+ constellation can be found in [Kirchengast et al., 2004a]. A recent performance analysis based on wave-optics processing was performed by [Gorbunov and Kirchengast, 2004].

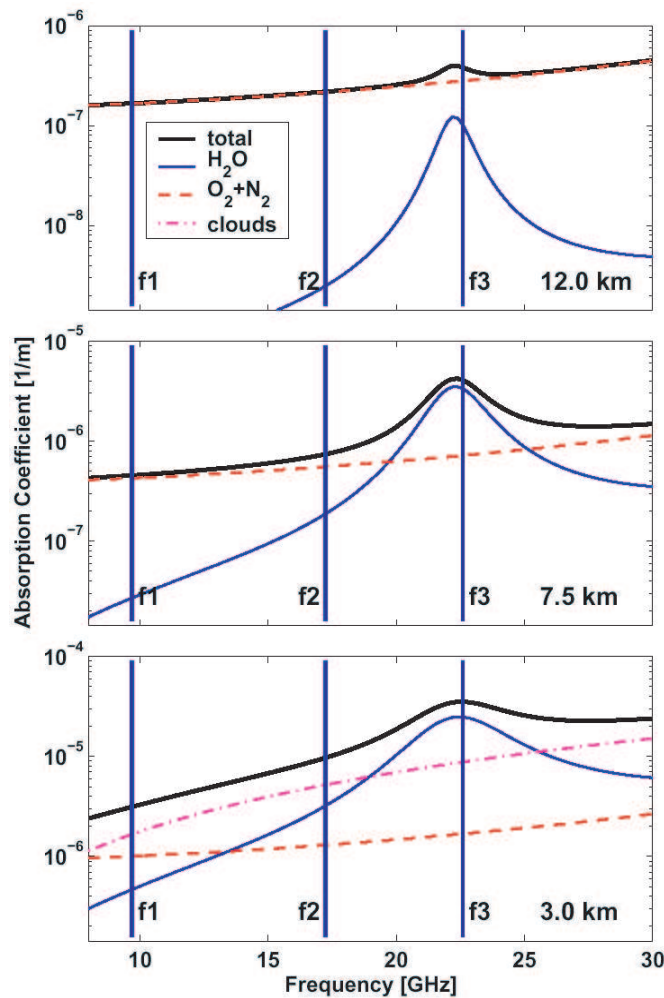


Figure 3.9: Atmospheric absorption coefficients as a function of frequency at three different heights (3 km, 7.5 km, 12 km) for a mid latitude summer atmosphere. The three ACE+ baseline frequencies are indicated. In addition to total absorption, water vapour (H<sub>2</sub>O), ambient air (O<sub>2</sub> and N<sub>2</sub>), and liquid water (cloud; lowest panel) absorption are also shown. Source: P. Eriksson/Chalmers University of Technology, 2004.

## 3.5 Observational Requirements

This section contains an overview of the ACE+ specific observational requirements. For more detailed information see the ACE+ Mission Requirements Document [ESA, 2004c].

Since the main objectives of ACE+ focus on climate research, the provided data has to fulfill the high demands needed for this purpose. The deciding factors are first long-term stability and high accuracy; high vertical resolution and global coverage are also very important properties. Thus, with the specific mission objectives in mind, the observational requirements on the main data products of ACE+ (tropospheric humidity as well as tropospheric and stratospheric temperature) have been drawn up on the basis of the generic requirements proposed by the WMO (see [ESA, 2004a] and references therein). The results are shown in Tables 3.1 and 3.2 summarizing the requirements on the LEO-LEO occultation and the GNSS-LEO occultation part, respectively. The key word *target* refers to the desired performance and *threshold* stands for the minimum performance needed in order to achieve the mission goals.

The specific requirements listed in Tables 3.1 and 3.2 are broken down into atmospheric layers according to WMO specifications as follows:

Lower Troposphere	LT	1000–500 h Pa	approx. surface – 5 km
Higher Troposphere	HT	500–100 h Pa	approx. 5–15 km
Lower Stratosphere	LS	100–10 h Pa	approx. 15–35 km
Higher Stratosphere	HS	10–1 h Pa	approx. 35–50 km

		Specific Humidity		Temperature	
		target	threshold	target	threshold
Horizontal domain		global			
Horizontal sampling (mean distance of adjacent profiles) to be achieved within:		700 km	1600 km	700 km	1600 km
Time sampling		24 hrs			
No. of profiles per grid box <sup>1)</sup> per month		40	30	40	30
Vertical domain <sup>2)</sup>		TBL <sup>3)</sup> to 15 km	5 to 12 km	TBL <sup>3)</sup> to 50 m	5 to 40 km
Vertical sampling	LT	0.5 km	1 km	0.5 km	1 km
	HT	0.5 km	1 km	0.5 km	1 km
	LS	-	-	0.5 km	1 km
	HS	-	-	1 km	5 km
RMS accuracy <sup>4)</sup>	LT <sub>TBL</sub>	0.6 g/kg	1 g/kg	1 K	2 K
	LT <sub>top</sub>	0.2 g/kg	0.4 g/kg	1 K	2 K
	HT <sub>top</sub>	0.003 g/kg	0.025 g/kg	0.5 K	1 K
	LS	-	-	0.5 K	1 K
	HS	-	-	1.5 K	3 K
Long-term stability		2 % RH <sup>5)</sup> per decade	3 % RH <sup>5)</sup> per decade	0.1 K per decade	0.15 K per decade
Timeliness	climate NWP <sup>6)</sup>	30 days	60 days	30 days	60 days
		1.5 hrs	3 hrs	1.5 hrs	3 hrs
Time domain <sup>7)</sup>		5 years			

<sup>1)</sup> Grid box defined as square of horizontal sampling requirement.

<sup>2)</sup> Below about 3 km (typical atmospheric conditions) to 6 km (severe scintillation/clouds), retrievals may involve weak prior temperature information to separately derive humidity and temperature from refractivity/absorption.

<sup>3)</sup> Top of atmospheric boundary layer, located typically 1–2.5 km above the surface.

<sup>4)</sup> Understood to be the accuracy at a vertical resolution consistent with the required sampling (i.e., a resolution of  $2\times$  vertical sampling [km]). The humidity accuracy requirement decreases linearly between the specified values at  $LT_{TBL} = 2$  km and  $LT_{top} = 5$  km; decreases logarithmically from  $LT_{top} = 5$  km to  $HT_{top} = 10$  km; above constant. The temperature accuracy requirement is constant between  $LT_{TBL}$  and  $LT_{top}$ ; decreases linearly from  $LT_{top}$  to  $HT_{top}$  value at 10 km; above constant.

<sup>5)</sup> Stability is specified for Relative Humidity (RH) here, a quantity with well-defined and linear range over the vertical domain. There are standard formulae to convert between RH and specific humidity as functions of temperature and pressure.

<sup>6)</sup> NWP is a secondary mission objective. However, often NWP analyses are used for the forcing of climate GCM runs. Therefore, the climate mission objectives would benefit if this timeliness requirement would be fulfilled.

<sup>7)</sup> Climate change detection and monitoring requires long-term observations over decades. ACE+ should thus be followed by similar missions.

Table 3.1: LEO-LEO observational requirements (after [ESA, 2004a]).

		Specific Humidity		Temperature	
		target	threshold	target	threshold
Horizontal domain		global			
Horizontal sampling (mean distance of adjacent profiles) to be achieved within:		100 km	700 km	100 km	700 km
Time sampling		12 hrs			
No. of profiles per grid box <sup>1)</sup> per month		50	40	50	40
Vertical domain <sup>2)</sup>		TBL <sup>3)</sup> to 10 km	2.5 to 5 km	TBL <sup>3)</sup> to 50 km	5 to 40 km
Vertical sampling	LT	0.5 km	1 km	0.5 km	1 km
	HT	0.5 km	1 km	0.5 km	1 km
	LS	-	-	0.5 km	1 km
	HS	-	-	1 km	5 km
RMS accuracy <sup>4)</sup>	LT <sub>TBL</sub>	0.6 g/kg	1 g/kg	1 K	2 K
	LT <sub>top</sub>	0.2 g/kg	0.4 g/kg	1 K	2 K
	HT <sub>top</sub>	0.1 g/kg	0.2 g/kg	0.5 K	1 K
	LS	-	-	0.5 K	1 K
	HS	-	-	1.5 K	3 K
Long-term stability		2 % RH <sup>5)</sup> per decade	3 % RH <sup>5)</sup> per decade	0.1 K per decade	0.15 K per decade
Timeliness	climate NWP <sup>6)</sup>	30 days	60 days	30 days	60 days
		1.5 hrs	3 hrs	1.5 hrs	3 hrs
Time domain <sup>7)</sup>		5 years			

<sup>1)</sup> Grid box defined as square of horizontal sampling requirement.

<sup>2)</sup> Below about 5 km (dry conditions) to 12 km (moist tropical conditions), retrievals will involve prior information to separately derive humidity and temperature from refractivity.

<sup>3)</sup> Top of atmospheric boundary layer, located typically 1–2.5 km above the surface.

<sup>4)</sup> Understood to be the accuracy at a resolution consistent with the required sampling (i.e., a resolution of  $2 \times$  vertical sampling [km]). The humidity accuracy requirement decreases linearly between the specified values at  $LT_{TBL} = 2$  km and  $LT_{top} = 5$  km; decreases logarithmically from  $LT_{top} = 5$  km to  $HT_{top} = 10$  km; above constant. The temperature accuracy requirement is constant between  $LT_{TBL}$  and  $LT_{top}$ ; decreases linearly from  $LT_{top}$  to  $HT_{top}$  value at 10 km; above constant.

<sup>5)</sup> Stability is specified for Relative Humidity (RH) here, a quantity with well-defined and linear range over the vertical domain. There are standard formulae to convert between RH and specific humidity as functions of temperature and pressure.

<sup>6)</sup> NWP is a secondary mission objective. However, often NWP analyses are used for the forcing of climate GCM runs. Therefore, the climate mission objectives would benefit if this timeliness requirement would be fulfilled.

<sup>7)</sup> Climate change detection and monitoring requires long-term observations over decades. ACE+ should thus be followed by similar missions.

Table 3.2: GNSS-LEO observational requirements (after [ESA, 2004a]).



# Chapter 4

## ACE+ Performance Analysis Simulations

The objective of the performance analysis made within the scope of this work is an assessment of the accuracy of temperature and humidity profiles retrieved from LEO-LEO occultation data in the ACE+ constellation. The focus lies on the retrieval performance under different clear, cloudy, and cloudy and turbulent air conditions. For this purpose, a variety of end-to-end simulations of occultation events have been performed using geometric-optics processing within EGOPS5 (version E5.0.4r1) — a simulation tool allowing for LEO-LEO occultation simulation and subsequent profiles retrieval which was developed within the scope of the ACE+ phase A (ACEPASS study, [Kirchengast et al., 2002b]). To be precise, 22 sets of occultation events, each with 40 or more ensemble members, accounting for different atmospheric conditions were prepared and processed for this work. The resulting temperature and humidity profiles of each set were compared with the original atmospheric data (“true” profiles) and statistically analyzed. Finally, the results of this analysis were compared with each other and discussed.

A detailed description of the analysis method is the subject of Section 4.3. The preceding Sections 4.1 and 4.2 give insight into the applied simulation tool EGOPS5. The performance analysis results will be presented subsequently in Chapter 5. The analysis and results further expand work reported in [Schweitzer et al., 2003], [Kirchengast et al., 2004a, b], and [ESA, 2004a].

### 4.1 The Simulation Tool EGOPS5

The *End-to-end Generic Occultation Performance Simulator, version 5* (EGOPS5), is a powerful tool which enables simulation of LEO-LEO as well as GNSS-LEO radio occultation measurements and subsequent processing of the data products towards atmospheric and ionospheric profiles. Data of real observations can be processed,

too. EGOPS5 was developed within the scope of the ACE+ phase A (ACEPASS study, [Kirchengast et al., 2002b]) and is an extension and advancement of EGOPS4 (see, e.g., [Kirchengast, 1998] and [Kirchengast et al., 2002a]) which did not contain the LEO-LEO occultation part yet.

The basic idea behind EGOPS is to support research addressing scientific and technical questions on the GNSS/LEO-LEO based radio occultation technique. This purpose requires modelling and simulation of numerous components and processes relevant to real radio occultation in the simulator's world. Thus, EGOPS treats as many aspects of the GNSS/LEO-LEO radio occultation as possible within a flexible and user friendly environment open for continuous enhancements. By means of EGOPS, diverse issues concerning the radio occultation technique can be investigated; for example the impact of geometrical (e.g., satellite constellation) and technical (e.g., antenna specifications) aspects on the coverage, the influence of atmospheric and instrumental properties on data quality, end-to-end error budgets, etc. Altogether, EGOPS is able to contribute significantly to a better quantification of the potential of the GNSS/LEO-LEO radio occultation technique for atmosphere and climate science.

EGOPS5 comprises the following three main capabilities:

- i. Mission analysis and planning for LEO and GNSS signal receivers on LEO satellites.

The antennae specifications of all LEO satellites are variable. Regarding system and orbit specifications, distinct satellite systems — which can be user-defined as well — and ground-station constellations can be selected.

- ii. Simulation of occultation observations.

This includes forward modelling of GNSS/LEO signal propagation through the atmosphere and ionosphere, and simulation of effects of the observing system (position determination errors, instrumental noise, etc.). The results are quasi-realistic observables (i.e. phase delay, amplitude, etc.).

- iii. Processing of simulated or observed occultation data.

This comprises the calculation of atmospheric profiles (real and imaginary refractivity, density, pressure, temperature, water vapour, specific humidity, liquid water) and ionospheric profiles (total electron content, ionospheric refractivity, electron density) from phase delay and amplitude via bending angle and transmission, as well as the compilation of various data product quality statistics.

Additionally, an integrated visualization and validation tool enables post-processing of the retrieved data including the capability of extracting information from the atmosphere system underlying the occultation simulations. This allows the user

to effectively interpret processing results immediately. Moreover, the simulation results (from the first two steps listed above) can be visualized which aids to their comprehension and interpretation.

The different EGOPS5 capabilities mentioned above are structured in an object-oriented manner, because this facilitates further enhancements such as inclusion of alternative calculation options and upgrading of individual components and processes. In particular, items i. and ii. above — which represent the quasi-realistic simulation of radio occultation observables — include the following main components: a *Geometry Simulator* mimicking the occultation system geometry, an *Atmosphere and Ionosphere System Simulator*, a *Transmitter Signal Simulator*, and a *Receiving System Simulator*. These systems are contributing to an overall process, the *Signal Propagation Simulator*, which simulates the propagation of transmitted signals through the atmosphere towards the receivers in low earth orbits. In a similar manner, the occultation data processing part (item iii. above) includes a structured *Inversion Retrieval Toolkit* internally divided into generic processing steps (processes) and data pools (components). An overview of the generic EGOPS5 concept described here is illustrated in Fig. 4.1.

The modular structure of the EGOPS5 software, which is shown in Fig. 4.2, directly derives from the generic EGOPS5 concept. It is composed of a series of high-level modules which are integrated into so-called *systems*. Data-flows connect modules and systems among themselves, thereby representing the natural hierarchy of the physics the software deals with. The core of the modular structure are four systems which are actually performing the end-to-end occultation simulations — these are the *Mission Analysis/Planning System*, the *Forward Modeling System*, the *Observation System Modeling System*, and the *Inversion/Retrieval System*. They depend on a considerable number of input parameters in order to enable realistic simulations and flexible data processing of widely arbitrary GNSS/LEO-LEO occultation missions. A description of these four main systems with emphasis on the LEO-LEO occultation part and the features used for the performance analysis is subject of Section 4.2 below.

To put it briefly, EGOPS5 is a flexible software tool open for continuous improvements and apt to help solve open questions on the GNSS/LEO-LEO based radio occultation technique.

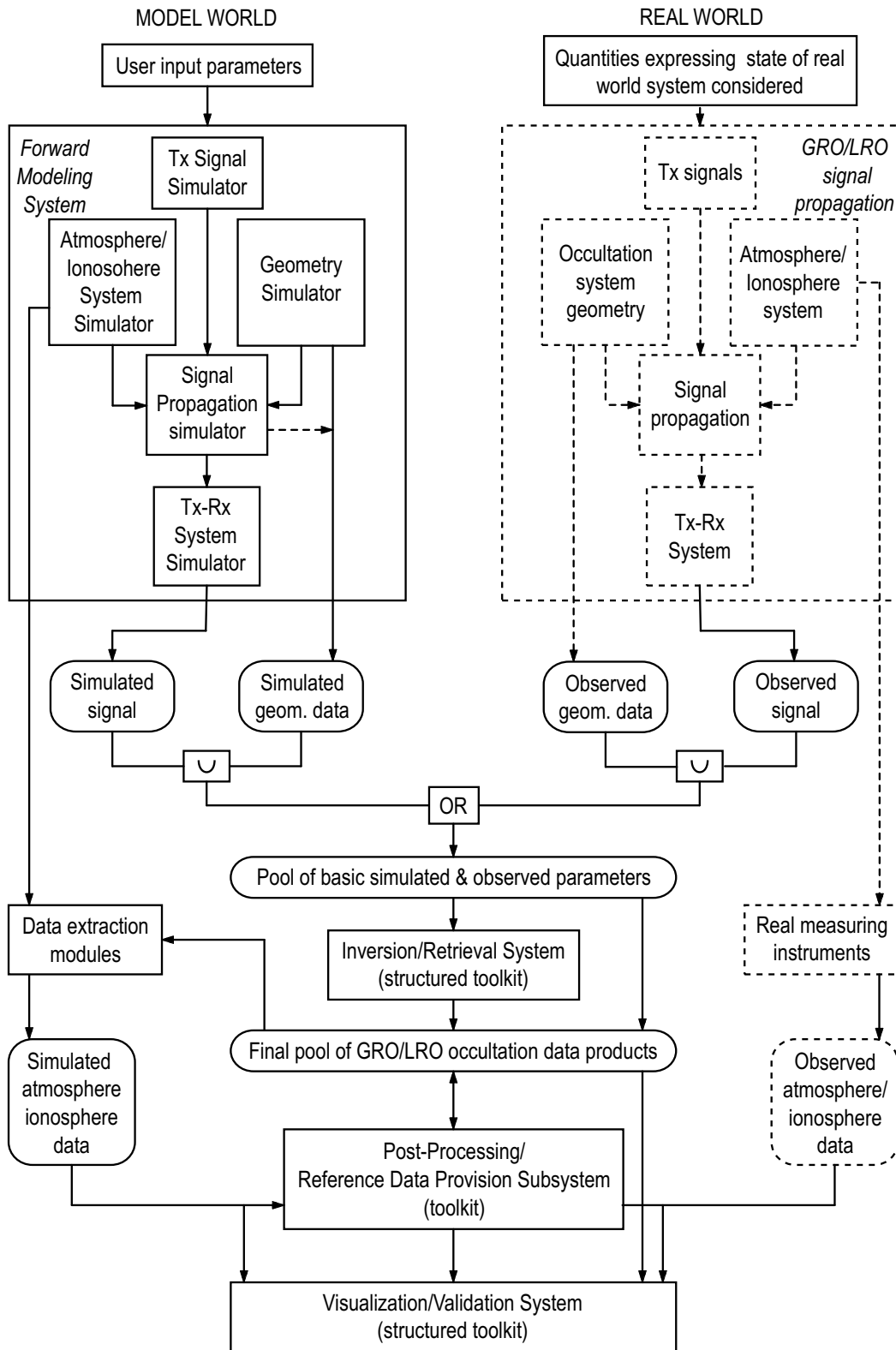


Figure 4.1: Conceptual view of EGOPS5 (after [Kirchengast et al., 2002a]).

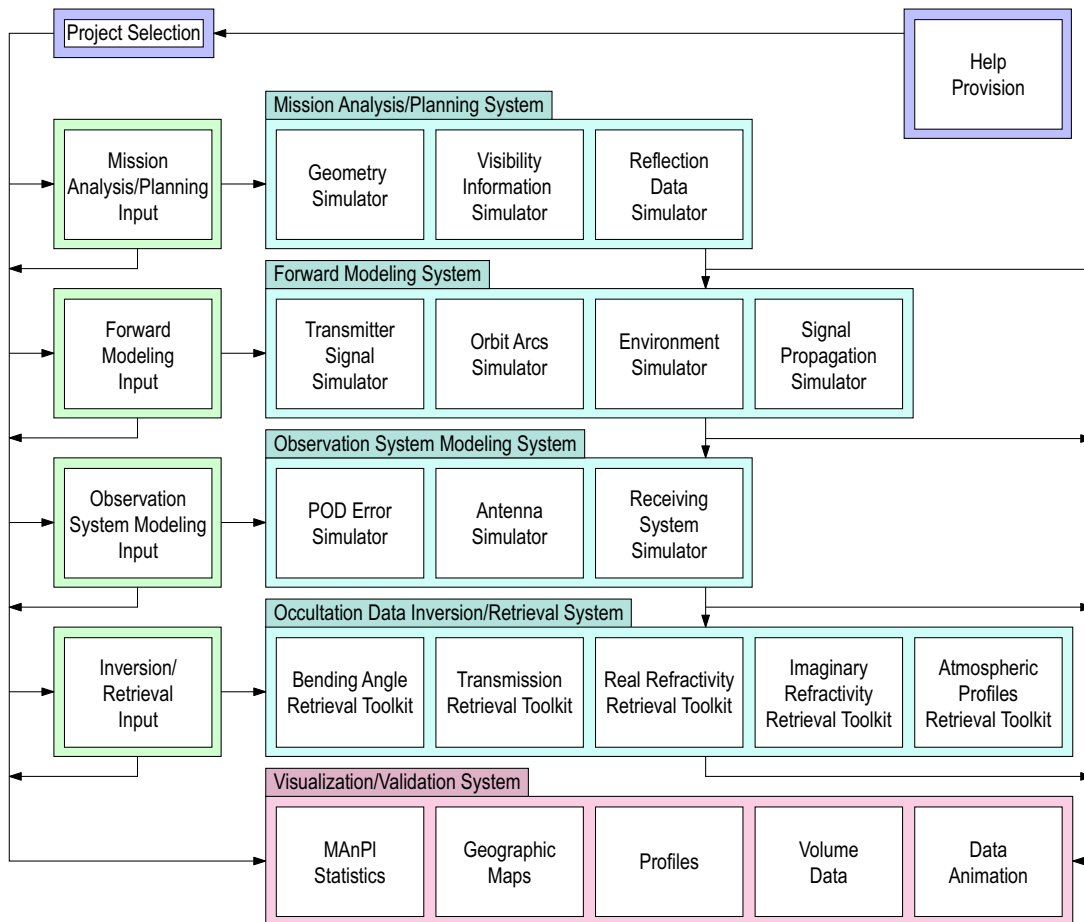


Figure 4.2: Modular view of EGOPS5 (after [Kirchengast et al., 2002a]).

## 4.2 Modelling and Retrieval Structure of EGOPS5

As mentioned in Section 4.1, the modelling and retrieval structure of EGOPS consists of four main parts: Mission Analysis/Planning, Forward Modeling, Observation System Modeling, and Inversion/Retrieval. The former three components are intended for the simulation of radio occultation observations, whereas the latter one is responsible for the processing of simulated as well as observed radio occultation data. In the following, all four systems will be considered with emphasis on the LEO-LEO occultation part, the EGOPS5 novelty which has been used for the performance analysis. For detailed information on the capabilities already included in EGOPS4 refer to [Kirchengast, 1998] and [Kirchengast et al., 2002a].

### 4.2.1 Mission Analysis and Planning

As heritage from EGOPS4, Mission Analysis/Planning (**MAnP1**) comprises analysis and planning of LEO satellite constellations carrying GNSS radio occultation receivers, including antennae field-of-view analysis and planning as well as visibility analysis with regard to ground stations. GNSS radio reflection scenarios can also be simulated, whereby water surfaces (oceans and huge lakes) reflect the GNSS radio signals to the LEO satellites. Analysis and planning of LEO-LEO constellations able to perform LEO-to-LEO radio occultation is a novel capability of EGOPS5.

The **MAnP1** simulation system consists of three main modules (cf. Fig. 4.2): a *Geometry Simulator*, which simulates the geometry of occultation events, a *Visibility Information Simulator*, and a *Reflection Data Simulator*, which simulates the reflection geometry. A sample EGOPS5 **MAnP1** input file is listed in Appendix A.2.

Considering the LEO-LEO occultation part, the baseline LEO-LEO system presently available within EGOPS5 is the ACE+ constellation with two transmitter satellites in an orbit of 800 km and two receiver satellites (counter-rotating to the transmitters) in an orbit of 650 km. The orbits are sun-synchronous with orbit nodes aligned in local time with the planned EPS/METOP orbit nodes. The separation angle between the two satellites in the higher orbit amounts to  $180^\circ$ , that in the lower orbit to  $80^\circ$ . The corresponding orbital elements are listed in Appendix A.1 in the form of *Two Line Element* (TLE) sets. **MAnP1** simulations based on these TLE files showed that with such a constellation, a total of 230 occultation events is obtained during one day and about 7000 events during one month (see Fig. 4.3).

All in all, **MAnP1** is a useful tool to assess, investigate and optimize GNSS/LEO-LEO radio occultation event coverage for planned missions.

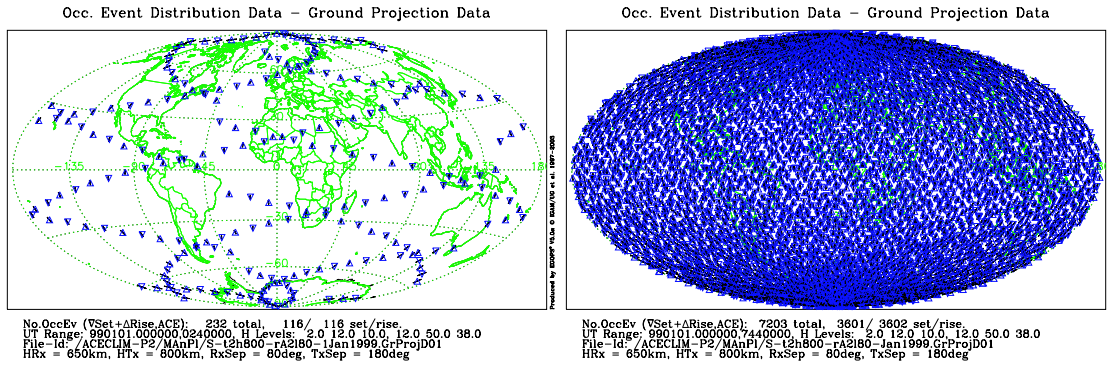


Figure 4.3: Coverage by LEO-LEO occultation events for baseline ACE+ constellation. The left panel shows daily coverage and the right one monthly coverage. Source: [Kirchengast et al., 2004b].

## 4.2.2 Forward Modeling

The EGOPS5 Forward Modeling (FoMod) together with subsequent Observation System Modeling (OSMod, see Subsect. 4.2.3) enables quasi-realistic simulation of GNSS-LEO as well as LEO-LEO radio occultation observables (i.e. phase and amplitude profiles at each signal frequency) and related required variables. FoMod's task is to simulate the transmitter signal propagation through the atmosphere and ionosphere up to the receiver based on orbital motions of transmitter and receiver satellites. The resulting occultation signals contain atmospheric and ionospheric effects only. Effects due to the receiving system, which usually perturb the signal quality, are superimposed during the subsequent OSMod simulation.

The division into FoMod and OSMod during the simulation of the observables has many advantages. For instance, it allows to inspect environmental influences separated from receiving system effects. This enables investigation of both various atmospheric effects and different instrumental effects on the signal properties.

The FoMod simulation system within EGOPS5 consists of four main modules (cf. Fig. 4.2): an *Orbit Arcs Simulator*, which finds the sections of the transmitter (Tx) and receiver (Rx) orbits necessary for performing the forward modelling (ray-by-ray from Tx to Rx over the full occultation event, if using a ray tracer), a *Transmitter Signal Simulator* and a *Signal Propagation Simulator* which involves an additional module, the *Environment Simulator*, which simulates atmosphere and ionosphere. It is worth to note that the environment simulation capabilities have been considerably enhanced during the development of EGOPS5, since clouds (both water and ice) and scintillations due to atmospheric turbulence can now be included, too. A sample EGOPS5 FoMod input file is listed in Appendix A.3.

The orbit arcs simulations are based on geometric properties of a specific occultation event, which can either be taken from the results of a MAnPl task (realistic

geometry) or be defined within the FoMod input file (ideal geometry). The output of orbit arcs computations are so-called simulated geometry data (sgd, stored in a \*.sgd file), which contain the satellite positions and velocities along the orbit arcs of the specified transmitter and receiver satellites at the specified sampling rate for the current occultation event. These data are required as a geometric baseline for subsequent signal propagation simulations. As a convenient sideline, true tangent point profile estimates from ray-tracers are also stored within the sgd files.

The simulation of the transmitter signals, which are the starting point for succeeding signal propagation simulations, provides carrier-frequencies and transmitted powers of the occultation signals. Within the scope of the EGOPS5 development, this component was extended to include LEO-LEO transmitter signal specifications as well. In particular, up to five user-specified frequency channels within the range of 1 to 30 GHz can be exploited. The default settings correspond to the ACE+ system: three nominal frequencies with values of  $F1 = 9.7$  GHz,  $F2 = 17.25$  GHz, and  $F3 = 22.6$  GHz and a transmitter signal power of 3 dBW each. These settings have also been used for the performance analysis.

FoMod's core is the signal propagation simulation, which yields the main observables excess phase and atmospheric loss (defocussing and absorption) for each frequency at the specified sampling rates for the occultation event in consideration. These data, which are saved within so-called simulated signal data (\*.ssd) files, are then used as input for observation system processing. Further results, provided as extended output, are the following "true" parameters (as opposed to the retrieved parameters calculated later on): bending angles, transmissions (influenced by absorption only), Doppler shifts and impact parameters for each signal frequency, as well as the linearly corrected phases LC for frequency F1. Signal propagation simulations within EGOPS5 can be carried out using different ray tracing modules: A full-3D ray tracer which fully accounts for the three-dimensional refractivity field and its first two derivatives, a quasi 3D ray tracer which, besides the refractivity field, only accounts for vertical refractivity gradients and curvature, or a wave optics propagator accounting for multiple phase screens in the atmosphere. In the studies during the preparation of this work, full-3D ray tracing with sub-millimetric accuracy and a sampling rate of 10 Hz has been used and will therefore be described now.

The geometric optics based full-3D signal propagation simulator computes phase delay and atmospheric loss as main products. Rigorous modelling of atmospheric loss is a new feature introduced in EGOPS5 since it is one of the main observables of the LEO-LEO radio occultation. Generally, atmospheric loss consists of two parts: atmospheric loss due to defocussing and due to absorption. These two components are treated separately during the computation: First, for each sample in an occultation, the ray path that goes from a specified transmitter position to a specified receiver position is found via precision ray tracing. The tracking of the receiver is performed by a few trials of ray paths using Newton-Raphson's method of finding roots (see, e.g., [Rodgers, 2000], [Gershenfeld, 2002]). After calculating initial

ray parameters and total phase, the ray path is calculated by solving Haselgrove's three-dimensional differential equations (six equations), and the relative flux density is measured by solving twelve additional equations [Syndergaard, 1998]. These eighteen equations in total are solved by numerical integration using a Runge-Kutta and a predictor corrector method (see, e.g., [Gershenfeld, 2002]) especially designed to deal with adaptive stepsize. The ray-tracer was mainly developed by S. Syndergaard at DMI Copenhagen (now at UCAR, Boulder Colorado, USA). During the integration, the defocussing loss of the signal power is computed in addition to the ray path calculation. After the refracted ray path is precisely known, computation of absorption loss along the ray path is done using the Bouguer-Lambert-Beer law (neglecting emission owing to the strong source intensity in active limb sounding, and scattering thanks to the long wavelengths):

$$I = I_0 \cdot e^{-\int_{l_0}^{l_1} \kappa(l) dl} = I_0 \cdot e^{-\tau} \quad (4.1)$$

Here,  $I$  is the received signal intensity,  $l$  is the coordinate along the ray path and  $l_0$  is the point of the considered part of the ray path farthest away from the sensor, which is usually placed above the absorptive part of atmosphere at a height of about 80 km.  $l_1$  is the point of the ray path closest to the sensor (also at  $\sim 80$  km),  $I_0$  is the un-attenuated intensity at  $l_0$ , and  $\tau$  is the optical thickness.  $\kappa$ , which is proportional to the imaginary refractivity, is the absorption coefficient along the ray path. With this equation,  $\kappa$  is calculated point-by-point along each ray for the given atmospheric conditions using the MPM93 imaginary refractivity model based on a selected atmosphere model (such as the CIRA86aQ\_UoG model, [Kirchengast et al., 1999]) supplying atmospheric parameters like temperature, water vapour, and clouds. Then, using Simpson's integration rule,  $\tau$  and absorption loss ( $I_0/I$ ) are calculated at the receiver end of the signal path and added to the defocussing loss. Finally, if desired, perturbations can be superimposed onto the total atmospheric loss by application of the atmospheric turbulence/scintillation model of [Kuhn, 2003].

All in all, FoMod is a powerful instrument to assess and investigate the capabilities of GNSS/LEO-LEO radio occultation.

In conclusion, two figures representative for FoMod will be shown. Figure 4.4 shows a range of temperature and humidity conditions of the moist air climatological model CIRA86aQ\_UoG which can be used as the underlying atmosphere entering the FoMod simulations. The presented profiles show exactly the conditions which have also been used for a part of the sets belonging to the performance analysis (Sect. 5.1).

Figure 4.5 illustrates total atmospheric loss under different conditions for the CIRA86aQ\_UoG mid-latitude summer (July, 40°N) case. In particular, the following atmospheric conditions are shown: moist but clear air, moist air with altostratus clouds superimposed, and moist air with scintillations due to atmospheric turbulence superimposed. This picture aims at giving a feeling of the atmospheric

loss levels for the three ACE+ frequencies. In general, atmospheric losses show fairly high variations, depending on atmospheric conditions.

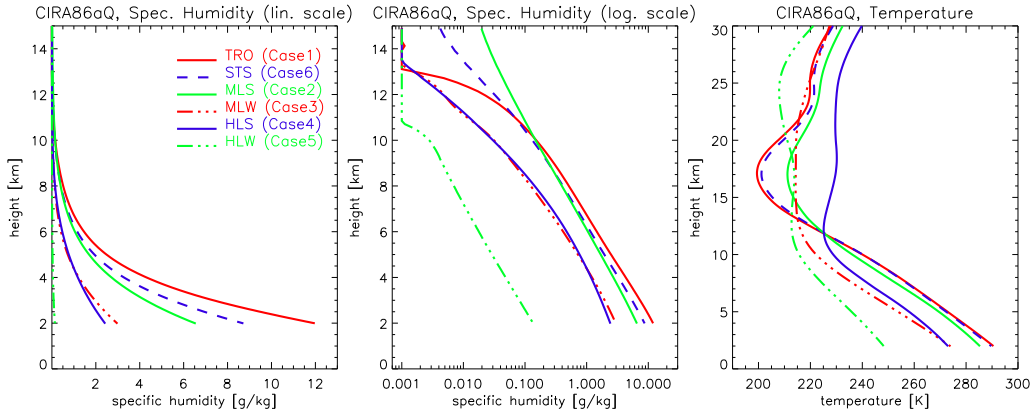


Figure 4.4: Humidity and temperature profiles for six representative atmospheric Cases (cf. Sect. 4.3) of the CIRA86aQ\_UoG model: tropical (TRO, July 0 °N), subtropical summer STS, July 20 °N), mid-latitude summer (MLS, July 40 °N), mid-latitude winter (MLW, January 40 °N), high-latitude summer (HLS, July 70 °N), high-latitude winter (HLW, January 70 °N).

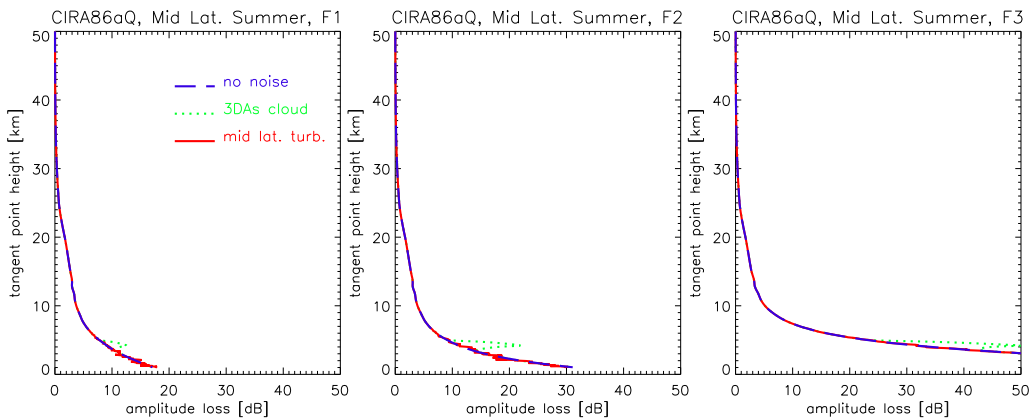


Figure 4.5: Atmospheric loss at the three ACE+ frequencies for the mid-latitude summer case (blue dashed profiles), also with some exemplary altostratus (As) clouds (green dotted profiles) as well as some scintillation activity (red solid profiles) superimposed. The cloud parameters were liquid water content  $0.2 \text{ g m}^{-3}$ , cloud center height 4.5 km, cloud thickness 0.6 km, and cloud horizontal extend 200 km. The atmospheric turbulence/scintillation model parameters were  $C_n^2 = 1.3 \cdot 10^{-15} \text{ m}^{-2/3}$  at surface with an exponential decrease according to a 2 km scale height, and a 200 km horizontal extend of turbulence activity.

### 4.2.3 Observation System Modeling

The EGOPS5 Observation System Modeling (**OSMod**) together with the preceding Forward Modeling (**FoMod**, see Subsect. 4.2.2) enables calculation of GNSS-LEO as well as LEO-LEO radio occultation observables (phase and amplitude profiles at each signal frequency) and related required variables through quasi-realistic simulation. Thereby, the task of **OSMod** is to superimpose all sorts of relevant physical and technical influences of the observation system (antenna, receiver, platform, fiducial sites) on the **FoMod** data output. In particular, this has an impact on **FoMod**'s “ideal” orbit data (spacecraft positions and velocities) and “ideal” signal data (phases and amplitudes) arriving at the receiving antenna, which up to this point were influenced by the atmosphere only.

The **OSMod** simulation system consists of three main modules (cf. Fig. 4.2): A *POD Error Simulator* which provides modelling for Precise Orbit Determination (POD) errors that naturally occur when determining the orbit positions and velocities of GNSS/LEO satellites, an *Antenna Simulator* which simulates Tx and Rx antenna patterns, and a *Receiving System Simulator* which includes modelling of receiver performance, local multipath, and differencing treatment (clocks modelling). A sample EGOPS5 **OSMod** input file is listed in Appendix A.4.

Compared to EGOPS4, the capabilities of the receiving system simulation have been enhanced. In particular, modelling of instrumental errors has been improved. Now, rigorous modelling of thermal amplitude noise,  $1/f$  amplitude noise as well as different amplitude drifts (polynomial and sinusoidal) is possible. In this context, also a realistic link-budget is derived which is needed in order to have a reasonable carrier-to-noise density ratio ( $C/N_0$ ) input to the noise modelling. This link-budget results automatically from the end-to-end simulation of all link budget components — from transmitter power via transmission antenna gain, space loss, and receiver antenna gain to received amplitude.

All in all, **OSMod** is a powerful tool which allows to assess and investigate the influence of instrumental errors on the data quality and thus is useful for assessing and optimizing the instruments applied for planned missions.

To conclude, carrier-to-noise density ratio profiles (Fig. 4.6) as well as figures illustrating the characteristics of different instrumental error sources (Figs. 4.7–4.10) are shown below. The pictures are derived from a simulation with the same **OSMod** settings that have also been used for the performance analysis.

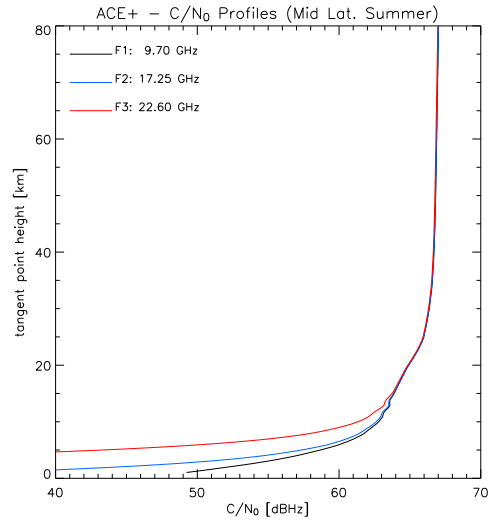


Figure 4.6: Carrier-to-noise density ratio ( $C/N_0$ ) profiles for the three ACE+ frequencies for the mid-latitude summer case. The underlying settings were transmitter power 3 dBW, Tx and Rx antenna gain  $\sim 25$ –28 dB, and instrumental error settings as shown in Figures 4.7–4.10. Slight  $C/N_0$  adjustments by OSMOD then ensured a nominal  $C/N_0 = 67$  dBHz above the atmosphere.

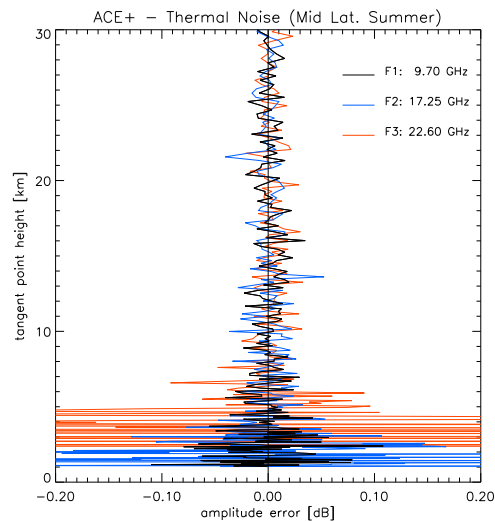


Figure 4.7: Exemplary realizations of thermal amplitude noise profiles for the three ACE+ frequencies for the mid-latitude summer case. The downward increase of thermal noise with the gradual  $C/N_0$  decrease (Fig. 4.6) is well visible. The main thermal noise model settings were 80 K antenna noise temperature and 160 K receiver noise temperature.

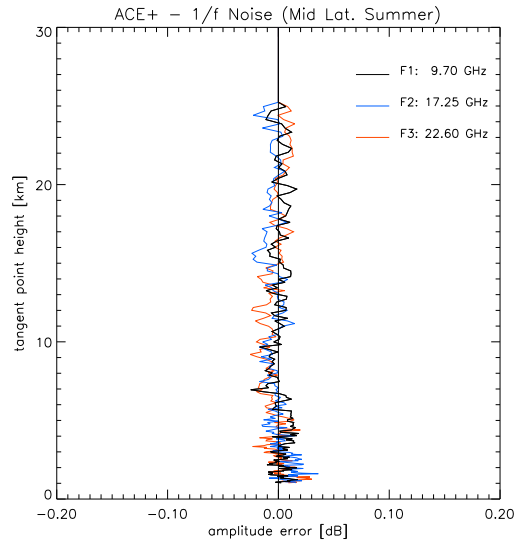


Figure 4.8: Exemplary realizations of  $1/f$  noise profiles for the three ACE+ frequencies for the mid-latitude summer case. A flicker noise model was used for modelling the  $1/f$  noise, with a frequency range from  $1/30$  Hz to 5 Hz and a gain fluctuation of  $3 \cdot 10^{-4} \text{ Hz}^{-1/2}$  at 1 Hz (model supplied by ESTEC; more information p. 79).

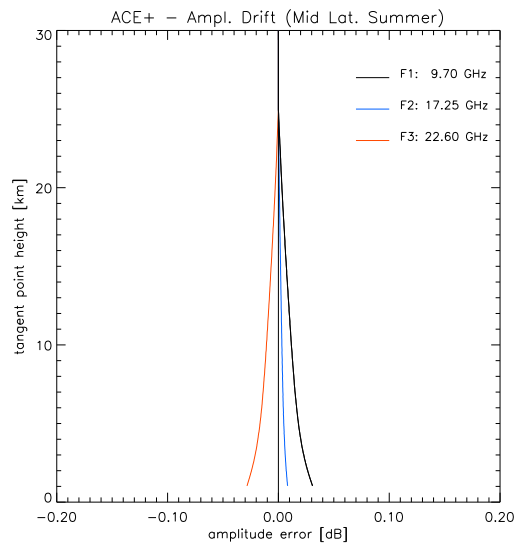


Figure 4.9: Exemplary realizations of linear amplitude drift profiles for the three ACE+ frequencies for the mid-latitude summer case. The main amplitude drift model setting was a linear drift slope of  $0.060 \text{ dB min}^{-1}$ , with the drift starting at the occultation event time corresponding to a tangent point height of 25 km.

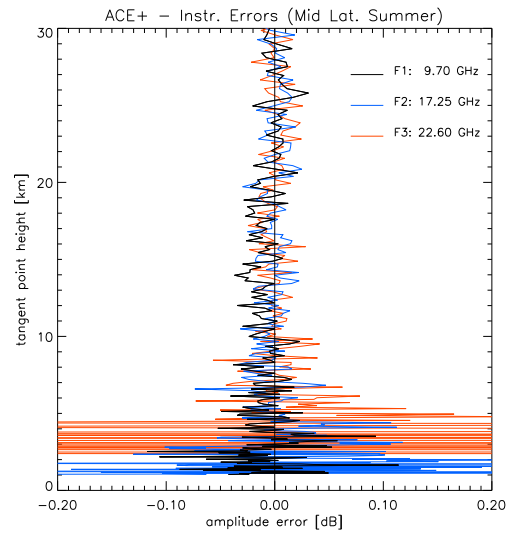


Figure 4.10: Exemplary realizations of total instrumental error profiles for the three ACE+ frequencies for the mid-latitude summer case. All three error sources illustrated in Figs. 4.7–4.9 are included with model settings as noted in the corresponding captions.

#### 4.2.4 Inversion/Retrieval

Just like in EGOPS4, Inversion/Retrieval (**InRet**) performs the processing of simulated or observed GNSS-LEO phase and amplitude data (supplemented by the necessary geometry information) via Doppler shifts and bending angles down to quasi-vertical profiles of real refractivity, density, pressure, temperature, and — using a priori information — humidity. Additionally, ionospheric profiles of total electron content and electron density can be retrieved. The new feature of EGOPS5 is that it allows for LEO-LEO occultation data processing as well, which in addition to phases exploits amplitudes, too. This enables — without additional information — retrieval of quasi-vertical profiles of real and imaginary refractivities, density, pressure (or geopotential height), temperature, humidity, as well as liquid water content if needed, via bending angles and transmissions from phase and amplitude data. An overview of the scientific retrieval algorithms for both GNSS-LEO and LEO-LEO data processing is given in [Kirchengast et al., 2004a] (see references therein for further literature on this subject).

The **InRet** simulation system within EGOPS5 consists of five main modules (cf. Fig. 4.2): an *Ionospheric Correction and Bending Angle Retrieval Toolkit*, a *Transmission Retrieval Toolkit*, a *Real Refractivity Profiles Retrieval Toolkit*, an *Imaginary Refractivity Profiles Retrieval Toolkit* and an *Atmospheric Profiles Retrieval Toolkit*. A sample EGOPS5 **InRet** input file is listed in Appendix A.5.

Now we will have a closer look at the new LEO-LEO occultation data processing

within EGOPS5, of which a schematic overview is shown in Figure 4.11. For a detailed algorithmic description consult [Nielsen et al., 2003] and [Kirchengast et al., 2004b]. The basics of the LEO-LEO profiles retrieval have already been treated within Section 2.2.

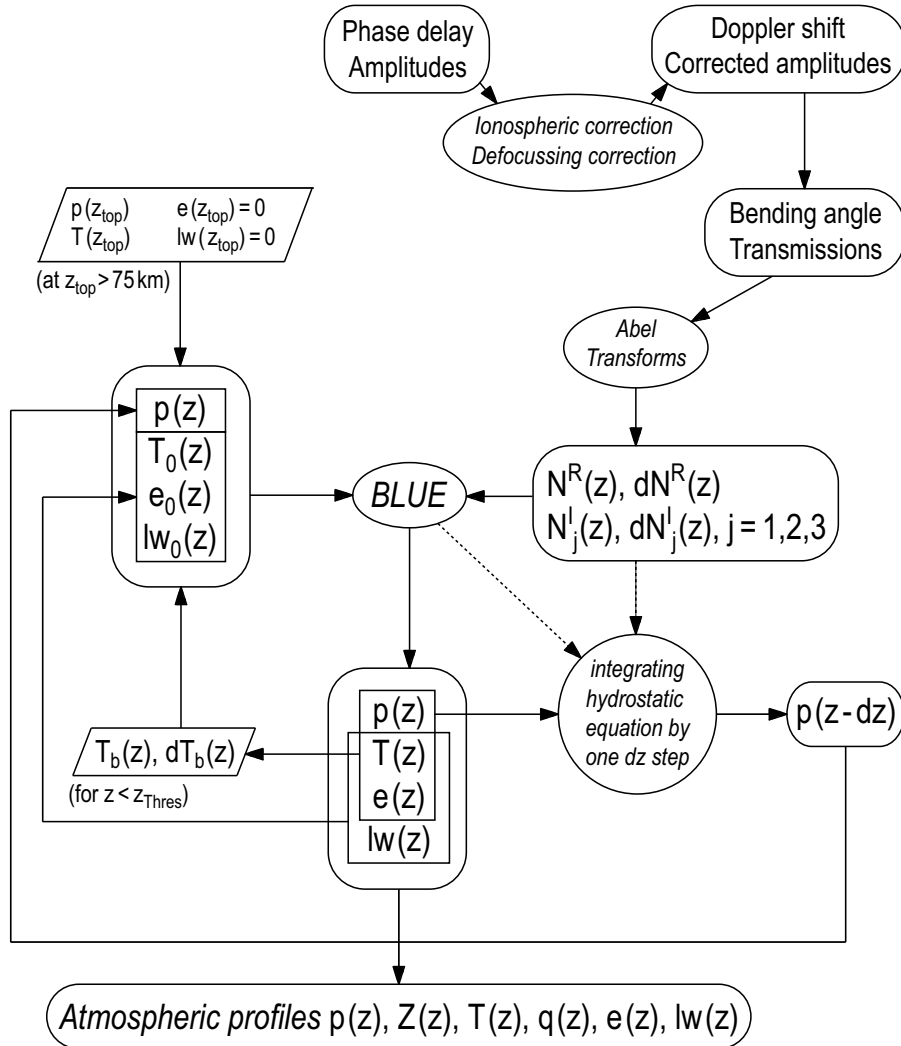


Figure 4.11: Schematic view of the LEO-LEO occultation data processing with emphasis on the atmospheric profiles retrieval (after [Kirchengast et al., 2004a]).

The general LEO-LEO processing strategy within EGOPS5 makes use of all main modules mentioned above and consists of five main steps: bending angle retrieval, transmissions retrieval, real refractivity retrieval, imaginary refractivities retrieval, and atmospheric profiles retrieval. The working structure of these components and basic relations to each other will be considered below.

## Bending Angle Retrieval

Within this first step, the atmospheric bending angle profile is computed as a function of the impact parameter, starting from phase and bending angle as well as POD (position and velocity vectors of Tx and Rx satellites) data obtained either from OSMOD simulations or real observations. This computation can be done applying geometric-optics or wave-optics processing. Whereas the former uses phase path changes only, the latter exploits normalized amplitude profiles, too.

The geometric-optics processing comprises five steps. First, the simulated or measured phase delays are smoothed over  $\sim 1$  sec (corresponds to  $\sim 2$  km in height, and less below 30 km) at a user specified sampling rate of 10Hz ( $\sim 0.2$  km in height) or higher. This avoids amplification of high frequency noise. Within EGOPS5, a regularization smoother following [Syndergaard, 1999] is applied (see also [Kirchengast et al., 2004b]). Furthermore, in order to remove unphysical data values, a outlier rejection algorithm which responds to data samples deviating by more than 3 times the standard deviation from the mean over a neighborhood of  $\pm 0.5$  sec can be activated if required.

Second, in order to remove ionospheric phase delay from the measured total phase delay, a dual-frequency linear combination (cf. Eq. 2.2) is applied on phases. ACE+ data processing currently uses frequencies F1 and F2. Since for the ACE+ X/K-band frequencies the ionospheric effects are approximately two orders of magnitude smaller than for the GNSS L-band frequencies, this phase correction is sufficient. More sophisticated correction schemes such as the correction of bending angles [Vorob'ev and Krasnil'nikova, 1994] are only required in the case of GNSS signals.

Third, Doppler shift is derived from the corrected phases via differentiation of phase delay (cf. Eq. 2.3). This differentiation is implemented as a space-centered finite difference, which means that the Doppler shift of each sample is set to the difference estimate between the neighbouring samples above and below. This simple scheme is possible since the smoothing during the first step ensures smoothness of the data over a neighborhood of three data samples [Kirchengast et al., 2004b].

Fourth, impact parameter and bending angle are derived from Doppler shift and orbital positions and velocities of the satellites by iteratively solving Eqs. 2.5–2.8. The iterative solution is needed since the impact parameter is only implicitly contained. The computations are based either on the assumption of a spherical symmetric earth (radius of 6371 km) or on a realistic ellipsoidal earth shape (WGS-84 ellipsoid, see, e.g., [Landolt-Börnstein, 1984]). In the latter case, the so called oblateness correction has to be applied before computation, where the POD data are transformed to originate in the ellipsoid's center of local curvature in the occultation plane at the mean geographic location of the occultation event (described by [Syndergaard, 1998]). A by-product of this correction is the knowledge of the mean tangent point location of the event and of its radius of local curvature (more details in [Kirchengast et al., 2004b]).

Fifth and finally, the measured bending angle profile is statistically optimized between altitudes of 30 km and 120 km in order to ensure adequate quality of the bending angle profile for subsequent Abel transform to refractivity. This is an important step in order to avoid large error propagation from mesospheric altitudes into the retrieval domain of interest (0–50 km). The optimization is done in an inverse-covariance-weighted least-squares way using the background bending angle profile which best fits the retrieved profile within the Stratopause region (baseline: 45–65 km) selected from a set of bending angle profiles of the global MSIS90 (see, e.g., [Hedin, 1991]) or CIRA86aQ\_UoG climatology. For detailed information refer to [Kirchengast et al., 2004b].

Summing up, the bending angle retrieval within EGOPS5 yields the mean tangent point location of the occultation event, its radius of local curvature, as well as the optimized bending angle profile ready for the refractivity retrieval.

### Transmissions Retrieval

This step yields transmission profiles for each LEO-LEO signal frequency which are influenced by atmospheric absorption only. They are derived from the amplitude profiles using the impact parameter profile, which is known from the bending angle retrieval, and the transmitter and receiver position profiles. In order to achieve this, two steps must be carried out: a defocussing and spreading correction followed by an amplitude normalization, which is the reason for the intrinsic self-calibration of the amplitudes.

The defocussing and spreading correction is needed, because the measured amplitudes are not only weakened due to the desired absorption, but also due to differential bending and spherical signal spreading. The correction method depends on the processing approach being used (wave-optics or geometric optics). Within the EGOPS5 geometric optics processing, a defocussing and spreading model amplitude  $A_{\text{dsm}}$  is computed from the satellite opening angle, the impact parameter profile, and the radial distances of the Tx and Rx satellites (cf. Eq. 2.12).

Within the second step, this defocussing and spreading model amplitude is used as correction in order to convert the observed amplitudes to the desired transmissions. In particular,  $A_{\text{dsm}}$  is normalized to a reference height above the absorptive atmosphere, where the transmission is about unity ( $\sim 25$  km in the case of ACE+). Afterwards, the observed amplitudes are divided by this normalized defocussing and spreading model amplitude. Now, the resulting amplitudes are normalized and corrected for defocussing and spreading and thus are ready for the conversion into transmission (cf. Eqs. 2.13 and 2.14).

It is worth mentioning that in EGOPS5 processing, the impact parameter profile (used in step 1), the  $A_{\text{dsm}}$  profile as well as the amplitude profiles are smoothed before their usage applying a third order polynomial filter with a filtering width

of  $\sim 1$  km. The resulting transmission profiles are smoothed, too. These filtering steps avoid unnecessary amplification of high-frequency noise in the subsequent Abel transform to imaginary refractivity.

### Real Refractivity Retrieval

The real refractivity profile as a function of height is obtained from the bending angle profile as a function of impact parameter via the classical Abel transform (cf. Eq. 2.19). Within EGOPS5 processing, the theoretically infinite top value of the Abel integral is set to a value corresponding to a height of 120 km, exploiting the bending angle profile over the full range and ensuring accurate retrieval up to the stratopause [Steiner et al., 1999].

### Imaginary Refractivities Retrieval

The imaginary refractivity profiles (one for each frequency) as a function of height are derived from the transmission profiles, the refractive index profile and the impact parameter profile via another Abel transform (cf. Eq. 2.23) akin to the classical one used within the real refractivity retrieval. Within EGOPS5, the theoretically infinite top value of the Abel integral is set to a value corresponding to a height above which the logarithm of the transmission and thus its integral contribution equals zero (near the reference height of  $\sim 25$  km above which absorption essentially vanishes).

After the imaginary refractivity profiles are known at each frequency, they are also filtered with a third order polynomial filter with a filtering width of  $\sim 1$  km. This avoids possible high-frequency noise, incurred by application of the Abel transform, to be transferred to further exploitation of the imaginary refractivity profiles.

### Atmospheric Profiles Retrieval

Since real and imaginary refractivities are connected to pressure, temperature, humidity, liquid water, and ice water, these parameters can be derived if the refractivities are known. In particular, the relating equations used within EGOPS5 are the simple Smith-Weintraub formula (cf. Eq. 2.26) for the real refractivity and a Millimeter-wave Propagation Model (MPM93, see, e.g., [Liebe et al., 1993]) (cf. Eq. 2.27) for the imaginary refractivities. Generally, it depends on the atmospheric state which profiles have to be retrieved. Therefore, different retrieval modes are available within EGOPS5: a *dry air retrieval* which only returns the dry air parameters density, pressure, and temperature, a *moist air retrieval* which computes humidity, too, and a *cloudy air retrieval* which additionally yields the liquid water density. The retrieval mode to be used is declared within the `InRet` input file. In the following, the general procedure to derive atmospheric profiles will be described.

Based on the three ACE+ frequencies, real and imaginary refractivity profiles feed four equations: one equation from the real refractivity, which is non-dispersive for the frequencies under consideration, and three equations from the frequency dependent imaginary refractivity. Thus, together with the hydrostatic equation (cf. Eq. 2.28, related equations are Eqs. 2.29–2.31), a set of five equations is available to derive the four desired parameters pressure, temperature, humidity, and liquid water. Since these equations contain five elements of independent information, the problem is slightly over-determined.

The estimation of the geophysical parameters is done in an “onion peeling” approach by downward (in height) integration of the hydrostatic equation, to sequentially obtain pressure, combined with an iterative Best Linear Unbiased Estimation (BLUE) solution at each integration step to obtain temperature, water vapour and liquid water from pressure and real and imaginary refractivities. The BLUE algorithm looks like this (after [Kirchengast et al., 2004a]):

$$\mathbf{x}_{n+1} = \mathbf{x}_n + \left( \mathbf{K}_n^T \cdot \mathbf{C}_y^{-1} \cdot \mathbf{K}_n \right)^{-1} \left[ \mathbf{K}_n^T \mathbf{C}_y^{-1} \left( \mathbf{y} - \mathbf{y}^{\text{mod}}(\mathbf{x}_n) \right) \right]. \quad (4.2)$$

$\mathbf{x}_n$  is the state vector to be iteratively estimated,  $\mathbf{y}_n$  is the measurement vector (real and imaginary refractivities),  $\mathbf{y}_n^{\text{mod}}$  is the forward-modelled measurement vector,  $\mathbf{C}_y$  is the measurement (and forward modelling) error covariance matrix, and  $\mathbf{K}_n$  is the Jacobian weighting matrix. The BLUE algorithm requires the specification of covariance matrices for the refractivity data, which are formulated based on the knowledge of their respective error characteristics. A detailed explanation of the BLUE solution within EGOPS5 is given within [Kirchengast et al., 2004b].

The EGOPS5 downward integration of the hydrostatic equation uses a fourth order Runge-Kutta integration with small integration steps of 100 m. This ensures accurate pressure values at each integration step. The integration is initialized at a height of 75 km assuming an initial atmospheric state ( $p_{\text{top}}, T_{\text{top}}, e_{\text{top}} = lw_{\text{top}} = 0$ ), where initial temperature and pressure values are estimated from the local scale height, which is estimated from the imaginary refractivity near 75 km and the local equation of state. Deviations from the true atmospheric state are not critical since initialization errors decay quickly over the first few scale heights, already within the mesosphere. The BLUE algorithm is involved after each integration step and estimates the state ( $T_i, e_i, lw_i$ ) at the height  $z_i$  from the pressure already obtained at the same height and the atmospheric state ( $T_{i+1}, e_{i+1}, lw_{i+1}$ ) at the previous height  $z_{i+1}$ .

In practice, the state parameters being retrieved within EGOPS5 depend on the height range. In particular, the water vapour effect is negligible above 20 km, which is why only temperature is estimated there. Furthermore, between 8 and 20 km, only temperature and water vapour are estimated, because liquid water effects are negligible in this height range. Below, the full state (p, T, e) is estimated, which requires at least three independent pieces of information. In this connection

it should be mentioned that ice water does not need to be retrieved, since the retrieval is insensitive to ice clouds (see, e.g., [Gradinarsky et al., 2003]).

On account of the slight over-determination of the problem, it is still possible to retrieve the full atmospheric state if one of the imaginary refractivities is lost. This happens when only two frequencies provide data in a useful dynamic range. Even if two imaginary refractivities are lost, which can occur in very wet regions, estimation of pressure, temperature and water vapour is possible if liquid water is negligible or some information (e.g. temperature) is known from background data. In extreme situations, it can happen that the lowest ACE+ frequency is lost, too. In this case, which only occurs rarely within the lower troposphere, profile retrieval below the affected regions is impossible.

Finally, a specific feature of the EGOPS5 atmospheric profiles retrieval shall be explained: *advanced processing in the case of severe atmospheric turbulence*. Strong scintillations which can occur below  $\sim 3\text{--}6$  km degrade the retrieval described above, because they cause large variations of the imaginary refractivity data. This weakness can be evaded, since the parts of the signal affected by scintillation can be identified thanks to the high sampling rate (1 kHz) of the raw measurements. Thus, a threshold height  $z_{\text{thresh}}$  below which severe turbulence is present can be determined, wherefore imaginary refractivity data belonging to this height range should be used with caution and be supplied with low to negligible weight within the BLUE algorithm. The under-determination of the BLUE algorithm arising from this down-weighting of the imaginary refractivity is compensated by introduction of weak background (a priori) information into the retrieval at the height levels concerned. In particular, a suitable temperature profile is searched within an adequate database, for example a 24 h ECMWF forecast, since temperature is well predictable in the troposphere. The selected background temperature profile is the one which fits the retrieved temperature profile best in the troposphere right above  $z_{\text{thresh}}$ , where the data are still very accurate and allow for a good fit [Kirchengast et al., 2004a]. Of course, this additional information has to be accounted for within the BLUE algorithm which therefore assumes the following form:

$$\mathbf{x}_{n+1} = \mathbf{x}_n + \left( \mathbf{K}_n^T \cdot \mathbf{C}_y^{-1} \cdot \mathbf{K}_n + \mathbf{C}_b^{-1} \right)^{-1} \left[ \mathbf{K}_n^T \mathbf{C}_y^{-1} \left( \mathbf{y} - \mathbf{y}^{\text{mod}}(\mathbf{x}_n) \right) - \mathbf{C}_b^{-1} \left( \mathbf{x}_n - \mathbf{x}^b \right) \right] \quad (4.3)$$

where  $\mathbf{x}^b$  is the background (a priori) state vector and  $\mathbf{C}_b$  is the background (a priori) error covariance matrix.

This so-called *best-fit temperature extrapolation* approach which has also been applied on a large part of the performance analysis (cf. Subsect. 5.1.2 and Sect. 5.2) was found to ensure accurate humidity and temperature retrieval even under severe turbulence conditions — although it is not yet particularly optimized.

Altogether, **InRet** has the capability to perform high quality processing of LEO-LEO as well as GNSS-LEO occultation data. In order to illustrate the operating mode of the whole retrieval chain, Figures 4.12–4.15 show the sequence of retrieved

parameters from transmissions via refractivities to temperature and humidity for the mid-latitude summer case under three different atmospheric and instrumental error conditions (no noise, total instrumental error, altostratus cloud and mid latitude turbulence combined with total instrumental error). Each figure shows three different panels: the left one presents the profile of the parameter, the middle one shows the absolute retrieval error, and the right one the relative retrieval error.

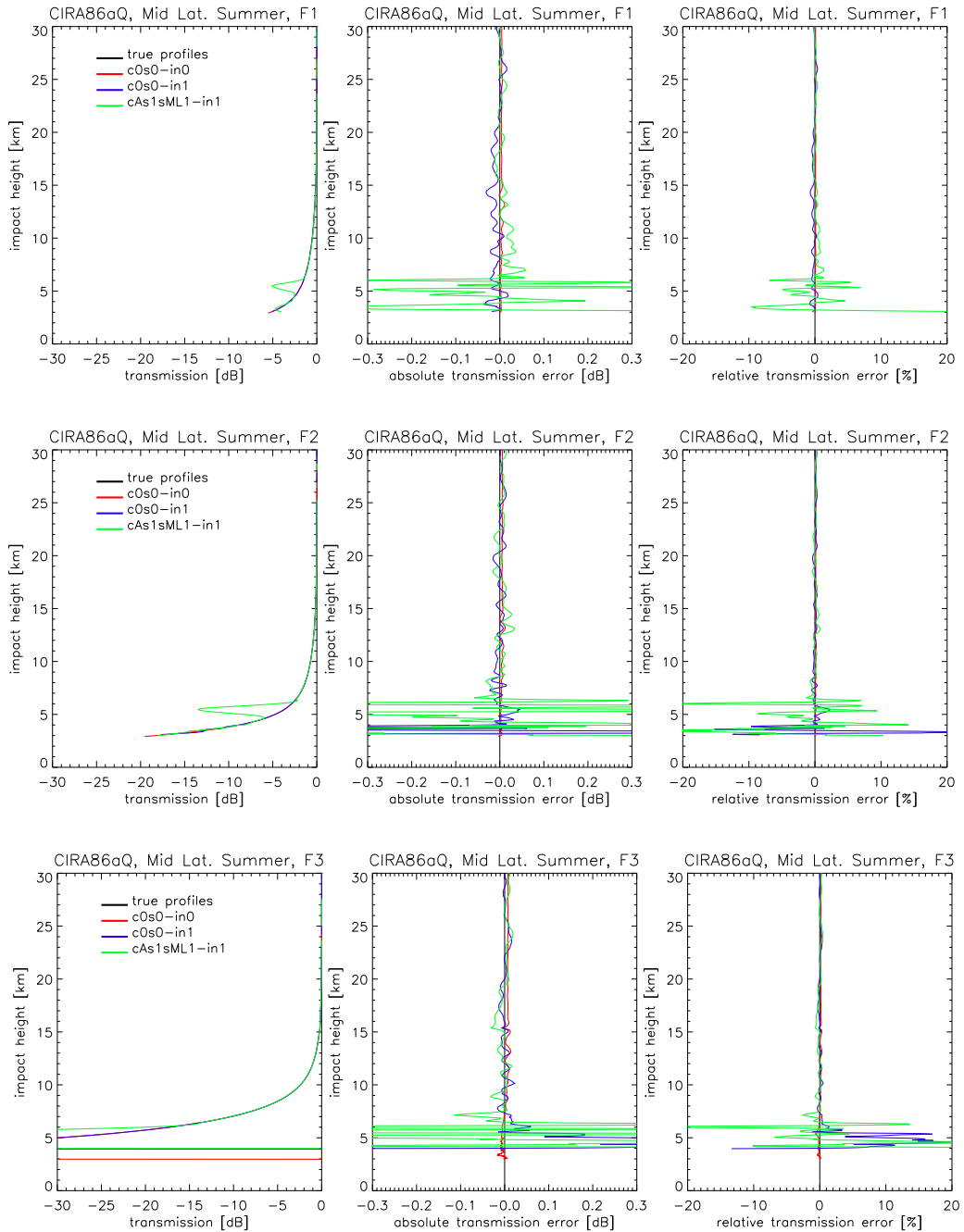


Figure 4.12: Exemplary transmission retrieval results for the three ACE+ frequencies F1 to F3 for the mid-latitude summer case. The red line represents the ideal case without atmospheric disturbances and without instrumental errors (c0s0-in0). The blue line includes all instrumental error sources discussed in Subsect. 4.2.3 (c0s0-in1). The green line involves altostratus clouds and turbulence with the same specifications as shown in Subsect. 4.2.2 in addition to the instrumental errors (cAs1sML1-in1).

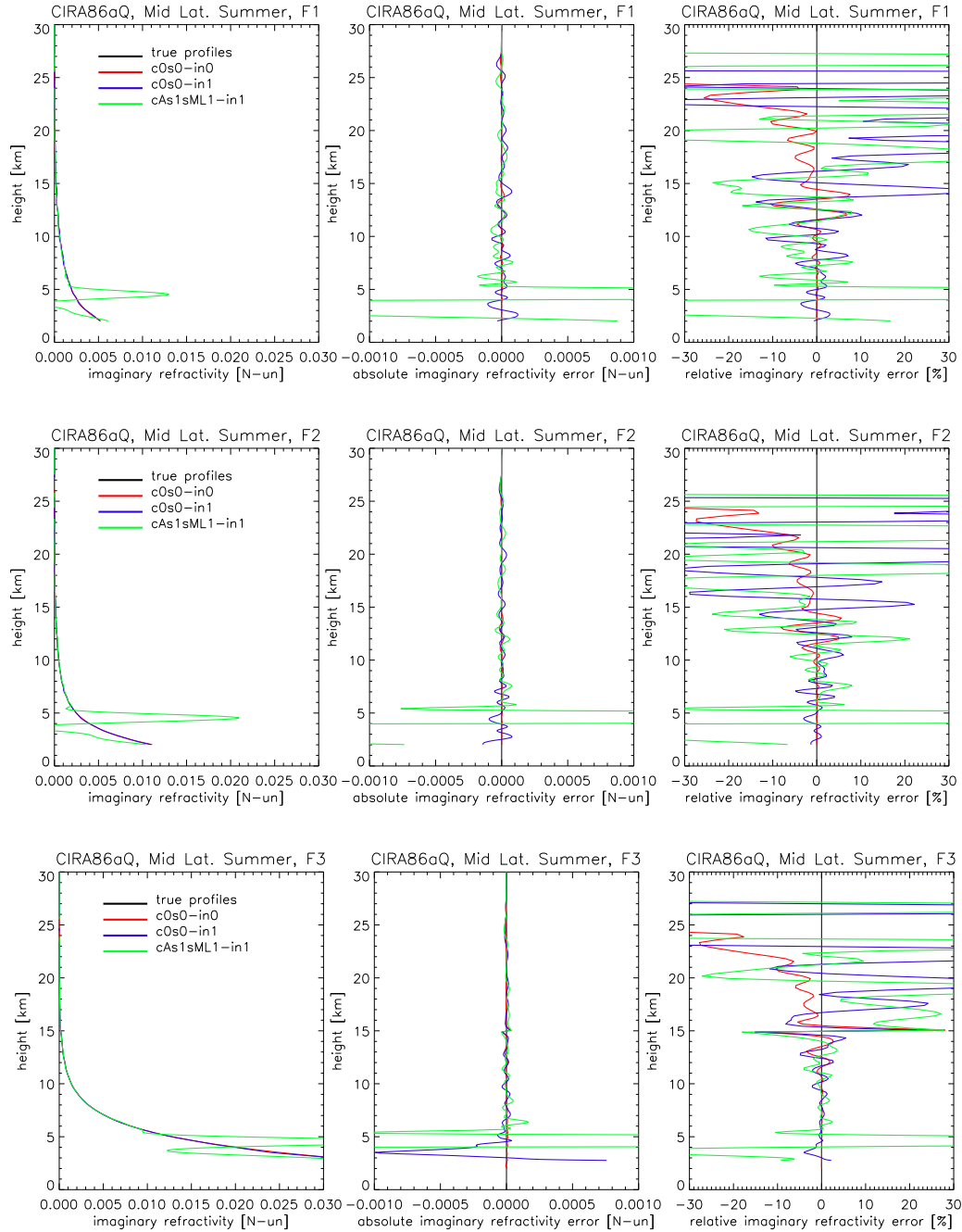


Figure 4.13: Exemplary imaginary refractivity retrieval results for the three ACE+ frequencies F1 to F3 for the mid-latitude summer case. For a specification of the individual profiles, see caption of Fig. 4.12.

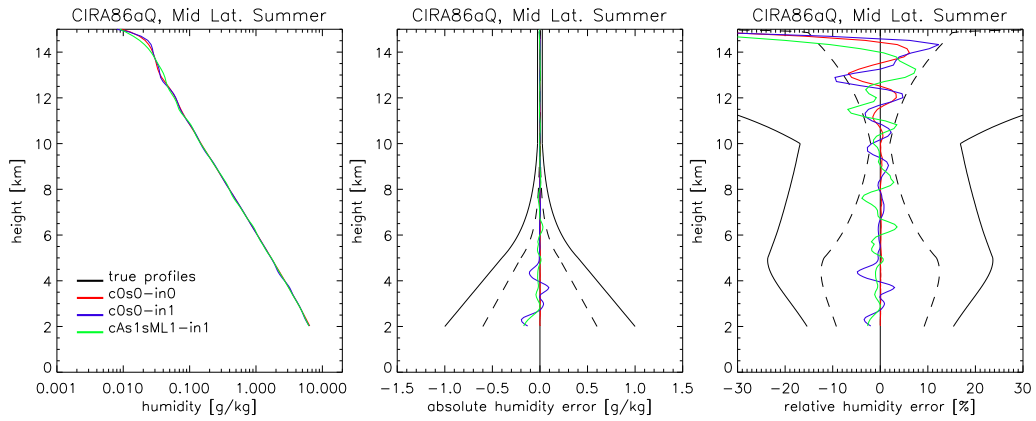


Figure 4.14: Exemplary humidity retrieval results for the mid-latitude summer case. For a specification of the individual profiles, see caption of Fig. 4.12.

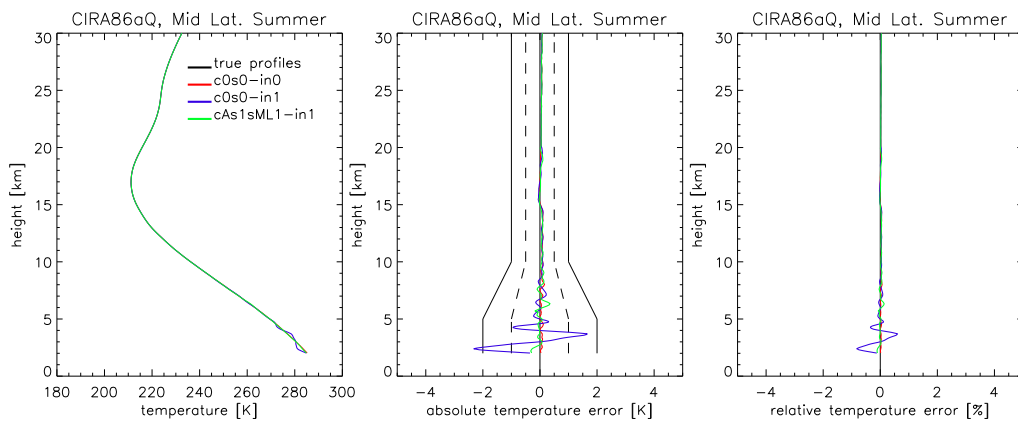


Figure 4.15: Exemplary humidity retrieval results for the mid-latitude summer case. For a specification of the individual profiles, see caption of Fig. 4.12.

### 4.3 Performance Analysis Setup

As outlined at the beginning of this chapter, the aim of the analysis is to assess the performance of temperature and humidity retrieval from ACE+ LEO-LEO occultation data under different atmospheric conditions (clear, cloudy, and turbulent air). For this purpose, 22 different sets consisting of at least 40 occultation events each and based on various atmosphere models and atmospheric states have been generated using EGOPS5. The transmitter and receiver orbits were assumed to be at heights of 800 km and 650 km, respectively (baseline orbit ACEPASS study). After forward modelling including a receiving system error modelling, atmospheric profiles were retrieved from the resulting observables and compared with the original atmospheric data on which the forward modelling was based (“true” profiles). In particular, absolute and relative deviation of the retrieved temperature and humidity profiles from the respective “true” atmospheric profiles were computed. Thereafter, true ( $x^{\text{true}}$ ) and retrieved ( $x^{\text{retr}}$ ) profiles as well as the error profiles of each event within a set were normalized to the same height grid and statistically analyzed; the profiles were averaged and mean bias

$$\bar{b} = \frac{1}{n} \sum_{i=1}^n (x_i^{\text{retr}} - x_i^{\text{true}}), \quad n \dots \text{No. of events}, \quad (4.4)$$

standard deviation

$$s = \sqrt{\frac{1}{n-1} \sum_{i=1}^n (x_i - \bar{b})^2}, \quad (4.5)$$

and bias uncertainty (two times the standard deviation of the bias)

$$2 \cdot s_b = 2 \cdot \frac{s}{\sqrt{n}} \quad (4.6)$$

have been put into graphs (see Figs. in Chapt. 5). The statistical data post-processing described above was done by means of IDL routines which at the same time monitored the data quality eliminating unphysical profiles and correcting unphysical data values. Finally, the results of the sets have been compared among each other, which is discussed in Chapter 5. A schematic overview of the end-to-end simulation work cycle is shown in Fig. 4.16.

Generally, the analysis consists of two main parts: one based on a climatological atmosphere model (CIRA86aQ\_UoG, results in Sect. 5.1) and the other based on an ECMWF high-resolution (T511L60) analysis field (results in Sect. 5.2). A description of the sets prepared for each of those two parts is given below.

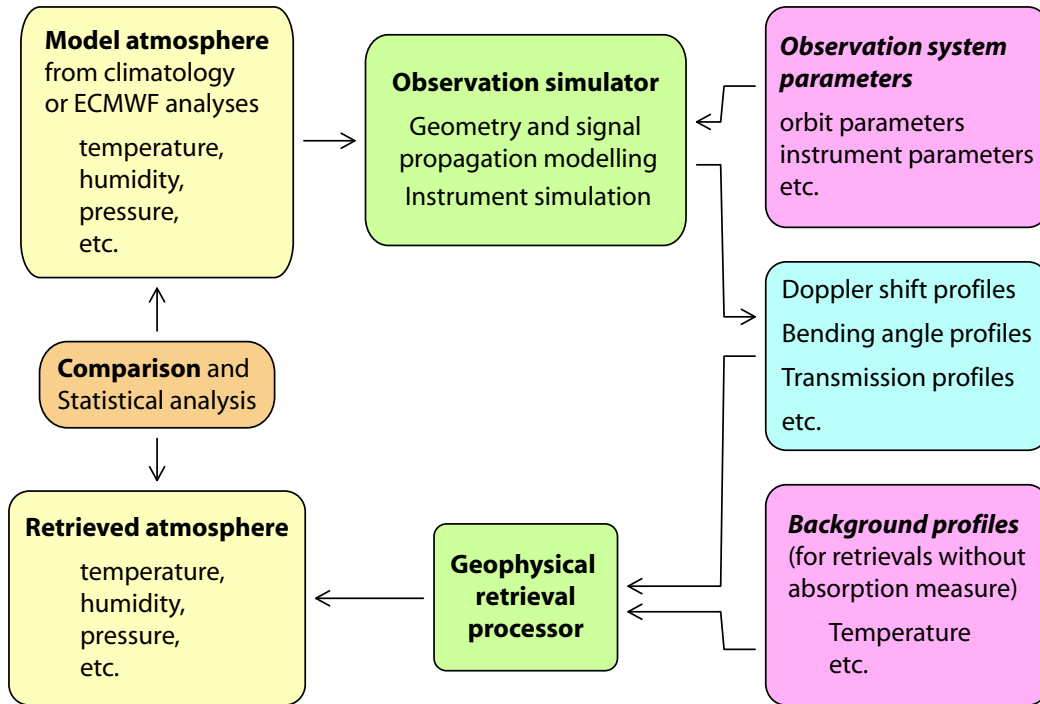


Figure 4.16: Flowchart of the performance analysis steps.

### Climatological Atmosphere Model

For the analysis based on the climatological atmosphere model, six *Cases* were defined which are representative of atmospheric conditions at different climatic latitudes in winter as well as summer (2003 is just an arbitrary year number):

Name	Acronym	Latitude	Date
Tropical (Case1)	TRO	0 °N	July 15, 2003
Subtropical Summer (Case6)	STS	20 °N	July 15, 2003
Mid-Latitude Summer (Case2)	MLS	40 °N	July 15, 2003
Mid-Latitude Winter (Case3)	MLW	40 °N	Jan. 15, 2003
High-Latitude Summer (Case4)	HLS	70 °N	July 15, 2003
High-Latitude Winter (Case5)	HLW	70 °N	Jan. 15, 2003

The “uneven” insertion of Case 6 between Case 1 and Case 2 is explained by the fact that this Case was introduced in addition to the cases treated by [Schweitzer et al., 2003] and [Kirchengast et al., 2004b], without wanting to change numbering against these earlier studies.

These Cases were prepared for the ACE+ LEO-LEO forward modelling and characterize the basic atmospheric conditions (defined through refractivity, pressure,

temperature, and humidity) underlying the simulations. Based on these Cases, whose respective temperature and humidity profiles were shown earlier in Figure 4.4, ten sets with 40 occultation events each have been simulated. These sets can be subdivided into two groups: clear air simulations and cloudy and turbulent air simulations, respectively. The clear air simulations contain one set for each of the six scenarios defined above. Neither clouds nor turbulence have been taken into account; the modelled occultation data were impaired by instrumental errors only, which are composed of the following components (cf. Figs. 4.6–4.10), in line with the ACE+ system requirements [ESA, 2004c]:

<b>Error source</b>	<b>Strength</b>
Thermal noise	consistent with $C/N_0$ of 67 dBHz above the atmosphere
Amplitude drift	linear drift slope of 0.060 dB/min ( $\sim 0.5\%$ over 20 sec)
1/f noise	flicker noise model with a frequency range from 1/30 Hz to 5 Hz and a gain fluctuation of $3 \cdot 10^{-4} \text{ Hz}^{-1/2}$ at 1 Hz

The flicker noise model used for the modelling of 1/f noise was supplied by ESTEC (P. Silvestrin and N. Flourey, ESA/ESTEC, Noordwijk, Netherlands, pers. communications, 2004). For more information on such gain fluctuation spectra see [ESA, 2004b, Fig. 8-1, and related text].

The atmospheric profiles retrieved from the clear air simulations have been computed using moist air (cf. p. 70) retrieval without best-fit temperature extrapolation (cf. Subsect. 4.2.4, p. 72) and represent the retrieval performance under ideal, clear atmospheric conditions. The results are shown in Subsection 5.1.1 and serve, among other purposes, as reference profiles for the results of the four cloudy and turbulent air based sets.

The cloudy and turbulent air sets are based on Case 1, 6, 2 and 4 (instrumental errors included) supplemented by clouds and turbulence representative for each of these Cases. A simple cloud model received in its basic form (MatLab code) from Dr. P. Eriksson (Chalmers University of Technology, Göteborg, Sweden) has been used in order to mimic the cloudiness, and turbulence has been superimposed applying the turbulence/scintillation model from [Kuhn, 2003]. Both models are integrated within EGOPS5 and require input defining strength and location of the desired clouds and turbulence.

The cloud model simulates clouds as simple, horizontally-limited layers of a given thickness around a given cloud height with constant liquid water and/or ice water content. Since the cloud model simulates the clouds exactly like they are defined within the FoMod input file, it was necessary to generate 40 slightly different input files for each set in order to mimic cloud variability. For this, the cloud properties have been randomly varied around values typical for the location of the event. These values have been chosen following [Gradinarsky et al., 2003] which compiled,

together with G. Kirchengast (IGAM/University of Graz), typical cloud properties from literature. Furthermore, every second event of each set has been assumed to be cloudless because the average cloud coverage on earth amounts to about 50%. Turbulence realizations are computed randomly anyhow, so each input file within a set contained the same starting values — reasonable average turbulence parameters which have been derived from empirical results of Sterenborg and Baptista (see [ESA, 2004a] and references therein). The baseline specifications of clouds and turbulence for each of the Cases used for this part of the analysis are listed in Table 4.1. For comparability, they are the same as those used by [Kirchengast et al., 2004a] and [ESA, 2004a].

The atmospheric profiles retrieved from the simulated occultation events described above have been computed using cloudy air retrieval (cf. p. 70) together with best-fit temperature extrapolation from the CIRA86aQ\_UoG model. The results represent the performance of the ACE+ LEO-LEO retrieval under typical cloudy and turbulent air conditions and are shown and interpreted in Subsection 5.1.2.

	Cloud Specifications	Turbulence Specifications
C1	<b>3D Cumulonimbus clouds and precipitation</b> <b>(“cCp1”)</b> $lwc = 2.5 \text{ g m}^{-3} \pm 0.5 \text{ g m}^{-3}$ (rms; 1.5–3.5 $\text{g m}^{-3}$ ) $c\_height/lwc = 2 \text{ km} \pm 0.25 \text{ km}$ (rms; 1.5–2.5 km) $c\_thickness/lwc = 2 \text{ km} \pm 0.25 \text{ km}$ (rms; 1.5–2.5 km) $iwc = 0.15 \text{ g m}^{-3} \pm 0.05 \text{ g m}^{-3}$ (rms; 0.05–0.25 $\text{g m}^{-3}$ ) $c\_height/iwc = 9 \text{ km} \pm 0.5 \text{ km}$ (rms; 8–10 km) $c\_thickness/iwc = 3 \text{ km} \pm 0.5 \text{ km}$ (rms; 2–4 km) $rr = 20 \text{ mm h}^{-1} \pm 5 \text{ mm h}^{-1}$ (rms; 10–30 km) $rr\_topheight = 2.5 \text{ km} \pm 0.25 \text{ km}$ (rms; 2–3 km)	<b>tropical turbulence</b> <b>(“sTR1”)</b> $C_{n0}^2 = 2 \cdot 10^{-13} \text{ m}^{-2/3}$ $H_{Cn2} = 1 \text{ km}$
C6	<b>3D Cumulus clouds</b> <b>(“cCu1”)</b> $lwc = 0.5 \text{ g m}^{-3} \pm 0.25 \text{ g m}^{-3}$ (rms; 0–1 $\text{g m}^{-3}$ ) $c\_height = 2.5 \text{ km} \pm 0.25 \text{ km}$ (rms; 2–3 km) $c\_thickness = 0.3 \text{ km} \pm 0.05 \text{ km}$ (rms; 0.2–0.4 km)	<b>subtropical turbulence</b> <b>(“sST1”)</b> $C_{n0}^2 = 1 \cdot 10^{-14} \text{ m}^{-2/3}$ $H_{Cn2} = 1.5 \text{ km}$
C2	<b>3D Altostratus clouds</b> <b>(“cAs1”)</b> $lwc = 0.2 \text{ g m}^{-3} \pm 0.1 \text{ g m}^{-3}$ (rms; 0–0.4 $\text{g m}^{-3}$ ) $c\_height = 4.5 \text{ km} \pm 0.25 \text{ km}$ (rms; 4–5 km) $c\_thickness = 0.6 \text{ km} \pm 0.15 \text{ km}$ (rms; 0.3–0.9 km)	<b>mid-latitude turb.</b> <b>(“sML1”)</b> $C_{n0}^2 = 1.3 \cdot 10^{-15} \text{ m}^{-2/3}$ $H_{Cn2} = 2 \text{ km}$
C4	<b>3D Cirrus clouds</b> <b>(“cCi1”)</b> $iwc = 0.05 \text{ g m}^{-3} \pm 0.025 \text{ g m}^{-3}$ (rms; 0–0.1 $\text{g m}^{-3}$ ) $c\_height = 8 \text{ km} \pm 0.5 \text{ km}$ (rms; 7–9 km) $c\_thickness = 1.6 \text{ km} \pm 0.4 \text{ km}$ (rms; 0.8–2.2 km)	<b>high-latitude turb.</b> <b>(“sHL1”)</b> $C_{n0}^2 = 1 \cdot 10^{-16} \text{ m}^{-2/3}$ $H_{Cn2} = 2 \text{ km}$

Legend: C1 = Case1, C6 = Case6, C2 = Case2, C4 = Case4,  $lwc$ ... liquid water content (density) of cloud,  $c\_height$ ... center height of cloud,  $C\_thickness$ ... thickness of cloud around center height,  $iwc$ ... ice water content (density) of cloud,  $rr$ ... rain rate,  $rr\_topheight$ ... top height of rainfall,  $C_{n0}^2$ ... turbulence structure constant at surface,  $H_{Cn2}$ ... scale height of turbulence structure constant. The horizontal extent of clouds was set to 200 km for  $Ci$  and  $As$ , 100 km for  $Cu$  and 10 km for  $Cp$ .  $Cp$  has a gradual  $lwc$  decay over several kilometers above  $c\_thickness/lwc$ . The horizontal extend of turbulence was set to 200 km in all cases and the vertical  $C_n^2$  decay was assumed exponential with the scale height  $H_{Cn2}$ . The outer scale of turbulence was set to 100 m.

Table 4.1: Specification of the parameters for cloud and turbulence scenarios (after [Kirchengast et al., 2004b]).

### ECMWF Analysis Field

The second main part of the analysis are quasi-realistic simulations based on an ECMWF high-resolution analysis field which provides a quasi-realistic atmospheric state. In particular, an operational T511L60 analysis ( $\sim 40 \text{ km} \times 40 \text{ km}$  horizontal resolution, 60 vertical levels from surface to 0.1 hPa) of the ECMWF has been used (12 UTC analysis of September 15, 2002). Twelve different sets of events based on the ECMWF temperature and humidity fields, complemented by ECMWF 3D liquid water and ice water fields as well as modelled turbulence have been prepared. Furthermore, receiving system errors have been taken into account in the same manner as for the CIRA86aQ-UoG scenarios.

Starting from an ACE+ LEO-LEO MAnP1 full day simulation (input file in Appendix A.2) which yielded 232 occultation event locations evenly distributed around the earth, three latitude bands containing about a third of the events each — so-called sets — have been gathered:

Name	Covered Latitudes	No. of events
Low latitudes (GL)	30 °S – 30 °N	72
Mid latitudes (GM)	30 – 60 °S and 30 – 60 °N	90
High latitudes (GH)	60 – 90 °S and 60 – 90 °N	70

The event distribution is shown in Figure 4.17. For each of these latitude bands, four FoMod simulation scenarios have been computed under varying atmospheric conditions: clear (moist) air, cloudy air, cloudy and turbulent air, as well as cloudy and turbulent air including horizontal variability. Within the first scenario only ECMWF temperature and humidity fields have been used (see Fig. 4.18). The second scenario included the 3D liquid water and ice water fields of the analysis (see Figs. 4.18 and 4.19), too. Figures 4.18 and 4.19 serve to give an idea of the quasi-realistic nature of the ECMWF analysis used. In addition to clouds, the influence of turbulence was simulated within the third scenario. Finally, the fourth scenario resembles the third one plus additionally including the full horizontal variability of the analysis; while the first three scenarios adapted local spherical symmetry for each profile around its occultation event location where it was extracted. This allows for a clear quantification of the observational and retrieval errors in the first three scenarios, since the “representativeness error” of horizontal variability is disregarded. The 3D liquid water and ice water fields contribute in all cloudy scenarios to the absorption of the occultation signal at any location where occultation rays pass through clouds.

Turbulence has been simulated using the same turbulence/scintillation model as in the CIRA86aQ-UoG scenarios with the difference, that the main turbulence parameters were modelled as a function of latitude based on the turbulence settings

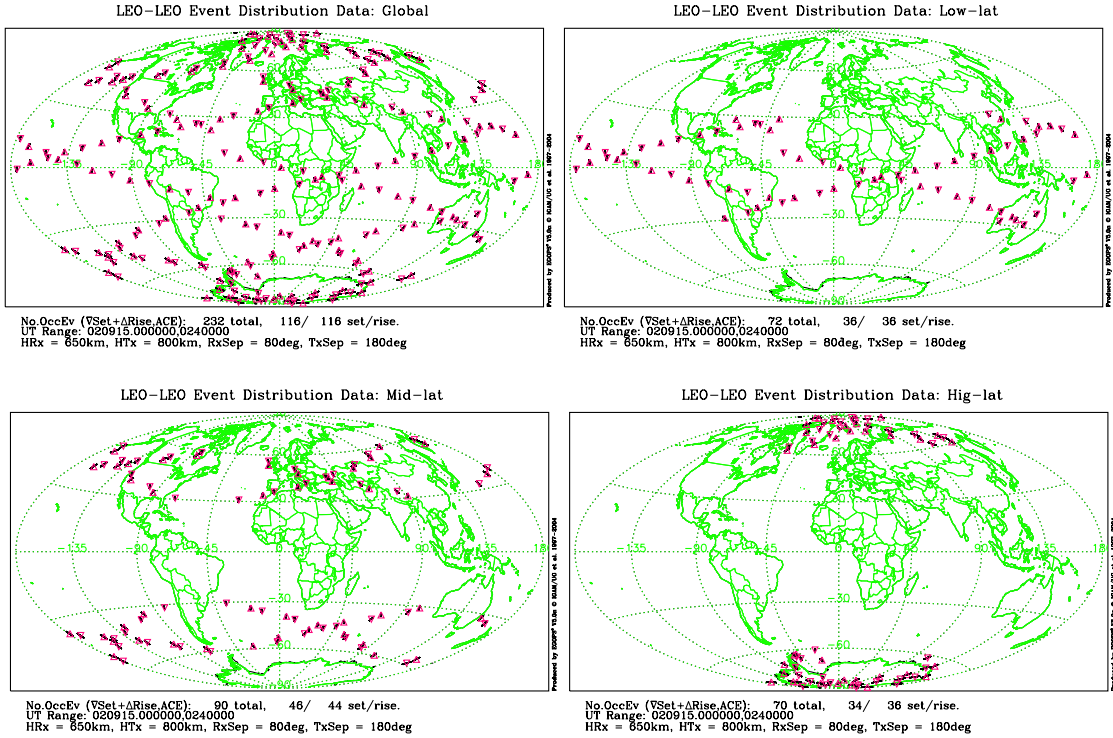


Figure 4.17: ACE+ LEO-LEO occultation event locations used in the ECMWF simulations: all events (upper left), low latitudes band (upper right), mid latitudes bands (lower left), high latitudes bands (lower right panel).

defined in Table 4.1. To be precise, distinct values of  $C_{n0}^2$  and  $H_{Cn2}$  have been attributed to latitudes  $0^\circ$  (“sTR1”),  $\pm 20^\circ$  (“sST1”),  $\pm 30^\circ$  ( $C_{n0}^2 = 3 \cdot 10^{-15} \text{ m}^{-2/3}$ ,  $H_{Cn2} = 1.75 \text{ km}$ ),  $\pm 50^\circ$  (“sML1”), and  $\pm 70^\circ$  (“sHL1”), respectively. Linear interpolation between these values provided a latitude dependent variation in strength of the scintillation effects, similar to real turbulence conditions. Turbulence beyond  $70^\circ$  has been assumed to be constant at the  $70^\circ$  values. This follows the assumptions of [Kirchengast et al., 2004a] for their ECMWF scenario.

The retrieval of atmospheric profiles from the forward simulations described above was carried out using cloudy air retrieval (cf. p. 70) combined — if activated by the retrieval — with best-fit temperature extrapolation from the ECMWF 24 h forecast for the analysis time. The best-fit profile was searched within a few degrees around the given event location and supplied with an uncertainty ranging from 0.75 K (near  $z_{\text{thresh}}$ , see p. 72) to 2 K (near 2 km). The results for the ECMWF scenarios are shown in Section 5.2, arranged in four subsections. The first three of them discuss the four scenarios subsequently for each latitude band in order to facilitate direct comparison between the retrieval performance under the different atmospheric conditions. The fourth compares the features of the single latitude bands among each other. Finally, in passing to Chapter 5, it is worth mentioning that the retrieval

results based on the ECMWF analysis represent a good approximation of the expected ACE+ LEO-LEO occultation observation retrieval performance in the real world.

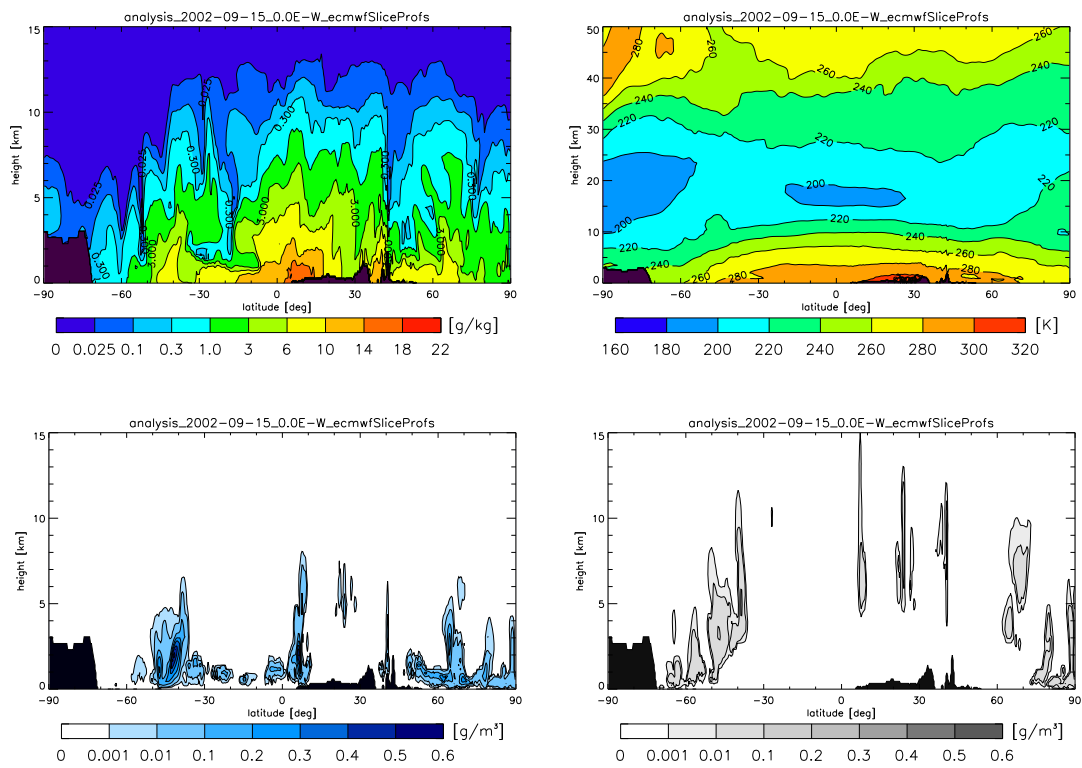


Figure 4.18: Latitude-height cross sections at  $0^\circ$  longitude through various ECMWF analysis fields (Sept. 15, 2002, 12 UTC): specific humidity (top left), temperature (top right), liquid water density (bottom left) and ice water density (bottom right). Source: [Kirchengast et al., 2004a]

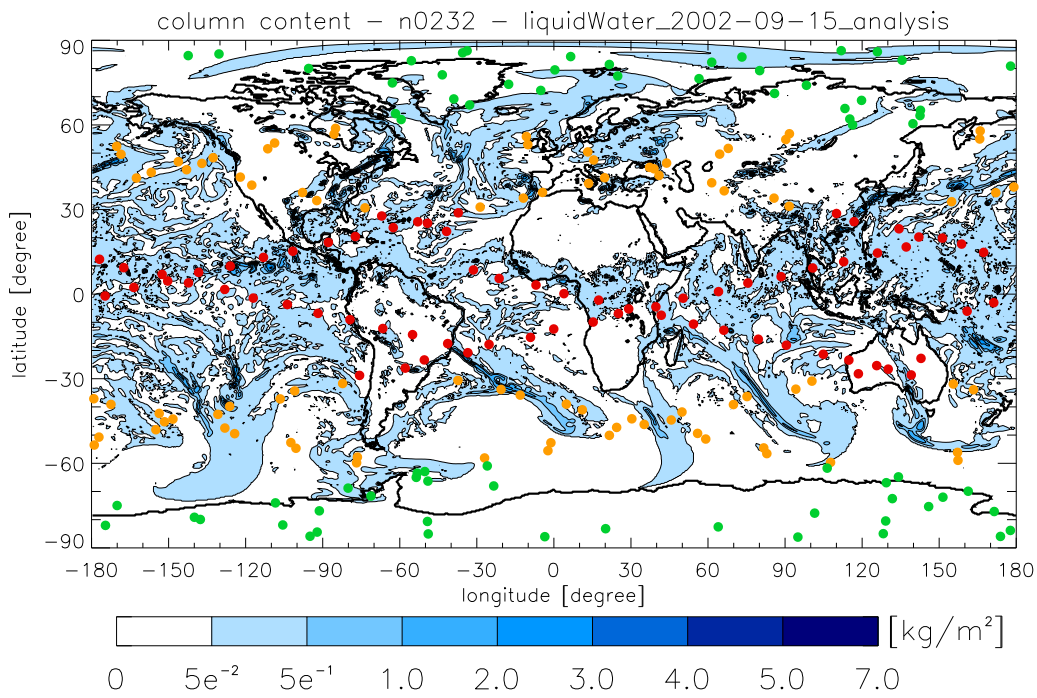


Figure 4.19: Vertically integrated liquid water density (unit  $\text{kg m}^{-2}$ ) indicating cloud coverage (data from Sept. 15, 2002, 12 UTC, ECMWF analysis). The dots represent the occultation event coverage again: low latitudes (red), mid latitudes (orange), high latitudes (green). Source: M. Schwarz/IGAM, 2004.



# Chapter 5

## Performance Analysis Results and Discussion

Within this chapter, the results of the statistical performance analysis described in Section 4.3 will be presented and discussed. The displayed figures aim at giving a visual estimate of the magnitudes at which the humidity and temperature retrieval errors are to be expected and how they compare with the observational ACE+LEO-LEO requirements which are listed in Table 3.1. First, the part of the analysis based on the climatological atmosphere model will be considered (Sect. 5.1), followed by the performance results based on the ECMWF analysis field. The vertical resolution of all retrieved profiles is — consistent with the respective ACE+ threshold requirements — about 1 km. To start with, all results have been found to essentially lie within the threshold requirements and nearly all results even meet the target requirements which were summarized in Table 3.1 mentioned above.

### 5.1 Analysis based on Climatological Atmosphere

This section discusses the results of temperature and humidity retrieval for different scenarios based on the climatological atmosphere model CIRA86aQ\_UoG. Two parts will be considered separately: The first part deals with the retrieval performance in clear air and shows the results of six sets containing 40 occultation events each, which are based on the six Cases as defined in Section 4.3 (p. 78) including errors due to the receiving system as also defined in Section 4.3 (p. 79). Neither clouds nor turbulence have been superimposed on the basic atmospheric state (defined through pressure, temperature, humidity) which is specified by the selected Case. Thus, the profiles retrieved from these scenarios represent the performance of the retrieval under ideal atmospheric conditions which would allow to investigate instrumental errors such as done by [Kirchengast et al., 2004b] for five of these six cases. Here, the purpose of the sets prepared for this part of the analysis is to

give an idea of the retrieval performance at different geographical latitudes during different seasons (summer and winter). Furthermore, they serve for comparison to the results of the second part.

The second part contains four sets at different latitudes, each consisting of 40 occultation events based on Case 1 (tropical), Case 6 (subtropical), Case 2 (mid-latitude) and Case 4 (high-latitude), respectively. A related analysis has been reported by [Kirchengast et al., 2004a] and [ESA, 2004a], where the four sets had all been based on Case 2 (mid latitude), however. The difference of this part of the analysis to the first part is that now turbulence as well as clouds have been accounted for. In particular, typical cloud and turbulence scenarios representative for each of the Cases have been derived from characteristic values occurring in the real world. The detailed specifications are listed in Table 4.1 and complementary descriptions are found on page 79. This part of the analysis aims at showing the performance of the retrieval under typical atmospheric conditions which usually are partly cloudy and disturbed. In this connection, the influence of various types of clouds and strengths of turbulence on the retrieval shall be discussed for example through comparison with the clear air scenarios.

### 5.1.1 Clear Air

Figures 5.1–5.6 show the statistical temperature and humidity performance analysis results for the clear, non-turbulent air scenarios. The left panels on each figure show the “true” profile on which the forward simulations of a set were based (cf. Fig. 4.4). On the middle panels, the absolute errors between retrieved and true profiles are displayed and the right panels show the relative retrieval errors. In particular, the errors were statistically analyzed over all profiles of a set and mean bias (thick green line), bias uncertainty (two times the standard deviation of the bias, thin green line) and standard deviation (thick blue line) have been drawn. The two standard deviations were depicted as  $\pm$  envelopes around the bias profile. In order to facilitate the interpretation, some error panels include thin black lines, too. They represent the observational requirements as listed in Table 3.1; the dashed black lines are the target requirements and the solid black lines the threshold requirements.

As can be seen from the figures, both humidity and temperature profiles for all scenarios lie within the target requirements at essentially all heights. The error of specific humidity typically does not exceed 3% between 2 and  $\sim 8$  km and this 3% area even reaches up to  $\sim 10$  km for Cases 1, 6, and 2. The high-latitude winter scenario is an exception in that its relative error is much larger — which becomes clear regarding the very small amount of water vapour present under the conditions of this scenario ( $< 0.2 \text{ g kg}^{-1}$  at 2 km height already). The 5% error boundary reaches up to  $\sim 9$  km for Cases 3 and 4 and even up to  $\sim 12$  km for Cases 1, 6, and 2. The error oscillations above are mainly due to remaining technical

weaknesses of the present not fully optimized end-to-end simulation [Kirchengast et al., 2004a].

Regarding the temperature retrieval results, we can see a small constant residual bias of near 0.1 K below a height of 20 km which is also caused by the not yet fully optimized end-to-end simulation mentioned above. The statistical temperature error (standard deviation) is smaller than 1 K within the lower troposphere and smaller than 0.5 K throughout the upper troposphere and lower stratosphere. Above 10 km, the error is even smaller than 0.25 K. Thus, the temperature retrieval fully meets the target requirements.

Finally, a phenomenon occurring in humid regions shall be explained. As can be seen from the results of the tropical scenario (Case1), humidity and temperature drift and get biased close to a height of 2 km. This does not stem from an inadequacy of the retrieval chain but is attributable to the high abundance of water vapour in the tropics (in this case  $\sim 12 \text{ g kg}^{-1}$  at 2 km). This makes the signal-to-noise ratio in lower regions so weak that accurate retrieval from transmission data is no longer possible. Generally, it is true for the ACE+ frequencies that the retrieval reaches the deeper the lower the amount of water vapour in the atmosphere is; and transmission retrievals can be accurate up to specific humidities of  $\sim 10 \text{ g kg}^{-1}$ . Practically, this effect is avoided by using additional information below 3 km, such as for example the best-fit temperature extrapolation (see Subsect. 4.2.4, p. 72) which has not been applied to this part of the analysis.

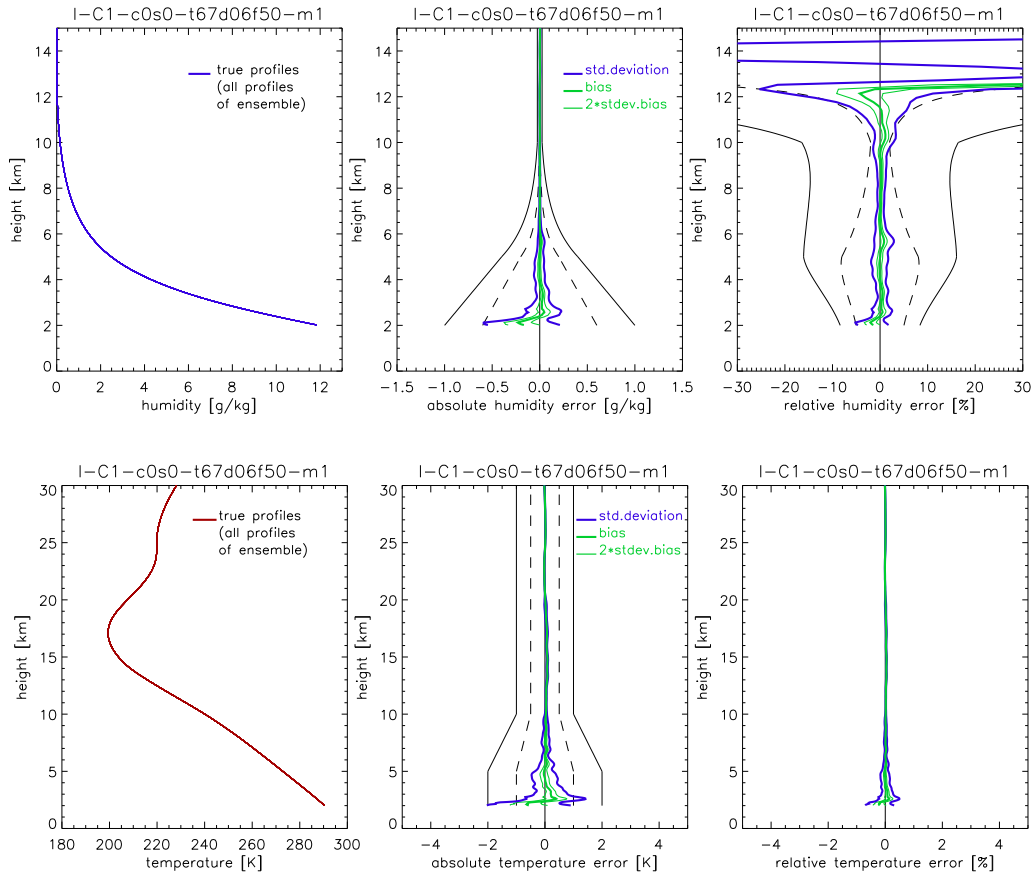


Figure 5.1: Humidity (upper panels) and temperature (lower panels) retrieval results for the clear-air, non-turbulent tropical (Case1) scenario. The left panels illustrate the atmospheric profile underlying the retrievals. The middle panels show the absolute retrieval error and the right panels the relative retrieval error. The errors are illustrated in terms of statistical performance analysis results. In particular, standard deviation (thick blue lines), mean bias (thick green line), and bias uncertainty (two times the standard deviation of the bias, thin green lines) are shown. The standard deviations are depicted as  $\pm$  envelopes around the mean bias profile. Furthermore, the observational requirements as listed in Table 3.1 are shown for reference: the solid black lines represent the threshold requirements and the dashed black lines the target requirements.

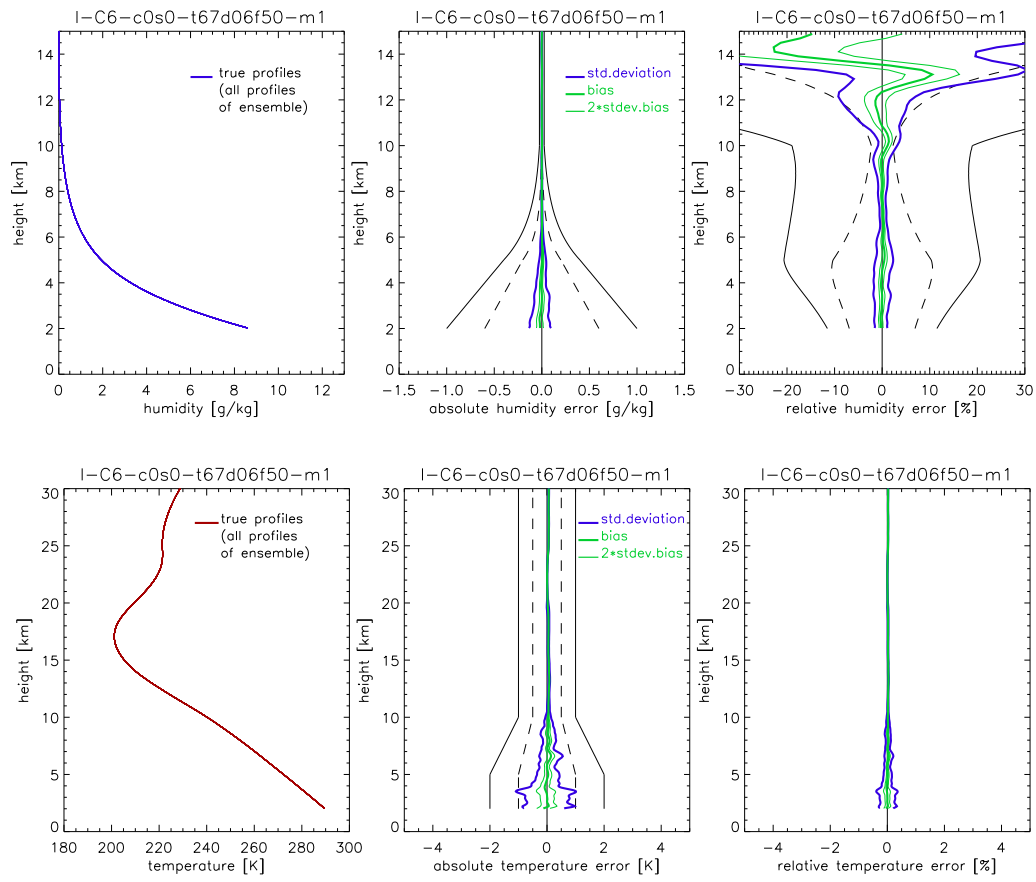


Figure 5.2: Humidity (upper panels) and temperature (lower panels) retrieval results for the clear-air, non-turbulent subtropical summer (Case6) scenario. The layout is the same as in Fig. 5.1.

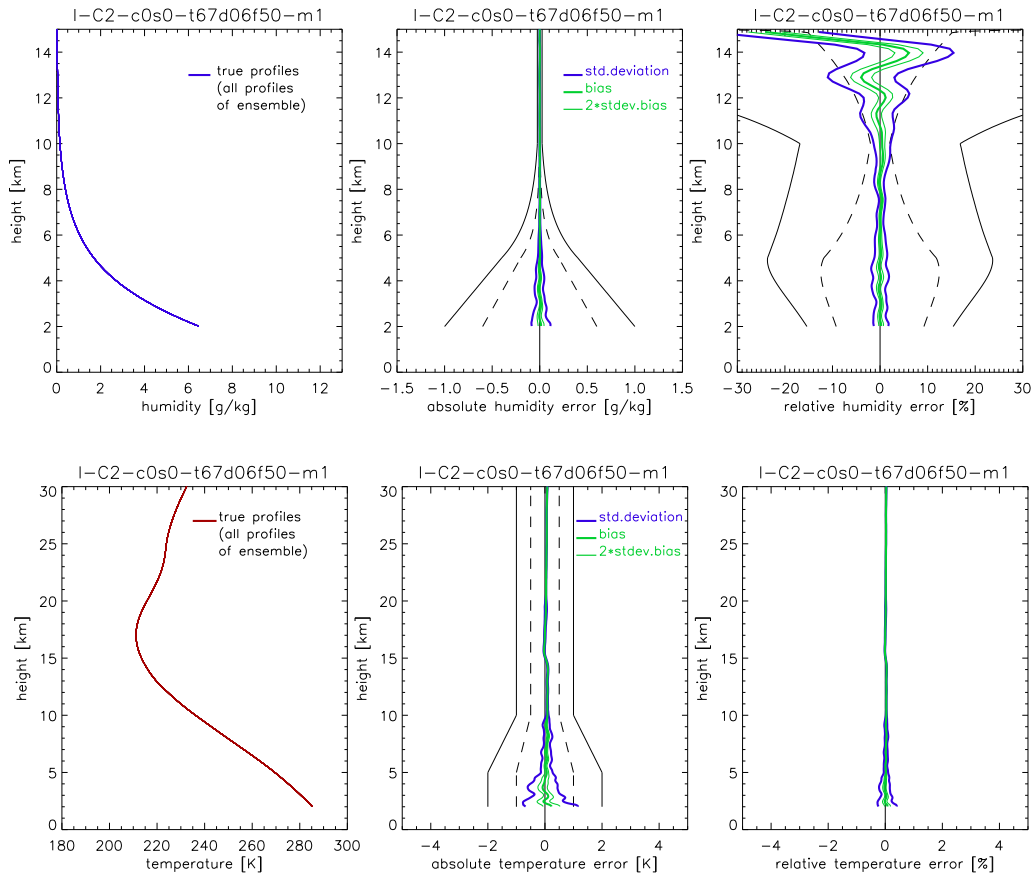


Figure 5.3: Humidity (upper panels) and temperature (lower panels) retrieval results for the clear-air, non-turbulent mid-latitude summer (Case2) scenario. The layout is the same as in Fig. 5.1.

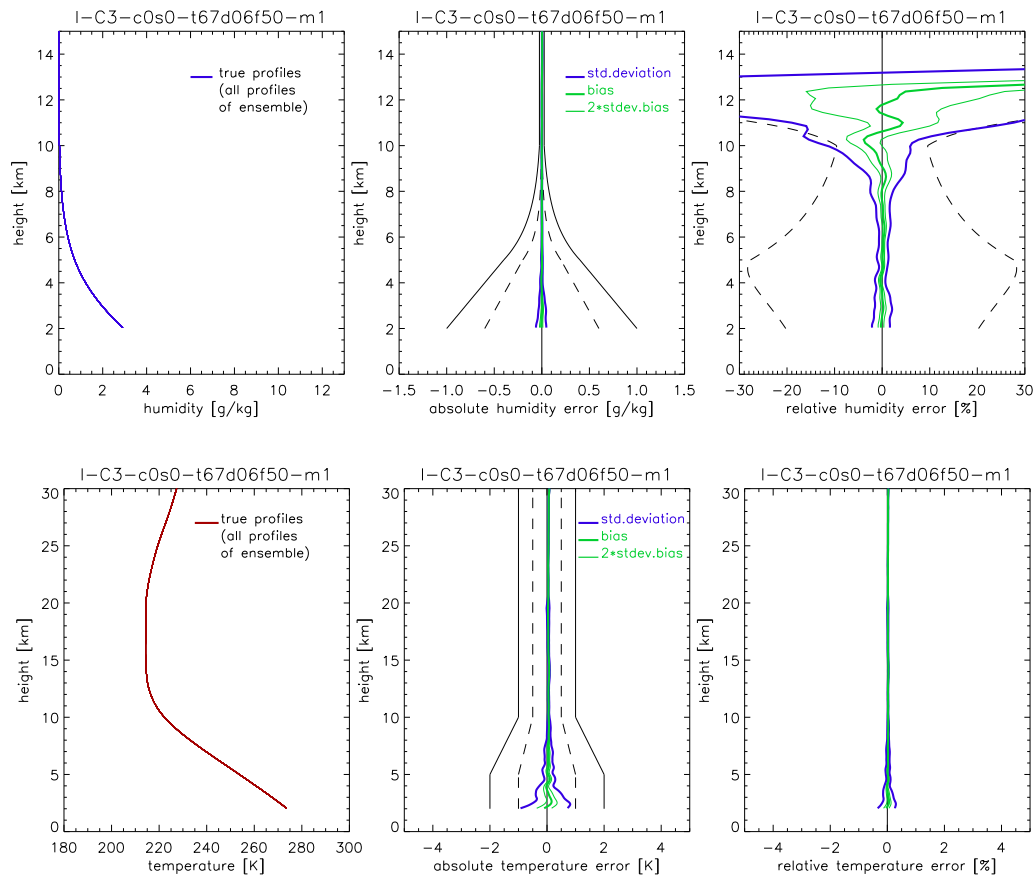


Figure 5.4: Humidity (upper panels) and temperature (lower panels) retrieval results for the clear-air, non-turbulent mid-latitude winter (Case3) scenario. The layout is the same as in Fig. 5.1.

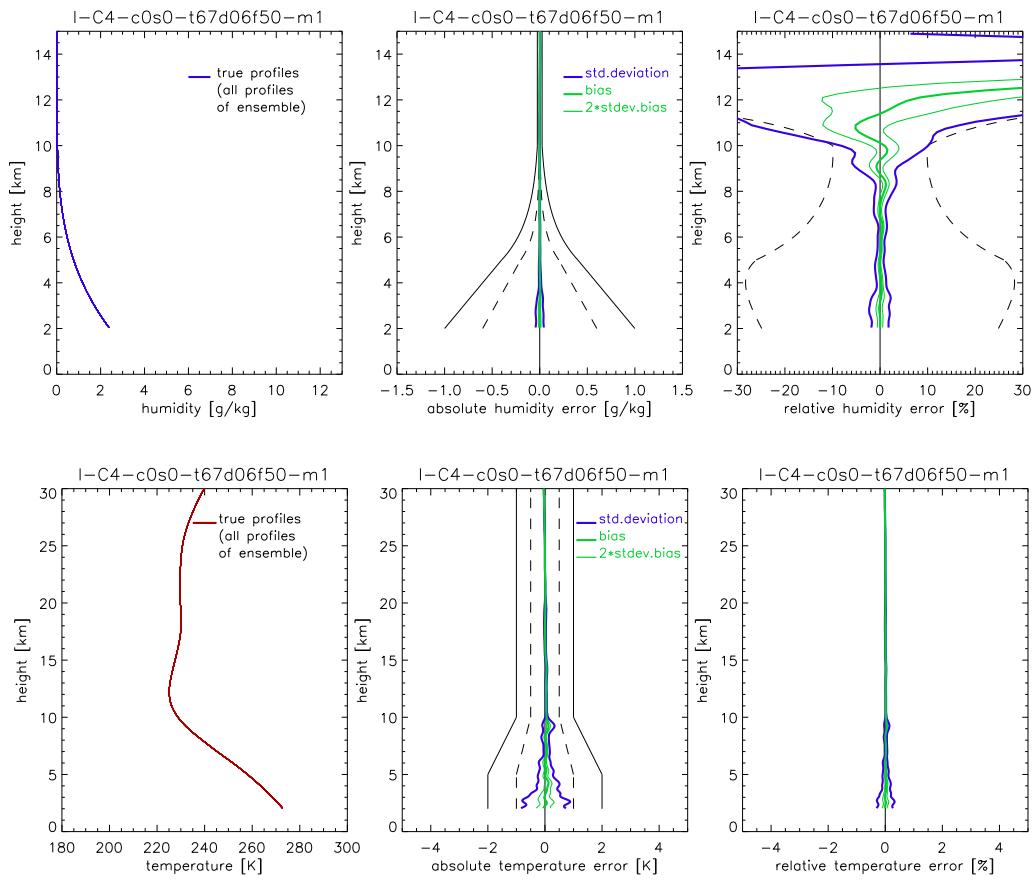


Figure 5.5: Humidity (upper panels) and temperature (lower panels) retrieval results for the clear-air, non-turbulent high-latitude summer (Case4) scenario. The layout is the same as in Fig. 5.1.

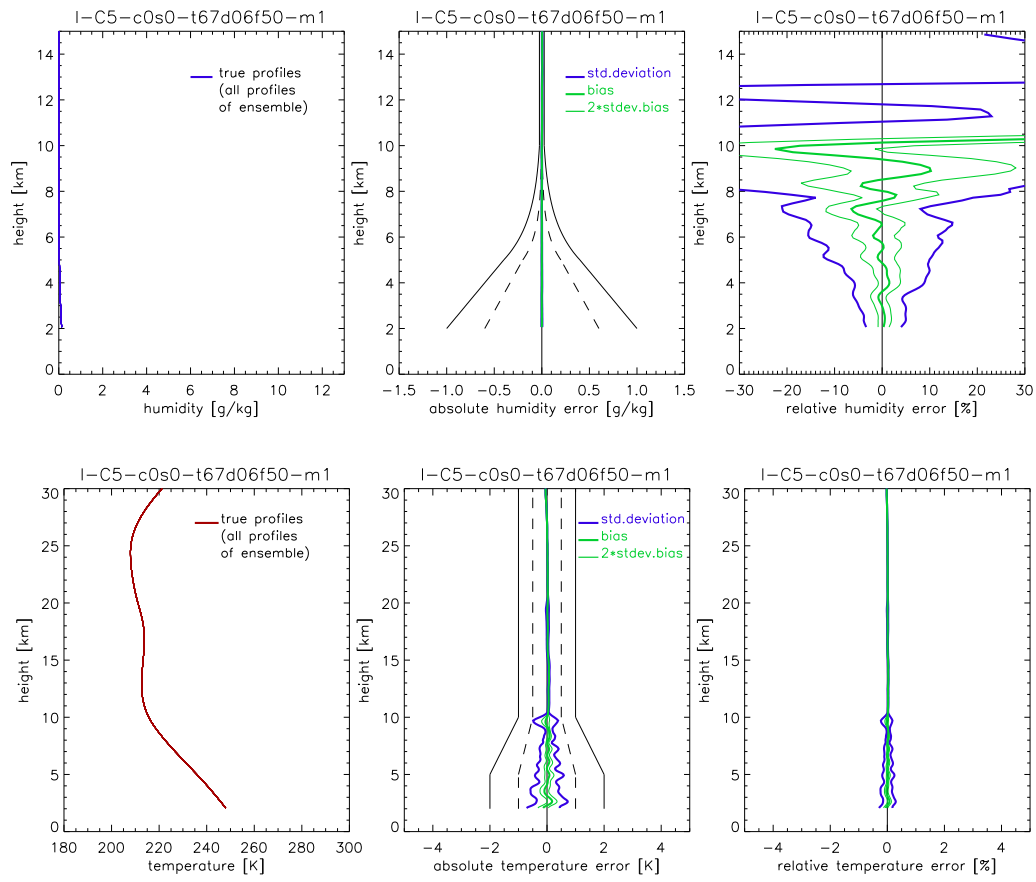


Figure 5.6: Humidity (upper panels) and temperature (lower panels) retrieval results for the clear-air, non-turbulent high-latitude winter (Case5) scenario. The layout is the same as in Fig. 5.1.

### 5.1.2 Cloudy and Turbulent Air

This subsection comprises the temperature and humidity retrieval performance results for the cloudy and turbulent air scenarios based on the climatological atmosphere model (see Figs. 5.7–5.10), as summarized in the introduction to Section 5.1 above. Just like the results of the clear air scenarios, the profiles lie within the target requirements at nearly all heights and are essentially unbiased. Generally, the cloudy and turbulent air results resemble the clear air results from about 6 km upwards except for sporadic differences due to the statistical nature of the ensemble simulations (e.g., instrumental errors randomly generated). For instance, the “bumpy” feature which can be seen in the standard deviation on the temperature plot of Figure 5.9 (cf. Fig. 5.3) at a height of approximately 10 km arises from a single profile, whose error is much larger than that of the other profiles, but not large enough to be corrected automatically during the data processing, where outliers are removed. Something similar can be found in Figure 5.5 (cf. Fig. 5.10) at a height of about 9.5 km. How exactly these sporadic outliers emerge from weaknesses of the retrieval chain was, due to time constraints, not yet determined based on the simulations presented so far. Also the simulations based on the ECMWF analysis field shown below in Section 5.2 point at a weakness around 10 km, which is related to a not fully optimized filtering and weighting of the transmission data at the different frequencies (see Sect. 5.2). Future improvements will include to carefully address this weakness.

Considering the lower 6 km, the errors are larger than in the clear air scenarios. Especially the relative error of the specific humidity amounts to about 5% (Cases 1 and 2) and 10% (Cases 6 and 4), respectively. The temperature profiles show approximately the same performance as in the clear air Cases, which means that the relative error is mostly smaller than  $\sim 0.5\%$  and that the absolute error reaches up to 1–1.5 K. Closer investigation indicated that this widening of the errors is not only due to the influence of clouds and turbulence. It is rather a property of the cloudy air retrieval (symbol c1) itself, due to the different weighting scheme for the transmissions from the three channels used in case cloud liquid water is an additional retrieved variable (while assumed zero in the moist air retrieval). This is confirmed by analyzing the clear air scenarios using the cloudy air retrieval: the evaluation of the clear air occultation data with the cloudy air retrieval method yields larger errors than the evaluation with the moist air retrieval method (symbol m1) — but this does not mean that the moist air retrieval applied to the cloudy and turbulent air Cases would also produce better results than the application of the cloudy air retrieval. The temperature and humidity results of the clear air scenarios computed with the cloudy air retrieval are shown in Figure 5.11 (see caption for details). Comparing these profiles with the cloudy and turbulent air results shows that the retrieval performance is approximately the same with and without atmospheric disturbances. Thus, the cloudy air retrieval is widely insensitive to clouds and turbulence. In practice, where cloudiness conditions are not known a priori, clearly always cloudy air retrieval (i.e. allowance for liquid water) will be

required below about 8 km.

The main reason for this good performance is the integrated best-fit temperature extrapolation which comes into play if severe turbulence and/or dense clouds occur. In such a case, a so called threshold height  $z_{\text{thresh}}$  is determined, below which the atmosphere is strongly influenced (see p. 72). Below this height, auxiliary temperature information is involved which levels out the effects of clouds and turbulence and thus enables accurate retrieval even under disturbed conditions.

Generally, clouds in terms of their liquid/ice water absorption effects have been found to have less influence on the retrieval than turbulence, and the presumed insensitivity to ice clouds was confirmed [Gradinarsky et al., 2003]. Rain (not specifically analyzed here) strongly increases the absorption of the transmitted signals and therefore, the impact on the retrieval is similar to that of turbulence; the influence of rain, however, is in general relevant below 3 km only.

On closer inspection of the results it is noticeable that the profiles belonging to the high-latitude summer scenario exhibit the largest errors (cf. Figs. 5.10 and 5.11) although this case is influenced by the weakest turbulence. On the other hand, the profiles of the strongly influenced tropical scenario (cf. Fig. 5.7) look even better than the appropriate clear air results (cf. Fig. 5.11). This is because of a different incorporation of the auxiliary temperature profile. Since the strength of turbulence is low in the high-latitude Case, the conditions leading to a definition of  $z_{\text{thresh}}$  are not reached in most of the events of the set, which is why almost no auxiliary temperature information is used above 3 km. In the tropical Case however, a  $z_{\text{thresh}}$  between 4 and 7 km ensures accurate retrieval below. The same applies to the other two scenarios, where  $z_{\text{thresh}}$  lies between about 3 km and 6 km (Case2) or between 3 km and 5 km (Case6).

All in all, the results of the ten sets discussed so far look very promising and indicate the unique potential of the LEO-LEO radio occultation technique for determining accurate and unbiased humidity and temperature profiles; even though the cloudy and turbulent air results beneath about 5 km are better than they can be expected to be under real conditions, since the search library for the best fitting temperature profile was the CIRA86aQ\_UoG climatology itself. However, results of the ECMWF based sets show that a realistic search library with temperature uncertainties of 0.75–2 K is sufficient in order to enable accurate retrieval throughout the lower troposphere. These ECMWF based results are discussed in Section 5.2 below.

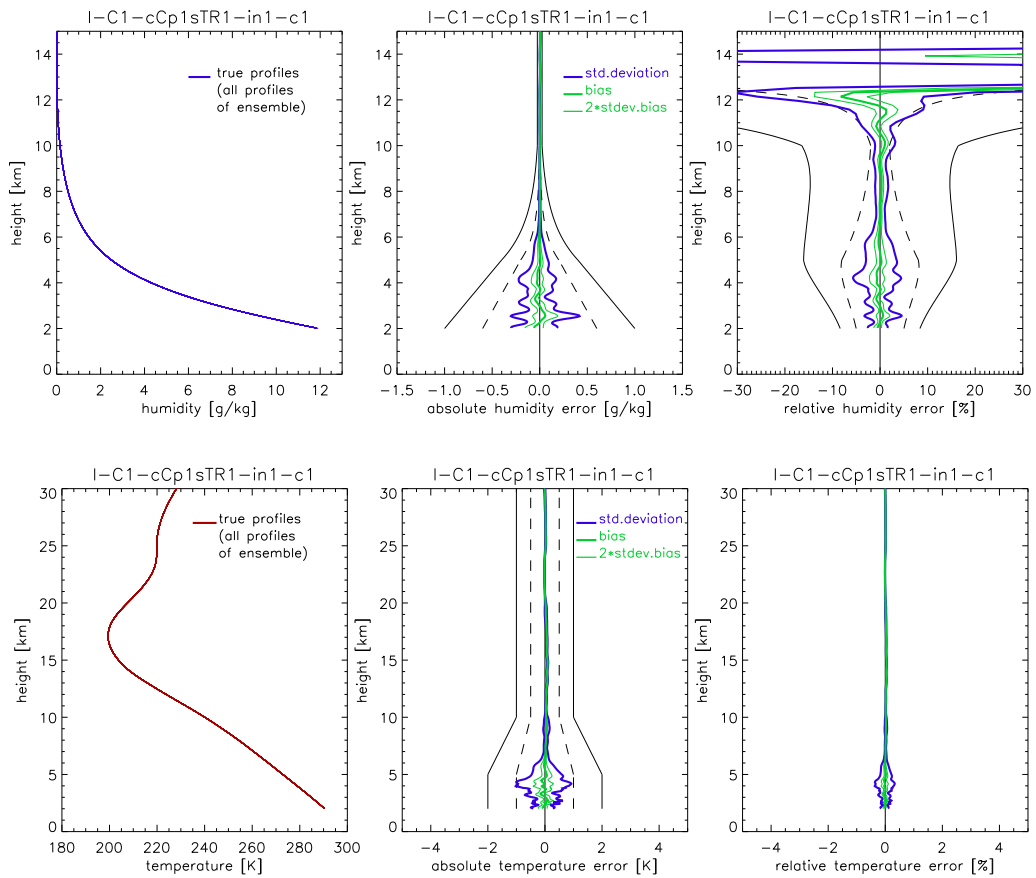


Figure 5.7: Humidity (upper panels) and temperature (lower panels) retrieval results for the cloudy and turbulent air tropical (Case1) scenario. The layout is the same as in Fig. 5.1.

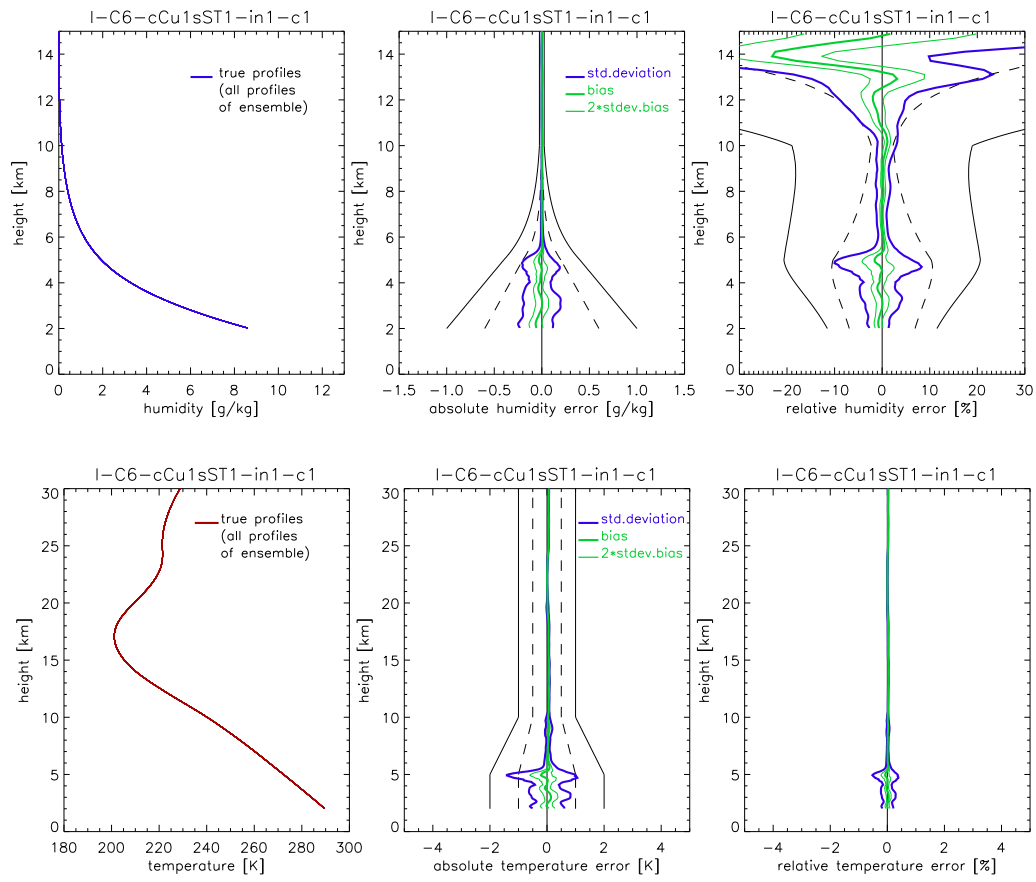


Figure 5.8: Humidity (upper panels) and temperature (lower panels) retrieval results for the cloudy and turbulent air subtropical summer (Case6) scenario. The layout is the same as in Fig. 5.1.

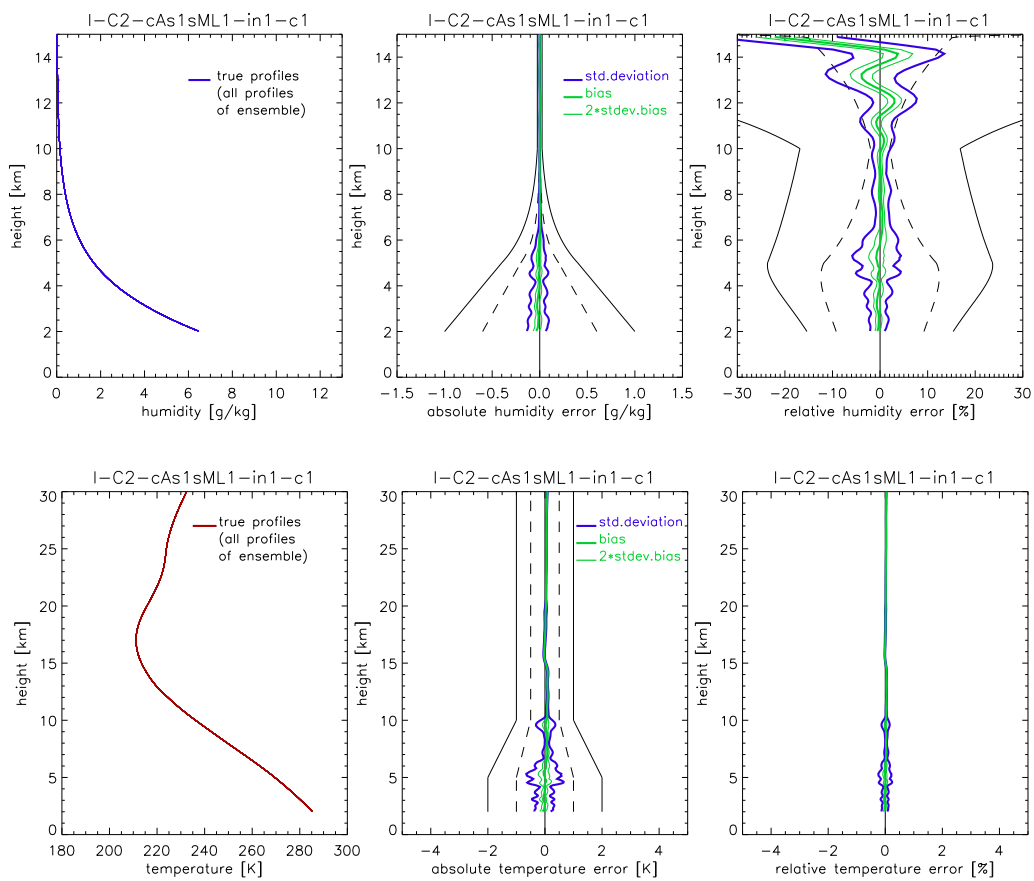


Figure 5.9: Humidity (upper panels) and temperature (lower panels) retrieval results for the cloudy and turbulent air mid-latitude summer (Case2) scenario. The layout is the same as in Fig. 5.1.

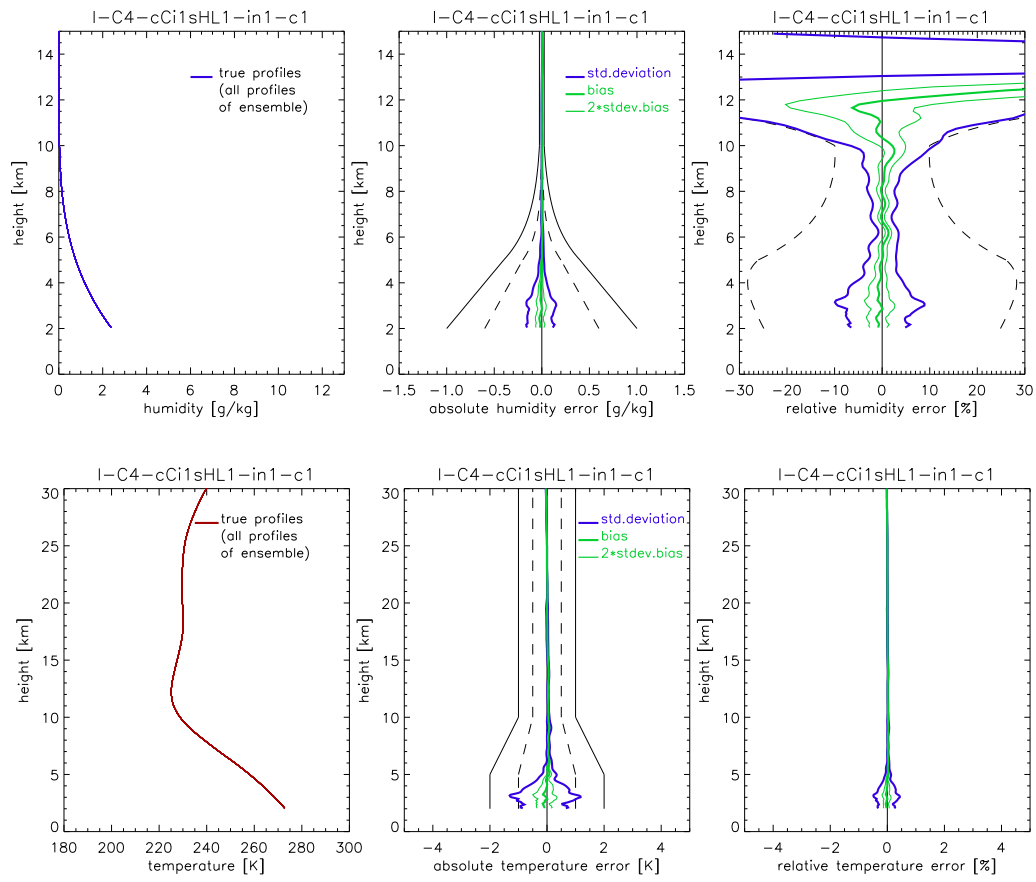


Figure 5.10: Humidity (upper panels) and temperature (lower panels) retrieval results for the cloudy and turbulent air high-latitude summer (Case4) scenario. The layout is the same as in Fig. 5.1.

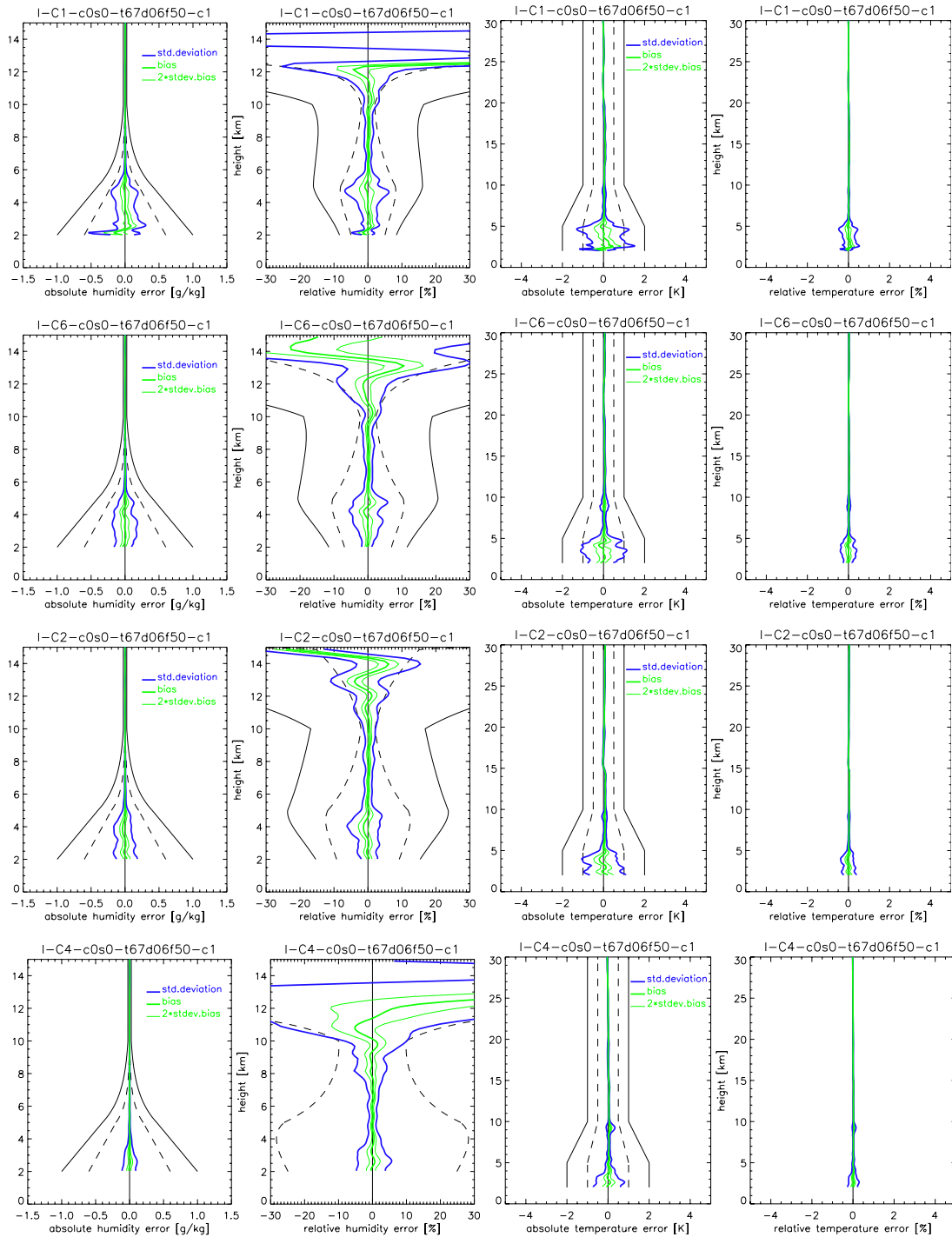


Figure 5.11: Humidity and temperature retrieval results for various clear air scenarios, computed applying cloudy air retrieval (symbol c1). The tropical (top row), subtropical (second row), mid-latitude summer (third row), and high-latitude summer (bottom row) scenarios, respectively, are displayed. In contrast, the results which are shown in Subsection 5.1.1 have been retrieved using moist air retrieval (symbol m1) within EGOPS5.

## 5.2 Analysis based on ECMWF Analysis Field

This section summarizes the temperature and humidity retrieval results for the clear, cloudy, and cloudy and turbulent air scenarios based on the ECMWF high resolution (T511L60) analysis field of September 15, 2002. Since ECMWF fields are quasi-realistic for this purpose, the results of this part of the analysis will be a good approximation to the real ACE+ LEO-LEO radio occultation retrieval performance. The analysis is divided into four parts. The first part deals with the retrieval performance at high latitudes, the second part with that at mid latitudes, and the subject of the third part is the performance at low latitudes. For each of these parts, a set of about 70–90 occultation events (see Fig. 4.17 or 4.19) was available as a basis for closer investigations, since one full day of ACE+ LEO-LEO occultation events was simulated (see Fig. 4.19). In particular, each of these three sets served for the computation of four different scenarios accounting for various atmospheric conditions (clear air, cloudy air, cloudy and turbulent air, cloudy and turbulent air including horizontal variability) and the results were compared with each other. The detailed specifications of the scenarios were introduced in Subsection 4.3 above. Finally, the fourth part of this section deals with the differences and similarities of the first three parts.

The overall aim of this section is to assess the retrieval performance (the retrieval mode applied was the cloudy air retrieval) under the ECMWF based quasi-realistic atmospheric conditions defined for this purpose. This is done via comparison of the four scenarios for each latitude band (clear air, cloudy air, cloudy and turbulent air, cloudy and turbulent air including horizontal variability). Furthermore, the general performance of the retrieval in each latitude band will be investigated and compared with that of the other latitude bands. These results significantly expand those of [Kirchengast et al., 2004a] and [ESA, 2004a], where cloudy and turbulent air was used as the single scenario based on low-, mid-, and high-latitude data sets comprising half of a full-day (every 2<sup>nd</sup>) of LEO-LEO occultation events.

### 5.2.1 High Latitudes

This subsection comprises the results of the temperature and humidity performance analysis of the high-latitude band (60–90 °N plus 60–90 °S, see Fig. 4.17). In particular, Figure 5.12 depicts the clear air scenario, Figure 5.13 the cloudy air scenario and Figure 5.14 the cloudy and turbulent air scenario. The atmosphere underlying the scenario of Figure 5.15 is cloudy and turbulent as well, but with the difference that horizontal variability is included, too, while local spherical symmetry was used in the former three scenarios for the temperature and humidity profiles at the event locations.

The left panels of each figure illustrate the variety of atmospheric humidity and temperature conditions comprised by the complete set. They show that there are

profiles not completely reaching down to 2 km — this effect actually also appears in the mid- and low-latitude band. This is partly caused by the topography and partly due to multipath effects in the lower troposphere limiting the ray-tracing in the forward modelling. The latter effect could be treated applying a more elaborate wave-optics forward modelling which would result in a somewhat better performance in terms of lower penetration ([Kirchengast et al., 2004a], [Gorbunov and Kirchengast, 2004]).

The middle and right panels on each figure depict the absolute and relative errors, respectively, which are illustrated in terms of statistical measures — the layout is the same as on the figures in the climatological atmosphere model based scenarios. On the whole, all results meet the threshold requirements, and even the target requirements are met at nearly all heights. Additionally, the profiles have no significant biases. Considering the retrieval of specific humidity, all results show nearly the same performance above a height of approximately 7.5 km. The relative errors at these heights are quite large, and above about 10 km they exceed the target requirements. That is not surprising regarding the very small amount of water vapour at upper heights and especially at high latitudes. However, a considerable part of the relative errors arises from the not yet fully optimized LEO-LEO end-to-end simulator and partly also from unrealistically low humidities in some ECMWF analysis profiles above 10 km (logarithmic plots, not separately shown, reveal partly concentrations  $< 0.001\text{g kg}^{-1}$  which is below any reasonable stratospheric concentrations; e.g., [Salby, 1996]). More skillful filtering and weighting of transmission and imaginary refractivity in future will lead to further improvement of the results. The results below 7.5 km indicate that cloud liquid water has a smaller influence on humidity retrieval than turbulence since Figures 5.12 and 5.13 show approximately the same errors (RMS below 10%), whereas the scenarios including turbulence exhibit larger errors (RMS up to 15%). Equally important, the similarity of the turbulent air scenarios (Figs. 5.14 and 5.15) shows that horizontal variability has nearly no influence on the humidity retrieval at high latitudes. This is to a main part caused by the small quantity of water and humidity beyond  $60^\circ$  latitudes (polar regions).

The temperature retrieval results of the scenarios assuming spherical symmetry (Figs. 5.12–5.14) are similar above 5 km and the errors do not exceed 0.5 K. Above 10 km, the errors are even below 0.25 K. Within the lower troposphere, the errors of the turbulent air scenarios are somewhat larger than those of the other two scenarios. But in both cases, they lie around 1 K. The results of the scenario including horizontal variability show a small widening of the errors between 5 km and 30 km due to the horizontal variations; but they are still within the target requirements. The performance beneath is about the same as in the turbulent air case without horizontal variability. It should be noted at this point, that “errors” due to horizontal atmospheric variations, which are “representativeness” errors, are not considered to be part of the ACE+ observational requirements, since to what degree they exist depends on whether the data are interpreted as local profiles (as

done here for illustration purposes) or as properly along-ray averaged (as should be done in practice, see, e.g., comments in [Kirchengast et al., 2004a]).

One feature noted in all four scenarios is the small “bumpy” feature of the temperature error profiles at a height of about 10 km. As discussed in Subsection 5.1.2 (p. 5.1.2), this is due to the still sub-optimal filtering and weighting of the different channels in the current algorithm. More precisely, in the settings used here, the information from imaginary refractivity of the frequency channels F1 (9.7 GHz) and F2 (17.25 GHz) changes suddenly from nearly zero above 10 km to full weight below. Improved weighting in the future will eliminate this effect.

Altogether, the retrieval performance of humidity and temperature at high latitudes has proven to be consistent with the general ACE+ LEO-LEO requirements listed in Table 3.1. The humidity results lie well within the target requirements from 2 km to about 9 km and are not far from them above. The temperature results even meet the target requirements from top to bottom.

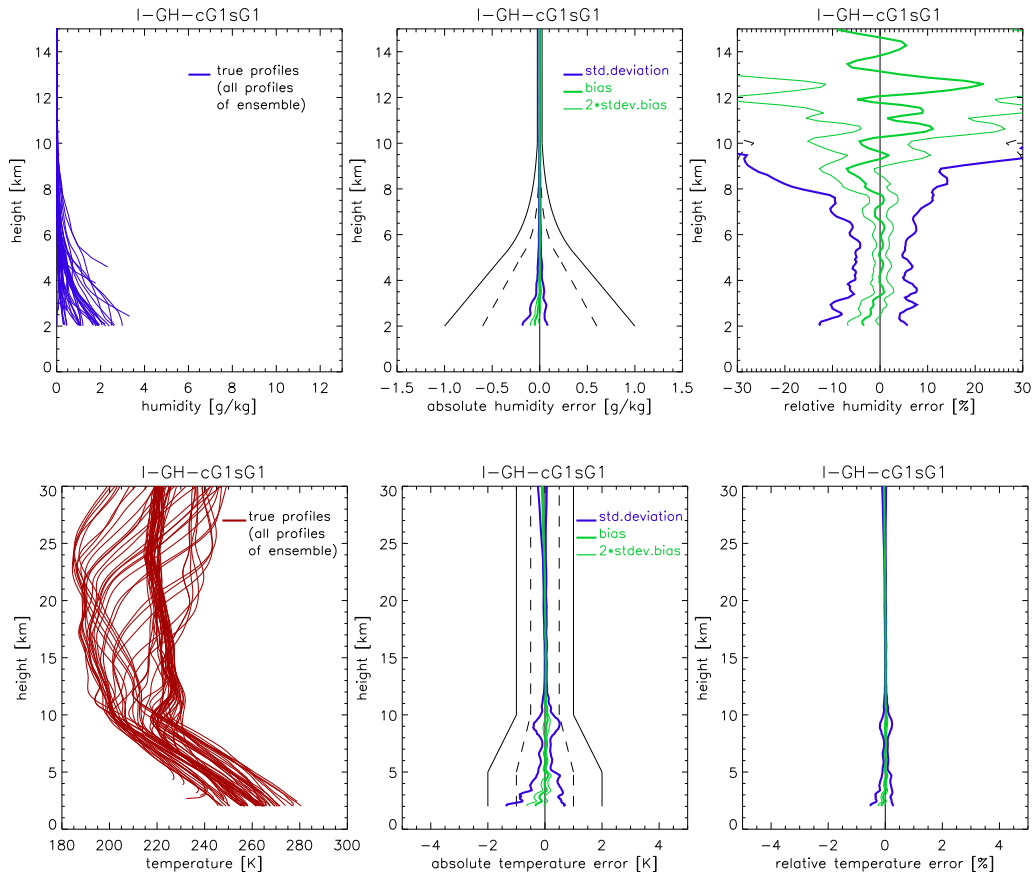


Figure 5.12: Humidity (upper row) and temperature (lower row) retrieval results for the high-latitude clear air scenario. The left panels illustrate the wide variety of atmospheric conditions covered by the profiles (summer and winter polar region are clearly discernible). The middle panels show the absolute retrieval error and the right panels the relative retrieval error. The errors are illustrated in terms of statistical performance analysis results. In particular, standard deviation (thick blue lines), mean bias (thick green line), and bias uncertainty (two times the standard deviation of the bias, thin green lines) are shown. The standard deviations are depicted as  $\pm$  envelopes around the mean bias profile. Furthermore, the observational requirements as listed in Table 3.1 are depicted for reference; the solid black lines represent the threshold requirements and the dashed black lines show the target requirements.

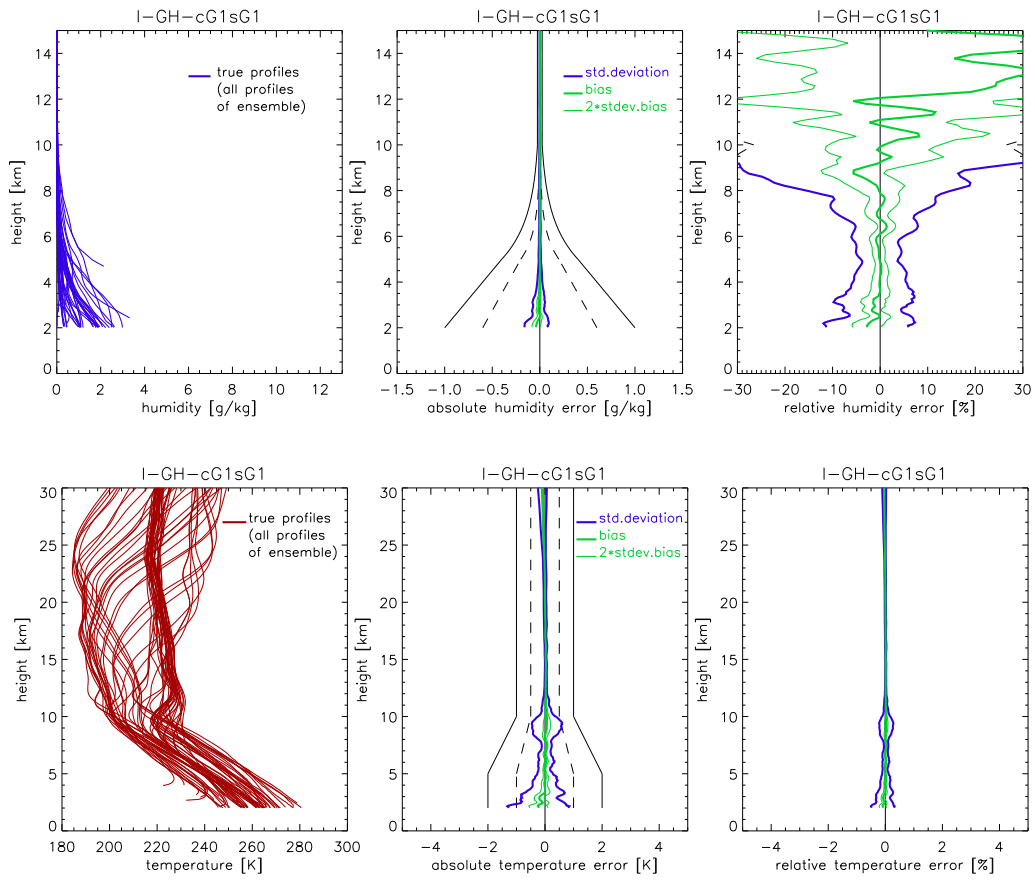


Figure 5.13: Humidity (upper row) and temperature (lower row) retrieval results for the high-latitude cloudy air scenario. The layout is the same as in Fig. 5.12.

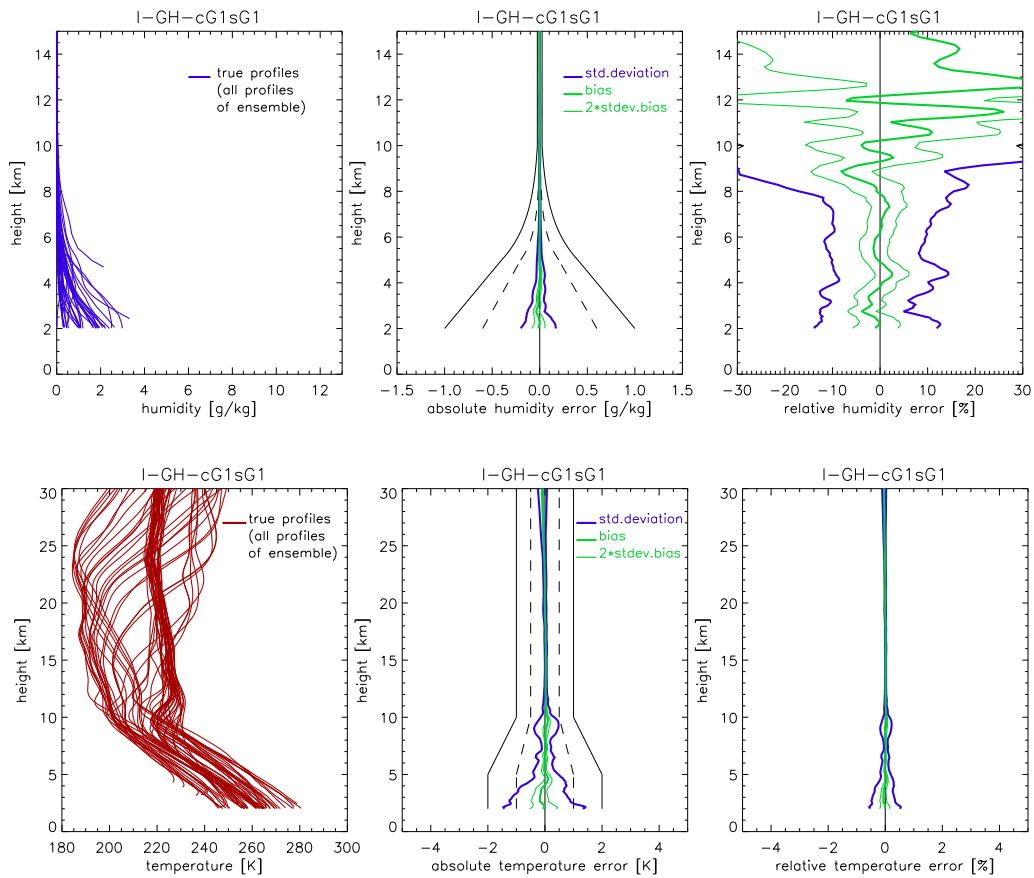


Figure 5.14: Humidity (upper row) and temperature (lower row) retrieval results for the high-latitude cloudy and turbulent air scenario. The layout is the same as in Fig. 5.12.

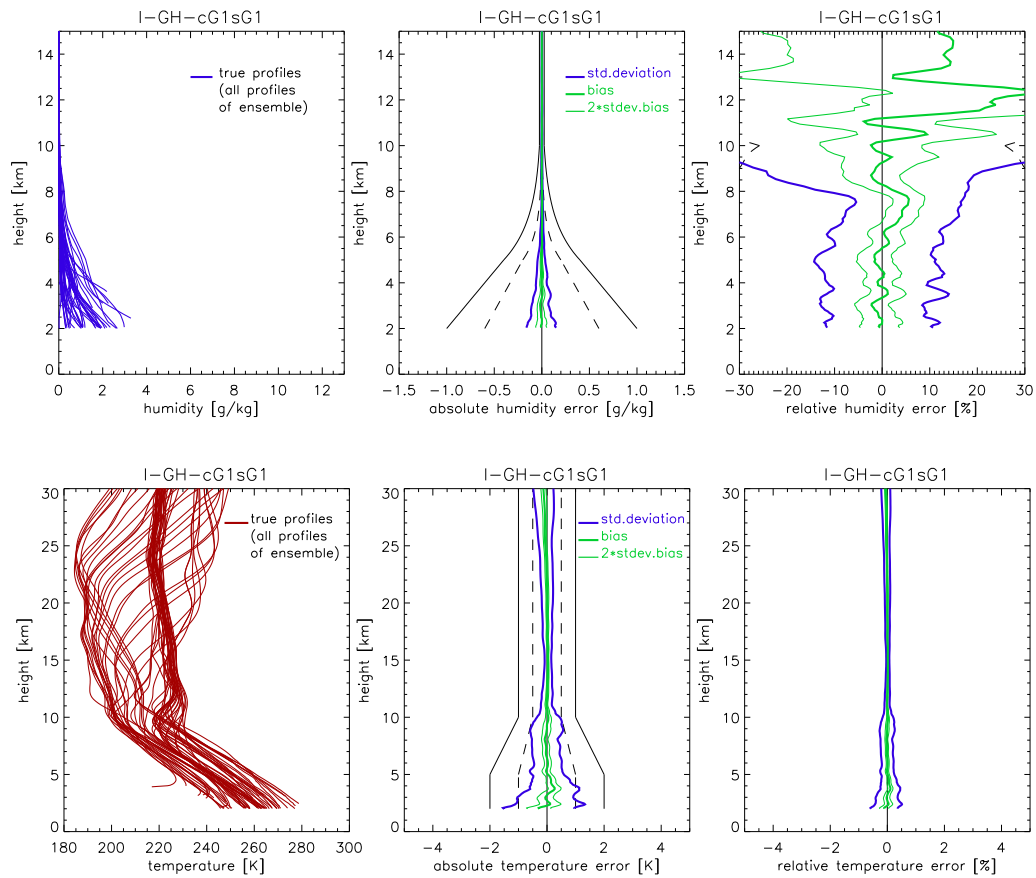


Figure 5.15: Humidity (upper row) and temperature (lower row) retrieval results for the high-latitude cloudy and turbulent air scenario with horizontal variability. The layout is the same as in Fig. 5.12.

## 5.2.2 Mid Latitudes

This subsection shows the retrieval performance within the mid-latitude band (30–60°N plus 30–60°S). The order of the scenarios is the same as in Subsection 5.2.1 above: Figure 5.16 shows the clear air results, followed by the cloudy air results (Fig. 5.17), the cloudy and turbulent air results (Fig. 5.18) and the cloudy and turbulent air results including horizontal variability (Fig. 5.19). Also the layout of the figures equals that of the preceding ones. Generally, all profiles meet the threshold requirements throughout the whole height range and the target requirements over extended domains and have no significant biases.

Looking at the humidity retrieval results, you can see that all four cases show about the same performance above approximately 10 km. In this height range, the errors are comparatively large but the RMS does not exceed the threshold requirements. A considerable part of these large errors is attributable to the not yet fully optimized retrieval chain as discussed in Subsection 5.2.1 above. Below 10 km, the performance is found to be not far off the target requirements and starts to meet them from about 8 km downwards, although the influence of turbulence and horizontal variability becomes visible. Cloud liquid water has no significant influence on the retrieval, which follows from the similarity of the clear and cloudy air results; for both scenarios, the errors lie within  $\pm 10\%$  from 2 km to 10 km. Turbulence, however, affects the humidity retrieval below about 6.5 km, which is why the errors in Figure 5.18 reach up to about 12% in the disturbed region. Furthermore, horizontal variability causes a widening of the errors at all heights beneath 10 km which becomes clear from comparison of Figures 5.18 and 5.19. They show that in case of horizontal variability, the errors amount to about 10% from 6.5 km to 10 km and reach up to about 15% below. As explained in Subsection 5.2.1, horizontal variability errors are “representativeness errors”, i.e., no direct part of the observational requirements.

The temperature performance reflects the same characteristics that have been drawn from the humidity results: Cloud liquid water has no influence on the performance, turbulence affects the retrieval from about 6.5 km downwards, and horizontal variability widens the errors from top to bottom. Except for the cloudy and turbulent air scenario including horizontal variability, the temperature errors are smaller than 0.25 K from around 11 km to 30 km and do not exceed 0.5 K between 6 km and 11 km. Beneath, the errors for the cloudy and turbulent air case are somewhat larger than those of the clear and cloudy air scenarios. Nevertheless, the errors lie around 1 K for all three scenarios. The cloudy and turbulent air case with horizontal variability also reaches the accuracy mentioned above.

Finally, the small “bump” which appears in all temperature profile standard deviations at approximately 10 km has the same origins as discussed in Subsection 5.2.1 above. The effect is a little smaller here because the humidity information contained within the imaginary refractivities of frequencies F1 and F2 near 10 km is higher at mid latitudes, since the humidity concentrations are generally higher. In

future, the weighting will be smoothly height dependent for all channels so that such residual features will vanish.

All in all, the performance of the retrieval in mid latitudes is well within the general ACE+ LEO-LEO observational requirements listed in Table 3.1. Above about 8 km, the humidity retrieval results meet the threshold requirements and below, they even meet the target requirements. The temperature results are consistent with the target requirements throughout the whole height range and if at all, they only exceed them a little and only at low heights.

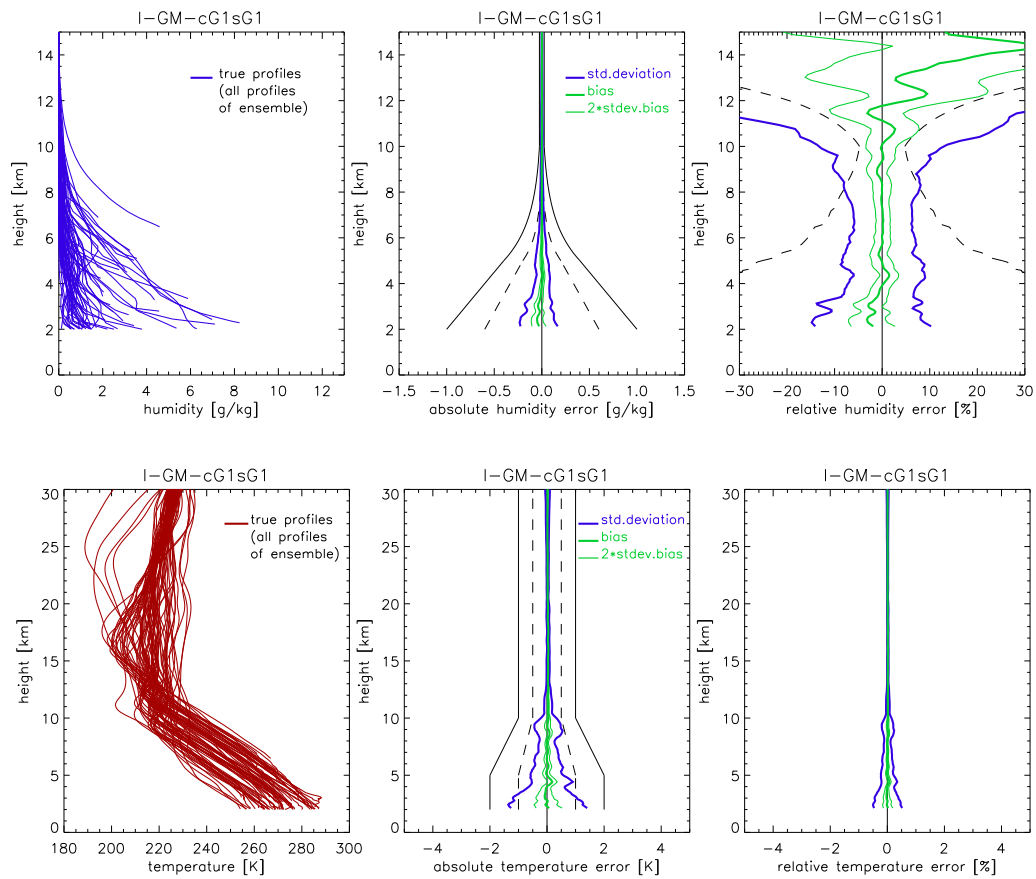


Figure 5.16: Humidity (upper row) and temperature (lower row) retrieval results for the mid-latitude clear air scenario. The layout is the same as in Fig. 5.12.

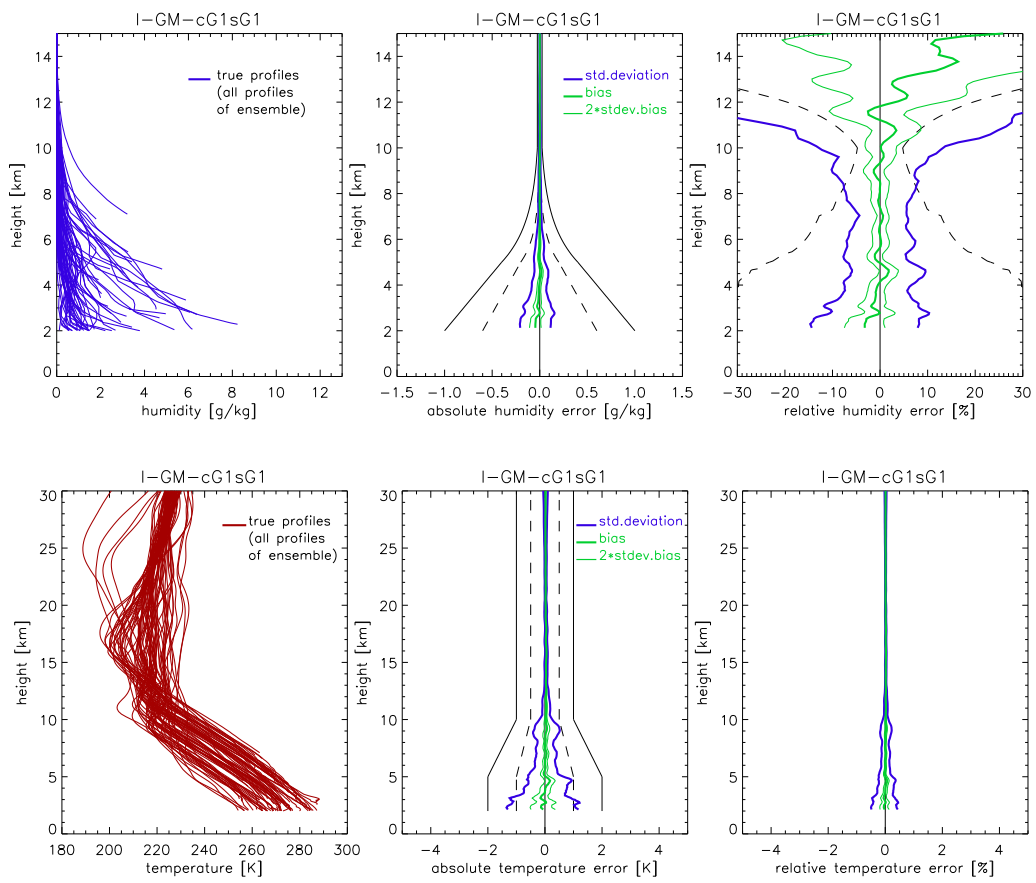


Figure 5.17: Humidity (upper row) and temperature (lower row) retrieval results for the mid-latitude cloudy air scenario. The layout is the same as in Fig. 5.12.

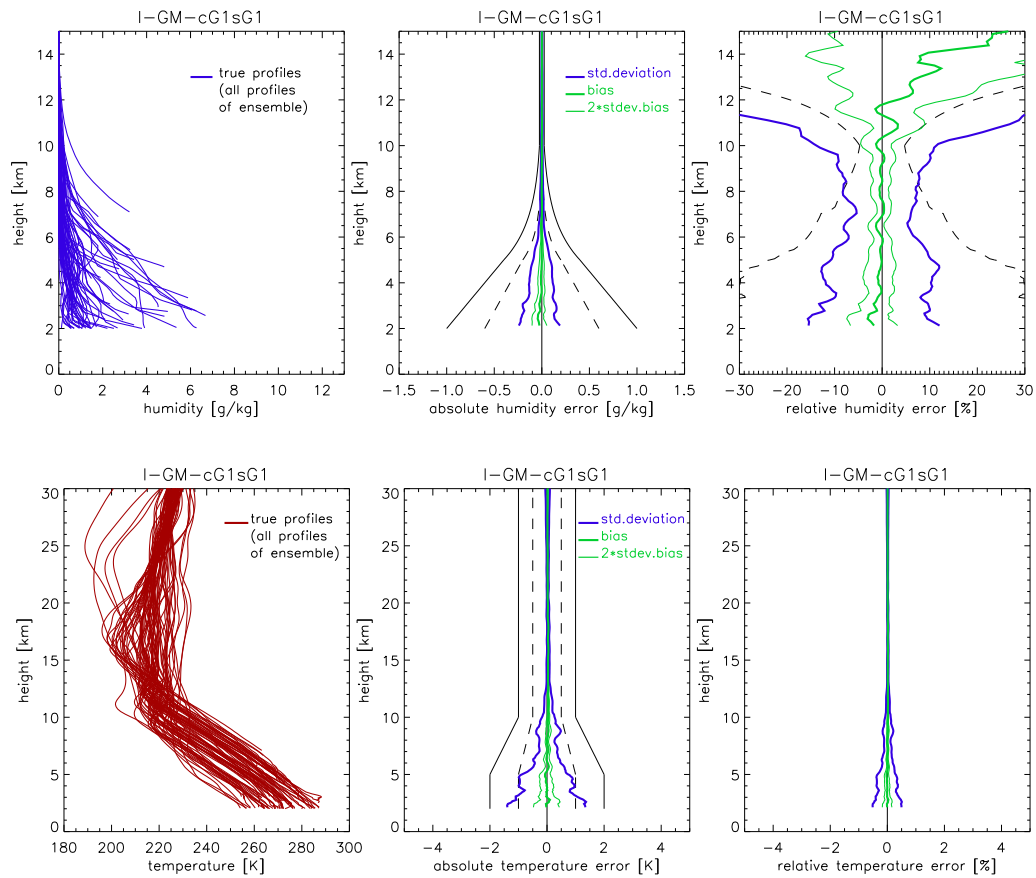


Figure 5.18: Humidity (upper row) and temperature (lower row) retrieval results for the mid-latitude cloudy and turbulent air scenario. The layout is the same as in Fig. 5.12.

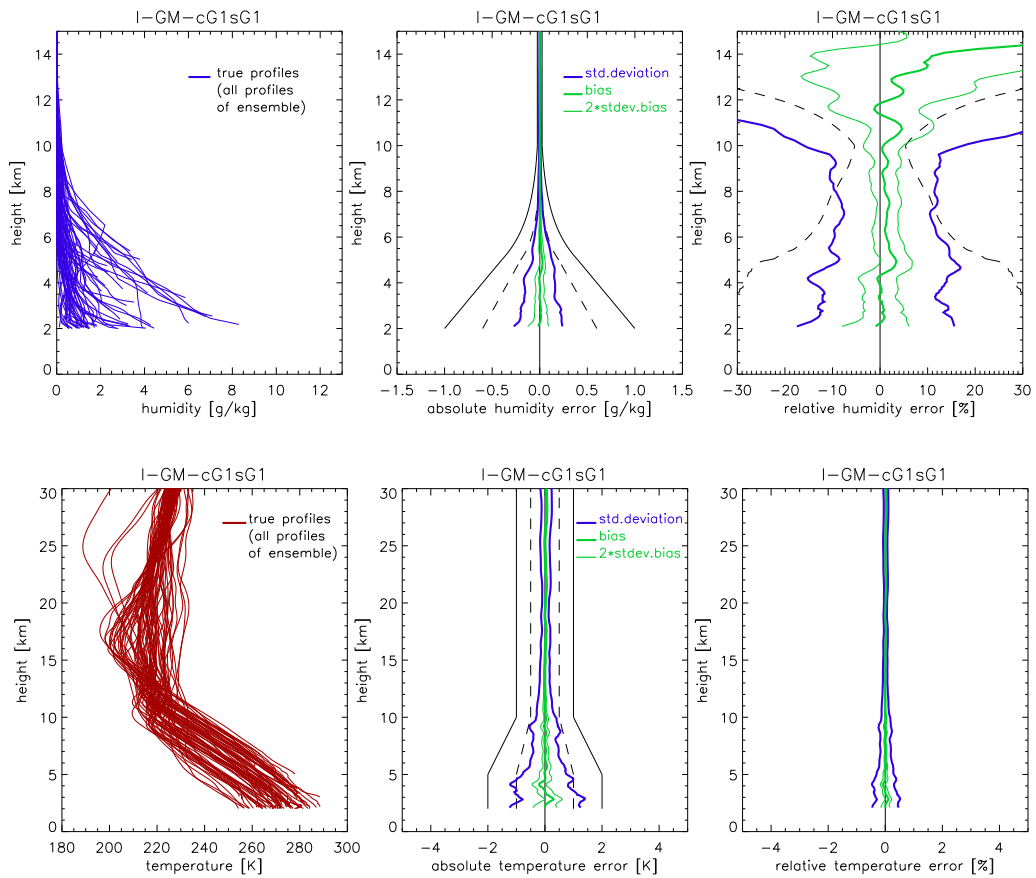


Figure 5.19: Humidity (upper row) and temperature (lower row) retrieval results for the mid-latitude cloudy and turbulent air scenario with horizontal variability. The layout is the same as in Fig. 5.12.

### 5.2.3 Low Latitudes

This subsection includes the temperature and humidity retrieval performance analysis results from the low-latitude band (30 °S to 30 °N). The clear air scenario is shown in Figure 5.20, followed by the cloudy air scenario (Fig. 5.21), the cloudy and turbulent air scenario (Fig. 5.22) and the scenario including horizontal variability (Fig. 5.23). The layout of the figures is the same as for the preceding figures. Generally, all profiles are consistent with the threshold requirements throughout the whole height range and with the target requirements in the lower troposphere. Furthermore, they have no significant biases.

Concerning the humidity retrieval, all three scenarios based on the assumption of spherical symmetry show roughly the same performance from top to bottom regardless of the atmospheric conditions. Above about 11 km the errors increase significantly, partly due to the humidity there and partly due to the not fully optimized retrieval chain as discussed in Subsection 5.2.1. Between about 7 km and 11 km, the errors are near 6%, and below, the RMS reaches up to about 8%. Below 3 km, the errors vary from scenario to scenario. This is due to the best-fit temperature extrapolation which is frequently activated even in the clear and cloudy air scenarios at a height of 3 km in order to deal with boundary layer effects (cf. the discussion on high humidities at heights < 3 km along with Fig. 5.1, Subsect. 5.1.1). Horizontal variability (cf. Fig. 5.23) causes a widening of the errors between approximately 2 km and 11 km and the RMS in this height range is nearly constant at 10%. Above, the errors are similar to those of the other three scenarios.

The performance of the temperature retrieval below approximately 10 km is about the same for all scenarios. From 10 to near 7.5 km, the errors lie below 0.5 K. Below 7.5 km, the errors rise and reach roughly 1 K at 5 km. The errors below stay at about the same level. Above 10 km, the errors are smaller than 0.25 K for all scenarios except the one that includes horizontal variability, where the errors are around 0.25 K. Finally, the “bumpy” feature at about 10 km, which appeared at high latitudes and mid latitudes (discussed in Subsects. 5.2.1 and 5.2.2), is almost invisible at the low-latitude band. This is because of the larger amount of water vapour in this region which leads, compared to mid-latitudes, to further increased humidity information content at frequencies F1 and F2 near 10 km.

In summary, the humidity and temperature retrieval performance at low latitudes is well within the ACE+ LEO-LEO observational requirements. The temperature results lie within the target requirements at nearly all heights and if at all, they exceed the target only marginally and mainly at low heights. The humidity performance meets the target requirements — which are very challenging to meet at low latitudes since formulated in terms of absolute humidity — throughout the lower troposphere only, but also is not far off the target above and lies well within the threshold requirements.

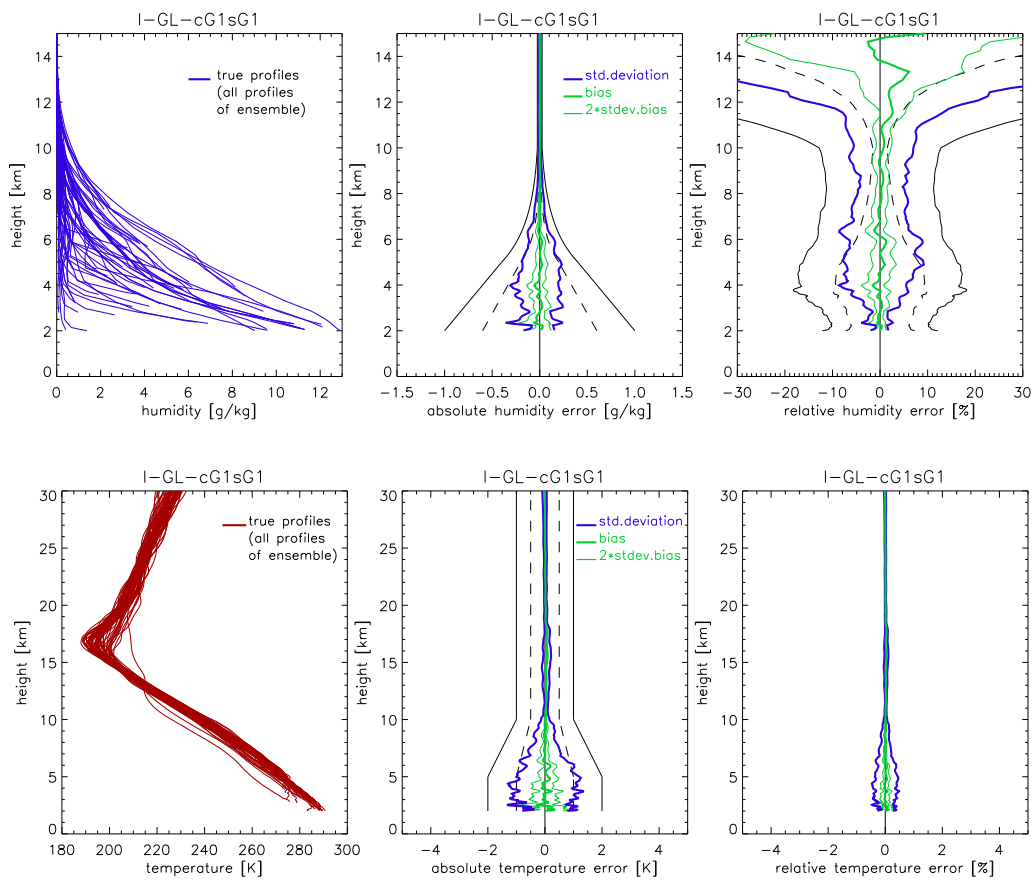


Figure 5.20: Humidity (upper row) and temperature (lower row) retrieval results for the low-latitude clear air scenario. The layout is the same as in Fig. 5.12.

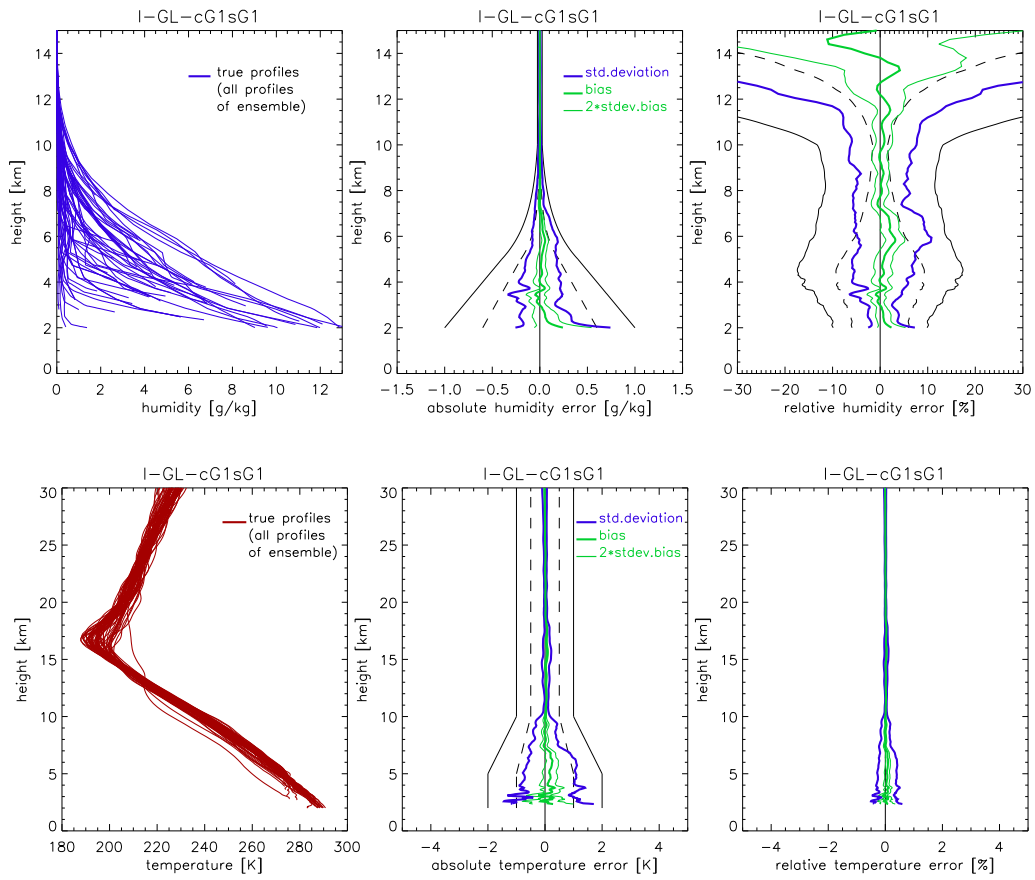


Figure 5.21: Humidity (upper row) and temperature (lower row) retrieval results for the low-latitude cloudy air scenario. The layout is the same as in Fig. 5.12.

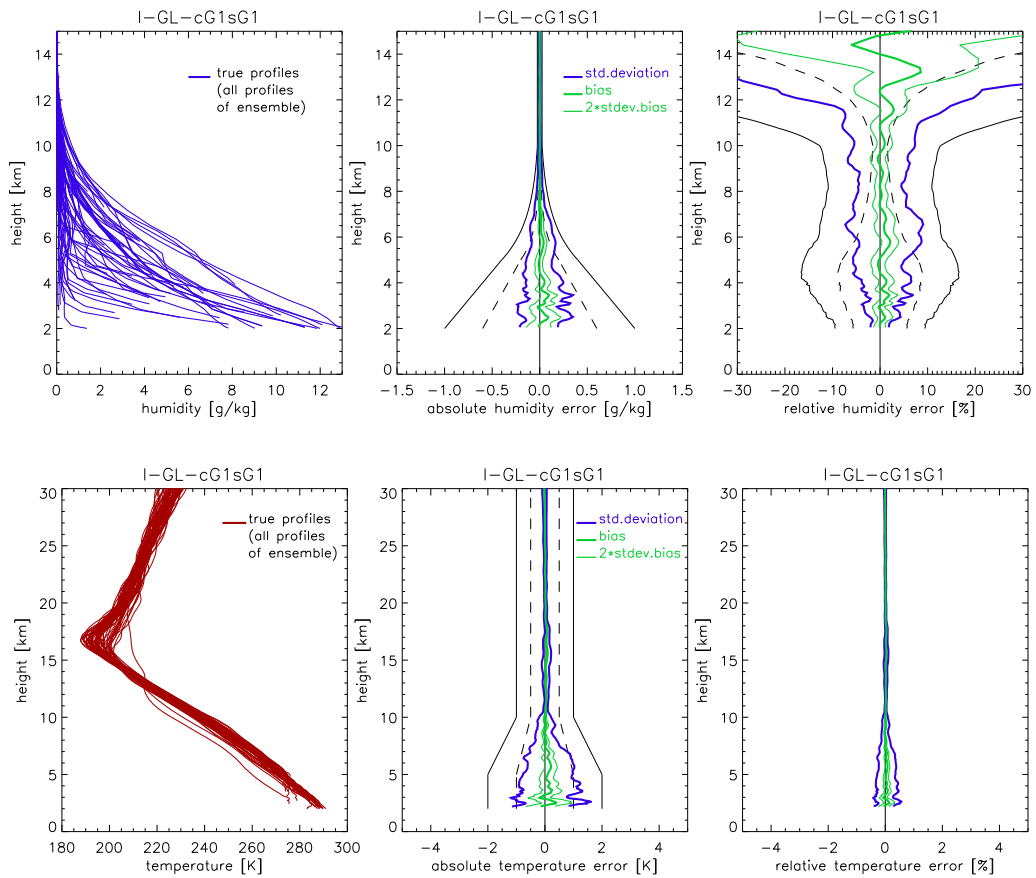


Figure 5.22: Humidity (upper row) and temperature (lower row) retrieval results for the low-latitude cloudy and turbulent air scenario. The layout is the same as in Fig. 5.12.

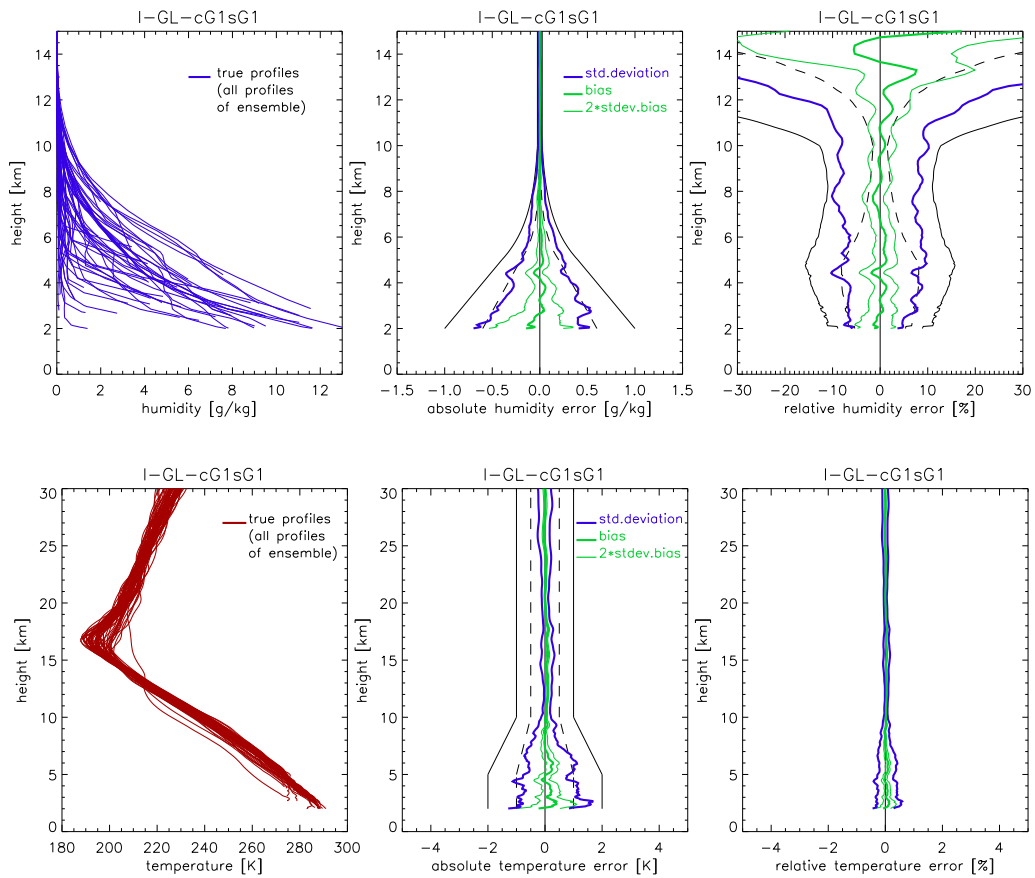


Figure 5.23: Humidity (upper row) and temperature (lower row) retrieval results for the low-latitude cloudy and turbulent air scenario with horizontal variability. The layout is the same as in Fig. 5.12.

### 5.2.4 Comparison of the Performance at Different Latitudes

This subsection provides a brief look at the similarities and differences of the performance results at different latitude bands. Generally, it turned out that clouds in terms of their liquid/ice water absorption have nearly no influence on the retrieval performance all over the world. At low latitudes, and to a minor degree also at mid and high latitudes, this behaviour can be attributed to the best-fit temperature extrapolation, which introduces a priori temperature information in order to stabilize the retrieval. Thus, accurate retrieval even in presence of heavily clouded and disturbed air is possible, though it somewhat affects the retrieval performance as do combinations of clouds and turbulences. This leads to the use of auxiliary information. The influence of turbulence is found largest at high latitudes. At mid latitudes, it is a bit smaller and at low latitudes, the effects of turbulence are strongly intermingled with cloud absorption effects and are thus not easily recognizable on their own. This performance behaviour is mainly due to different usage of temperature background information at the three latitude bands. The strong turbulence at low latitudes causes relatively more a priori temperature information to be used than the weaker turbulence at the mid- and high-latitude bands, which is why the effects of turbulence are compensated best at low latitudes — at the expense of using the highest degree of auxiliary temperature information. Favourably, the latter is most readily available in the thermally stable low latitude atmosphere.

Horizontal variability affects the retrieval at all latitudes and at all heights. Regarding specific humidity, the influence grows with the amount of water vapour since the general variability increases simultaneously. This is why the influence is smaller at upper heights than at lower heights (see also [Foelsche and Kirchengast, 2004a, b]). Accordingly, the transitional height between minor and larger influence is lower at high latitudes than at low latitudes. The temperature retrieval, however, is affected from some horizontal variability from top to bottom, because the temperature field reflects the general horizontal variability of the atmospheric mass field. See [Foelsche and Kirchengast, 2004a, b] and references therein for further details on horizontal variability effects.

The ratio of retrieved temperature error and best-fit temperature background error (averaged over all events belonging to a set) has been put into graphs (see Fig. 5.24) in order to illustrate the differences in the frequency of usage of additional temperature information in the three latitude bands and under various atmospheric conditions. For the sake of completeness, the same ratio for retrieved and a priori water vapour errors has been drawn, too. The error ratios  $r_k$  were computed at each height during the retrieval as follows:

$$r_k = \frac{\sqrt{S_{kk}}}{\sqrt{C_{bkk}}} = \frac{s_k}{\sigma_k}, \quad (5.1)$$

where  $\mathbf{S}$  is the retrieval error covariance matrix,

$$\mathbf{S} = \left( \mathbf{K}^T \mathbf{C}_y^{-1} \mathbf{K} + \mathbf{C}_b^{-1} \right)^{-1}, \quad (5.2)$$

with the Jacobian weighting matrix  $\mathbf{K}$ ,

$$\mathbf{K} = \left( K'^{\text{adj}}, K_j''^{\text{adj}} \right)^T, \quad (5.3)$$

the measurement (and forward modelling) error covariance matrix  $\mathbf{C}_y$ ,

$$\mathbf{C}_y = \text{Diag} \left( \sigma_{N'}^2, \sigma_{N''_j}^2 \right), \quad (5.4)$$

and the background (a priori) error covariance matrix  $\mathbf{C}_b$ ,

$$\mathbf{C}_b = \text{Diag} \left( \sigma_T^2, \sigma_e^2, \sigma_{lw}^2 \right). \quad (5.5)$$

$s_k = \sqrt{S_{kk}}$  is the standard deviation of the respective parameter.  $j$  is the frequency channel index (three frequencies in the case of ACE+),  $\sigma_{N'}$  and  $\sigma_{N''}$  are the a priori standard errors of real and imaginary refractivities, respectively, and  $\sigma_T$ ,  $\sigma_e$  and  $\sigma_{lw}$  are the a priori standard errors of temperature, total water vapor partial pressure, and cloud liquid water density.  $K'^{\text{adj}}$  contains the real refractivity Jacobians and  $K_j''^{\text{adj}}$  the imaginary refractivity Jacobians (for each frequency  $j$ ):

$$K'^{\text{adj}} = \left( \frac{\partial N'}{\partial T}, \frac{\partial N'}{\partial e}, \frac{\partial N'}{\partial lw} \right)^T, \quad (5.6)$$

$$K_j''^{\text{adj}} = \left( \frac{\partial N_j''}{\partial T}, \frac{\partial N_j''}{\partial e}, \frac{\partial N_j''}{\partial lw} \right)^T. \quad (5.7)$$

For more information on these quantities see the detailed algorithmic description of the retrieval by [Kirchengast et al., 2004b].

Figure 5.24 illustrates the ratio of retrieval error to background error for water vapour and temperature in all latitude bands for all four atmospheric scenarios. The two upper left panels show the behaviour in clear air, the upper right panels that in cloudy air, the lower left panels that in cloudy and turbulent air, and the lower right ones the behaviour in cloudy and turbulent air including horizontal variability. The green lines represent the high-latitude band, the orange lines the mid-latitude band and the red lines the low-latitude band. The blue line serves only as a reference and shows the ratio for the CIRA86aQ\_UoG clear air mid-latitude summer scenario analyzed using cloudy air retrieval including the possibility of

best-fit temperature extrapolation (see Fig. 5.11, third row). The retrieval based on this scenario is independent from background information from top to bottom, which means that best-fit temperature extrapolation has never been activated.

The error ratio demonstrates the dependence of the retrieval from background information. Error ratios below 0.1 imply that more or less all information stems from the measurement itself, and thus that the retrieval is independent from a priori knowledge. Ratios of more than 0.5, however, indicate that the majority of the information comes from background knowledge. Comparing the error ratios for temperature, we can see that background temperature knowledge enters from approximately 7 km downwards in all ECMWF based scenarios. But the intensity of the influence varies depending on the atmospheric conditions and on the latitude band. At low latitudes, a priori information is used already at higher altitudes than at high latitudes. And the influence of the background becomes important

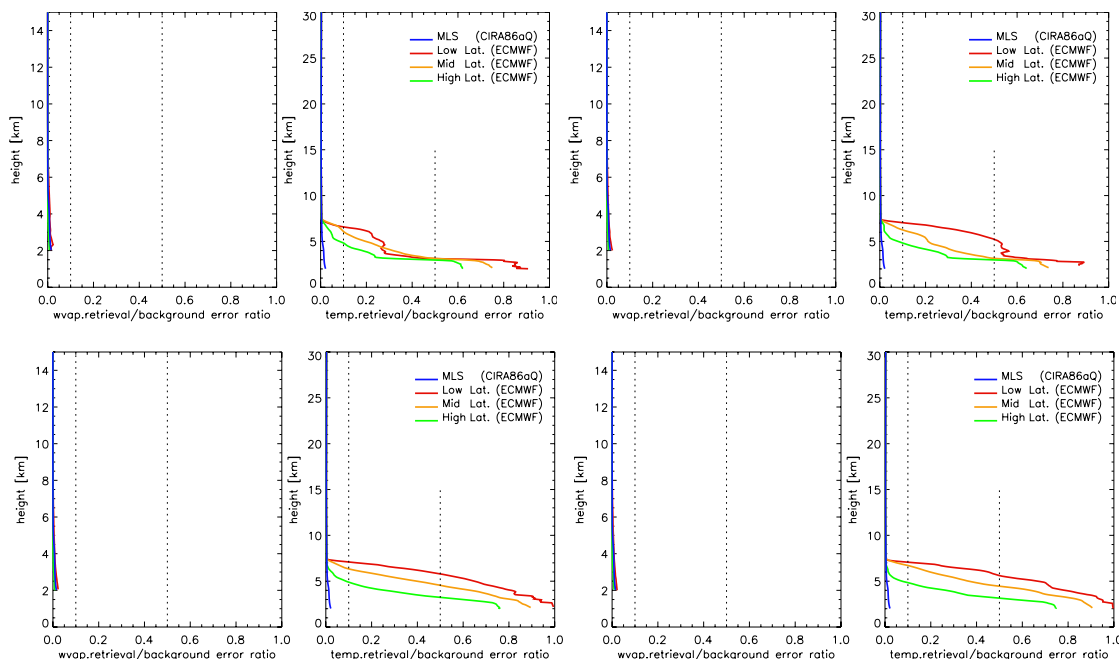


Figure 5.24: Retrieval error to background error ratios for retrieved water vapour and temperature profiles for the ECMWF based high-latitude (green), mid-latitude (orange) and low-latitude (red) scenario. The blue line serves as reference and represents the behaviour in the CIRA86aQ\_UoG clear air mid-latitude summer scenario. The conditions in clear air (the two upper left panels), cloudy air (upper right panels), cloudy and turbulent air (lower left panels), and cloudy and turbulent air including horizontal variability (lower right panels) are displayed. Baseline uncertainties in the BLUE algorithm were set to 100 K and 25 mbar for temperature and water vapour, respectively (mimicking “infinite” background uncertainties at all the heights where no background is to be used).

(ratio  $> 0.5$ ) earlier in the turbulent air scenarios than in the clear and cloudy air scenarios. Generally, a priori temperature information is used to a greater extent the more cloudy and disturbed the air is. This contributes to the good performance of temperature and humidity retrieval everywhere, even under severe cloudy and turbulent air conditions as they occur at low latitudes.

Considering the ratios of the water vapour retrieval error to the water vapour background error, you can see that background information of humidity has never been used. The small deviations from zero in the lower 5 km arise from an internal technical handling, which treats background-independent conditions for convenience by setting background uncertainties to extremely high (but still finite instead of infinite) values. At heights where additional temperature information is included, the humidity retrieval is mainly based on the information provided by real refractivity measurements and the background temperature. The search library for the temperature, a 24 h ECMWF forecast, has proven to be adequate, since neither humidity nor temperature retrieval have significant biases at heights where background information is used.

Finally, the error correlation coefficients  $c_k$  between water vapour and temperature at all latitudes under different atmospheric conditions shall be considered. They are displayed in Figure 5.25 (averaged over all events belonging to a set) and were computed at each height during the retrieval as follows:

$$c_{kl} = \frac{S_{kl}}{\sqrt{S_{kk} \cdot S_{ll}}}, \quad (5.8)$$

where again (as in Eq. 5.1) the elements of the retrieval error covariance matrix  $\mathbf{S}$  have been used — this time including the non-diagonal ones expressing inter-correlations between water vapour and temperature.

The error correlation coefficient is a measure for the interdependence of errors in two parameters. As can be seen, the error correlation between water vapour and temperature is slightly positive from top to bottom. This means that there will be a slight tendency to overestimate the humidity if the temperature is overestimated. This correlation arrives due to the hydrostatic equation being linked to the equation of state and the equation of virtual temperature, which are applied during the retrieval (cf. Subsect. 2.2.3). Since the retrieval results are unbiased (as shown earlier in this chapter), however, this inter-correlation of the statistical errors on water vapour and temperature is more of academic than practical interest, in particular for climatological purposes. In numbers, the error correlation is very small at a level of 0.2 down to the mid-to-lower troposphere.

In the mid-to-lower troposphere below 8 km, rooting in the physical equations involved in the retrieval, the inter-correlation is stronger the greater the amount of water vapour in the atmosphere is. This is instructively seen in comparing the low- with the high-latitude results in Figure 5.25: At high latitudes, inter-correlation coefficients are  $< 0.5$  in all cases down to 2 km while at low latitudes they reach

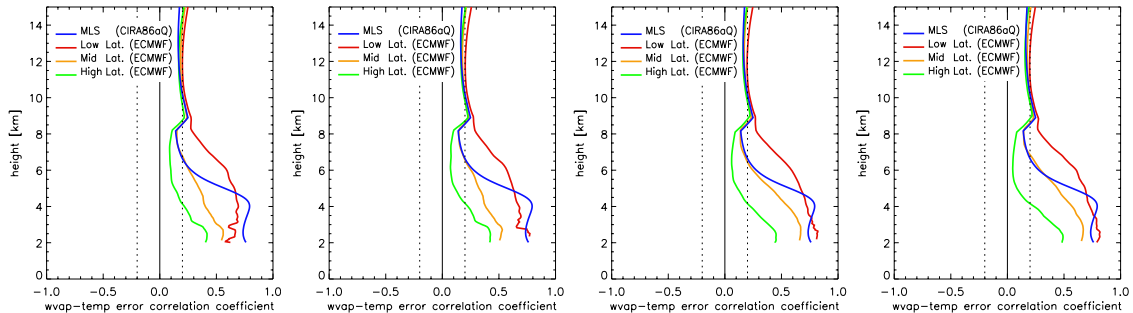


Figure 5.25: Error correlation coefficients between retrieved water vapour and temperature profiles for the ECMWF based high-latitude (green), mid-latitude (orange) and low-latitude (red) scenario. The blue line serves for reference and represents the behaviour in the CIRA86aQ\_UoG clear air mid-latitude summer scenario. Displayed are the conditions in clear air (left panel), cloudy air (second panel), cloudy and turbulent air (third panel) and cloudy and turbulent air including horizontal variability (right panel).

up to 0.8. Regarding weather rather than climate application of the data, such as use in NWP data assimilation systems, one might think of the need to include the inter-correlations below about 7km into the relevant observation error covariance matrices. Also this aspect is fairly academic, however, since in practice NWP systems will generally prefer to assimilate real and imaginary refractivity profiles directly, where no inter-parameter error correlations exist.

The correlation is also essentially independent on whether temperature background information is used or not, as the similarity of the different panels of Figure 5.25 shows.

All in all, humidity and temperature retrieval results are nearly unbiased and meet the ACE+ observational requirements [ESA, 2004c] at all latitude bands. The temperature results lie within the target requirements and the humidity results lie also within target or generally not far from the target requirements. The data would be of high utility for both climate and weather applications.

# Summary, Conclusions and Outlook

The analysis carried out within the scope of this work showed that the performance of the humidity and temperature retrieval readily meets the threshold requirements laid down in the ACE+ Mission Requirements Document (cf. [ESA, 2004c], Sect. 3.5) regardless of the atmospheric conditions and the geographical location of the occultation event. The temperature results lie even within the target requirements at nearly all heights, as do the humidity retrieval results below about 5–9 km. Furthermore, the retrieved profiles are essentially free from biases, which is due to the self-calibrating nature of the radio occultation technique (cf. Sect. 2.2).

Nevertheless, improvements are needed; in particular at upper heights where the amount of water vapour is low. There, the current retrieval scheme is affected, among other things, by the not yet fully optimized filtering and weighting of the information contained in the transmissions and imaginary refractivities of the three ACE+ frequencies. This contributes considerably to a weakness of the humidity retrieval above about 8–12 km and of the temperature around 10 km. The weighting is non-trivial because of the low humidity at upper heights and its latitude-dependent variability.

In order to allow for an accurate retrieval in the dry high latitude regions, frequencies that are more sensitive to water vapour are needed compared to those for the humid lower latitudes. Therefore, latitudinal dependent weighting in addition to a more skillful height dependent weighting of the information contained within the three ACE+ frequencies will produce further improved results in both dry and humid regions.

Favourably, clouds in terms of their additional liquid water absorption turned out to have a small influence on the temperature and humidity retrieval performance. Furthermore, the retrieval is essentially insensitive to ice clouds, i.e., temperature and humidity profiles can be sensed through ice clouds. Regarding the increased atmospheric turbulence in (thick water) clouds, this is expected to have significant influence and may lead to activation of best-fit temperature extrapolation (Subsect. 4.3, p. 72) in the current setup. A more rigorous study of turbulence requires

high-resolution wave-optical simulations, which was beyond the scope of this study. Recent results to this end indicate that use of wave-optics preprocessed differential transmission profiles is a promising approach in presence of turbulence [Gorbunov and Kirchengast, 2004]. Further studies in this direction will be useful.

Rain affects the retrieval with similar significance as turbulence and forces the best-fit temperature extrapolation to be activated, in general below 3 km only. This extrapolation yields a priori information on temperature in regions where the absorption of the signal is so large or so oscillatory that the information included in the imaginary refractivity is practically of no use for atmospheric profiles retrieval. That way, the retrieval is facilitated and accurate results are still possible. In that case, the results are based on the information contained within the real refractivity and the selected temperature profile.

Below about 3–7 km, turbulence affects the retrieval more or less depending on its strength. But the effects thereof are limited, which is mainly due to the best-fit temperature extrapolation. In most cases, the influence of turbulence is hardly recognizable in the results. The effects of horizontal variability, on the other hand, are mostly easier to spot. It uniformly affects the performance of temperature regardless of height or latitude, whereas humidity is influenced less at high latitudes than at low latitudes. This is because the horizontal variations are less strong at high latitudes than at lower ones, which is closely connected to the higher water vapour content of air at lower latitudes. Nevertheless, the retrieval performance is compliant with the observational requirements even if horizontal variability is included. Moreover, in practice adequate use of the observations would account for the along-ray averaged nature of the data.

In summary, the retrieval system has proven to be mature for the evaluation of radio occultation data even under quite realistic conditions, as the simulations based on the ECMWF analysis field (including clouds and turbulence) indicate. Nevertheless, further retrieval system improvements are needed, some of which have been noted above. The results of the performance analysis show that ACE+ can be expected to fulfill the scientific objectives laid down in the ACE+ Mission Requirements Document [ESA, 2004c]. The ACE+ LEO-LEO radio occultation system can be expected to deliver accurate and consistent measurements of humidity, temperature, and pressure as a function of height. In the upper and middle troposphere and above, the retrieval of the parameters will be independent of a priori knowledge, which is a great advantage over the GNSS-LEO radio occultation technique. In the lower troposphere below about 3–7 km a priori information of temperature will be used under adverse atmospheric conditions. All in all, the database provided by the ACE+ mission will be of great importance for atmosphere and climate science.

# Appendix A

## Sample EGOPS Input Files

### A.1 ACE+ Constellation Two Line Element (TLE) Files

#### ACE+ Transmitter (Tx) Satellites

```
ACE+TX1-800km          H1          betalim = 10.0
1      1  99003USR 99001.00000000 .00000000 00000-0 00000-0 0 0010
2      1  98.6300 243.6000 0001000 90.0000  0.0000 14.31502844  0
ACE+TX2-800km          H2          betalim = 10.0
1      1  99004USR 99001.00000000 .00000000 00000-0 00000-0 0 0010
2      1  98.6300 243.6000 0001000 90.0000 180.0000 14.31502844  0
```

#### ACE+ Receiver (Rx) Satellites

```
ACE+RX1-650km          L1          betalim = 10.0
1      1  99001USR 99001.00000000 .00000000 00000-0 00000-0 0 0010
2      1  97.9500 63.6000 0001000 90.0000  0.0000 14.74733736  0
ACE+RX2-650km          L2          betalim = 10.0
1      1  99002USR 99001.00000000 .00000000 00000-0 00000-0 0 0010
2      1  97.9500 63.6000 0001000 90.0000  80.0000 14.74733736  0
```

### A.2 Mission Analysis/Planning Input File

```
[*Project-Id and Task-Id*]
EGOPS Input File Version = 5.0.3
Creation Date & Time      = 2004-04-20 03:31:00
```

```

Task-Type           = MAnP1
Project-Id         = SDECMWF2
Task-Id           = M-GCM1

[*Data Type Selection*]
Data Type         = LEO-LEO Occultation Data

[*UT Range*]
Start_Time        = 020915.000000 [yyymmdd.hhmmss]
Simul_Time_Range = 0240000 [hhmmss]

[*Height Levels*]
Hlo1 Hhi1 HStep1 dh1 = 1.0 12.0 1.0 0.10 [km]
Hlo2 Hhi2 HStep2 dh2 = 12.0 30.0 2.0 0.20 [km]
Hlo3 Hhi3 HStep3 dh3 = 30.0 80.0 10.0 1.00 [km]

[*Geographic Area of Interest*]
GeogrAreaChoice   = Global

[*Earth Figure Model*]
EarthFigModelChoice = Ellip.WGS84

[*Tx-to-Rx Ray Treatment*]
RayTreatmentChoice = Bended Rays (Exp. Atmos.)

[*Tx System and Orbit Specifications*]
Tx SatSystemChoice = ACE+
Tx OrbitModelChoice = SGP Orbits (Impr. Kepler)
Tx1 OrbitElemFilename = Tx-ACE-Plus_1999001.tle

[*Tx Antennae Specifications*]
Tx -V AntennaChoice = Used
Tx -V BoresightElevation = 27.0 [deg]
Tx -V BoresightAzimuth = 180.0 [deg]
Tx -V FOVChoice = Ell_Cartes
Tx -V TPBW Vertical = 10.0 [deg]
Tx -V TPBW Horizontal = 90.0 [deg]
Tx +V AntennaChoice = Used
Tx +V BoresightElevation = 27.0 [deg]
Tx +V BoresightAzimuth = 0.0 [deg]
Tx +V FOVChoice = Ell_Cartes
Tx +V TPBW Vertical = 10.0 [deg]
Tx +V TPBW Horizontal = 90.0 [deg]

[*Rx System and Orbit Specifications*]
Rx SatSystemChoice = ACE+
Rx OrbitModelChoice = SGP Orbits (Impr. Kepler)

```

```
Rx OrbitElemFilename      = Rx-ACE-Plus_1999001.tle
```

```
[*Rx Antennae Specifications*]
```

```
Rx -V AntennaChoice       = Used
Rx -V BoresightElevation  = 27.0 [deg]
Rx -V BoresightAzimuth    = 180.0 [deg]
Rx -V FOVChoice           = Ell_Cartes
Rx -V TPBW Vertical       = 10.0 [deg]
Rx -V TPBW Horizontal     = 90.0 [deg]
Rx +V AntennaChoice       = Used
Rx +V BoresightElevation  = 27.0 [deg]
Rx +V BoresightAzimuth    = 0.0 [deg]
Rx +V FOVChoice           = Ell_Cartes
Rx +V TPBW Vertical       = 10.0 [deg]
Rx +V TPBW Horizontal     = 90.0 [deg]
```

```
[*Visibility Infos on Differencing*]
```

```
DiffVisInfChoice         = No_Diff_Vis_info
TrackVisInfChoice        = No_Track_Vis_info
```

```
[* EOF *]
```

## A.3 Forward Modeling Input File

```
[*Project-Id and Task-Id*]
```

```
EGOPS Input File Version = 5.0.3
Creation Date & Time     = 1999-07-22 23:45:49
Task-Type                = FoMod
Project-Id               = WP41-Perf1-DA
Task-Id                  = F-C2-cAs1sML1
```

```
[*Occ. Event Simulation Type/Specifications*]
```

```
OccEventSimulType       = Single Event/Ideal Geometry
OccEv.HeightRange       = 1.0 80.0 [km]
TangPointLoc (Lat Lon)  = 40.0 0.0 [deg]
AziOccPlane (N over W)  = 0 [deg]
EventStart Date/Time    = 030715.120000 [yymmdd.hhmmss]
SatHeights (hRx hTx)   = 650 800 [km]
```

```
[*Tx Channels and FoMod Sampling Rate Specification*]
```

```
Tx ChannelSetChoice     = ACE+ Standard (NChan= 3 F1-F3)
FoMod Sampling Rate     = 10.0 [Hz]
```

```
[*Atmospheric Models Choice/Specifications*]
```

```
AtmModelChoice          = HLat 2D Atmosphere (CIRA86aQ_UoG)
```

```

AtmModelStructureChoice = Sph. Symmetry (no horizontal var.)
HumidityChoice          = Humidity included (moist air)
CloudsandRainChoice     = Simple Clouds+Rain
CloudsRainType          = 3D As-Altostratus (LWC)
LWCloud WaterContent    = 0.20 [g/m3]
LWCloud Height Thickness = 4.5 0.6 [km]
Cloud RefLocationLatLon = 40.00 0.00 [deg]
Cloud LatWidth LonWidth = 200.0 200.0 [km]
AtmDistModelChoice      = Turbulence/Scintillations superposed
TurbReferenceHeight     = 0.0 [km]
Turb_Cn2_RefHeight      = 1.30E-15 [m-(2/3)]
TurbVerticalStructure   = Exponential
TurbVerticalScale       = 2.0 [km]
TurbHorizontalExtend    = 200.0 [km]

```

[\*Ionospheric Models Choice/Specifications\*]

```

IonModelChoice          = No Ionosphere

```

[\*Signal Propagation Simulator Specifications\*]

```

PropSimulatorType      = Full-3D Ray Tracer
PropSimulatorAccuracy  = < ~1 mm
Extended Data Output   = Dopp-Tran-Bend-pLC1 Data

```

[\*Earth Figure Model\*]

```

EarthFigModelChoice    = Spherical

```

[\* EOF \*]

## A.4 Observation System Modeling Input File

[\*Project-Id and Task-Id\*]

```

EGOPS Input File Version = 5.0.3
Creation Date & Time     = 2004-07-22 23:45:49
Task-Type                = OSMod
Project-Id               = WP41-Perf1-DA
Task-Id                  = 0-C2-cAs1sML1-in1

```

[\*Occ. Event Simulation Type/Specifications\*]

```

OccEventSimulType       = Single Event/Ideal Geometry
OccEv.HeightRange       = 1.0 80.0 [km]
ReferenceFoMod/Task-Id = F-C2-cAs1sML1
OccNoRange               = 1 1 0

```

[\*Tx Channels and Rx Sampling Rate Specification\*]

```

Tx ChannelSetChoice     = ACE+ Standard (NChan= 3 F1-F3)

```

```
Rx Sampling Rate          = 10.0 [Hz]

[*POD Error Modeling/Specifications*]
PODErrorModelChoice      = No POD Errors

[*Tx-Rx System Simulator Specifications*]
TxRx SysSimulatorType    = Parameterized Receiving System Simulator
Extended Data Output     = C/NO and Antenna Data

[*Tx Antennae Specifications*]
Tx -V AntennaChoice      = Used
Tx -V BoresightElevation = 27.0 [deg]
Tx -V BoresightAzimuth   = 180.0 [deg]
Tx -V FOVChoice          = Ell_Cartes
Tx -V HPBW Vertical      = 90.0 [deg]
Tx -V HPBW Horizontal    = 90.0 [deg]
Tx -V AntGain/Boresight  = 24.8 [dB]
Tx -V BoresightTracking  = Yes
Tx +V AntennaChoice      = Used
Tx +V BoresightElevation = 27.0 [deg]
Tx +V BoresightAzimuth   = 0.0 [deg]
Tx +V FOVChoice          = Ell_Cartes
Tx +V HPBW Vertical      = 90.0 [deg]
Tx +V HPBW Horizontal    = 90.0 [deg]
Tx +V AntGain/Boresight  = 24.8 [dB]
Tx +V BoresightTracking  = Yes

[*Tx Performance Modeling*]
TxPerformModelChoice     = No Transmitter Perf. Model

[*Rx Antennae Specifications*]
Rx -V AntennaChoice      = Used
Rx -V BoresightElevation = 27.0 [deg]
Rx -V BoresightAzimuth   = 180.0 [deg]
Rx -V FOVChoice          = Ell_Cartes
Rx -V HPBW Vertical      = 10.0 [deg]
Rx -V HPBW Horizontal    = 40.0 [deg]
Rx -V AntGain/Boresight  = 24.8 [dB]
Rx -V BoresightTracking  = Yes
Rx +V AntennaChoice      = Not Used

[*Rx Performance Modeling*]
RxThermNoiseModelChoice = LEO-LEO Thermal Noise Model
ChannelsC/NOAdjustment  = -2.60 -1.90 -1.10 [dBHz]
AntennaNoiseTemp10GHz   = 80.0 [K]
ReceiverNoiseTemp10GHz  = 160.0 [K]
Rx1/fNoiseModelChoice   = 1/f Amplitude Noise Model
```

```

1/fReferenceHeight      = 25.0 [km]
PeriodInterval TMin TMax = 1.00 20.00 [sec]
ErrorSlopePeriodDomain = 0.050 [dB/min]
RxPolyAmplDriftModel   = Polynomial Ampl. Drift Model
DriftApplicationType    = Apply drifts randomly (as rms)
PolyReferenceHeight     = 25.0 [km]
LinearDriftSlope        = 0.060 [dB/min]
QuadrDriftCurvature    = 0.0000 [dB/min2]
3rdOrderDriftCurvChange = 0.00000 [dB/min3]
RxSinAmplDriftModel    = No Sinusoidal Ampl. Drifts

[*Local Multipath Modeling*]
LocalMultipathModelChoice = No Local Multipath

[*Differencing Treatment/Clocks Modeling*]
DiffTreatClocksChoice    = Perfect Clocks (No Differencing)

[*Atmospheric Models Choice/Specifications*]
AtmModelChoice           = HLat 2D Atmosphere (CIRA86aQ_UoG)
AtmModelStructureChoice  = Sph. Symmetry (no horizontal var.)
HumidityChoice           = Humidity included (moist air)
CloudsandRainChoice      = Simple Clouds+Rain
CloudsRainType           = 3D As-Altostratus (LWC)
LWCloud WaterContent     = 0.20 [g/m3]
LWCloud Height Thickness = 4.5 0.6 [km]
Cloud RefLocationLatLon  = 40.00 0.00 [deg]
Cloud LatWidth LonWidth  = 200.0 200.0 [km]
AtmDistModelChoice       = Turbulence/Scintillations superposed
TurbReferenceHeight      = 0.0 [km]
Turb_Cn2_RefHeight       = 1.30E-15 [m-(2/3)]
TurbVerticalStructure    = Exponential
TurbVerticalScale        = 2.0 [km]
TurbHorizontalExtend     = 200.0 [km]

[*Ionospheric Models Choice/Specifications*]
IonModelChoice           = No Ionosphere

[*Earth Figure Model*]
EarthFigModelChoice      = Spherical

[* EOF *]

```

## A.5 Inversion/Retrieval Input File

```

[*Project-Id and Task-Id*]

```

```

EGOPS Input File Version = 5.0.3
Creation Date & Time      = 2004-04-09 19:15:00
Task-Type                = InRet
Project-Id               = WP41-Perf1-DA
Task-Id                  = I-C2-cAs1sML1-in1-c1

```

```
[*Occ. Event Type/Specifications*]
```

```

OccDataType              = SimData
OccEventType             = Single Event/Ideal Geometry
OccNoRange               =      1      1      0
OccEv.HeightRange       =      1.0  80.0 [km]
ReferenceOSMod/Task-Id  = 0-C2-cAs1sML1-in1

```

```
[*Tx Channels and Rx Sampling Rate Specification*]
```

```

Tx ChannelSetChoice     = ACE+ Standard (NChan= 3 F1-F3)
Rx Sampling Rate        =      10.0 [Hz]

```

```
[*Bending Angle and Transmission Retrieval Specifications*]
```

```

BendAngleRetToolChoice  = Advanced Geom.Optics Bend.Angle Retrieval
IonoCorrectionType      = Phase Correction
StatOptimizationType    = Optimize invoking MSIS90_DMI
TransmRetToolChoice     = Standard Channel Transmission Retrieval
I/IO RefHeightperChannel = 25.0 25.0 25.0 [km]
IOValue AvHeightInterval = 4.0 [km]

```

```
[*Refractivity Profiles Retrieval Specifications*]
```

```
RefProfRetToolChoice    = Abel Transform Complex Refr.Profiles Retrieval
```

```
[*Atmospheric Profiles Retrieval Specifications*]
```

```

AtmProfRetToolChoice    = Complex Refr.Based Atmos. Profiles
ComplRefrInvRetType     = T,q,e,p,rho,w by Opt.Inverse Estimation
RealRefrErrorModelChoice = 1/z (<zRef) + exp(z) (>zRef) Errors
RealRefrRMSError_zRef   = 0.10 [%] (zRef: 15 km)
ImagRefrErrorModelChoice = fac*dNi(z0)*W(z) SNR-based Errors
ImagRefrRMSError_spec  = 1.00 [1] (scale factor)
AtmProfRetrievalMode    = p+T+q+w (cloudy air) Retrieval
AtmBackgroundMode      = Best-fit T at z < zBestfitTop
AtmModelfBestFit        = HLat 2D Atmosphere (CIRA86aQ_UoG)

```

```
[*Atmospheric Models Choice/Specifications*]
```

```

AtmModelChoice          = HLat 2D Atmosphere (CIRA86aQ_UoG)
AtmModelStructureChoice = Sph. Symmetry (no horizontal var.)
HumidityChoice          = Humidity included (moist air)
CloudsandRainChoice     = Simple Clouds+Rain
CloudsRainType          = 3D As-Altostratus (LWC)
LWCloud WaterContent    = 0.20 [g/m3]
LWCloud Height Thickness = 4.5 0.6 [km]

```

```
Cloud RefLocationLatLon = 40.00 0.00 [deg]
Cloud LatWidth LonWidth = 200.0 200.0 [km]
AtmDistModelChoice = Turbulence/Scintillations superposed
TurbReferenceHeight = 0.0 [km]
Turb_Cn2_RefHeight = 1.30E-15 [m-(2/3)]
TurbVerticalStructure = Exponential
TurbVerticalScale = 2.0 [km]
TurbHorizontalExtend = 200.0 [km]
```

```
[*Ionospheric Models Choice/Specifications*]
```

```
IonModelChoice = No Ionosphere
```

```
[*Earth Figure Model*]
```

```
EarthFigModelChoice = Spherical
```

```
[* EOF *]
```

# List of Acronyms

- ACE ... Atmosphere and Climate Experiment
- ACE+ ... Atmosphere and Climate Explorer
- ACEPASS ... ACE+ Phase A Scientific Support
- ACliSCoPE ... Atmosphere and Climate Sensors Constellation Performance Explorer
- APM ... Atmospheric Profiling Mission
- ATOMS ... Active Tropospheric Ozone and Moisture Sounder
- BLUE ... Best Linear Unbiased Estimation
- $C/N_0$  ... Carrier-to-noise density ratio
- CDAE ... Command and Data Acquisition Element
- CHAMP ... Challenging Minisatellite Payload
- CIRA-86 ... COSPAR International Reference Atmosphere-86
- CIRA86aQ-UoG ... Moist air global climatological model, developed at the University of Graz
- CNES ... Centre National d'Etudes Spatiales (French space agency)
- CONAE ... Comisión Nacional de Actividades Espaciales
- COSMIC ... Constellation Observing System for Meteorology, Ionosphere and Climate
- COSPAR ... Committee on Space Research
- DLR ... Deutsches Zentrum für Luft- und Raumfahrt (German space agency)
- DMI ... Danish Meteorological Institute

- ECMWF ... European Centre for Medium-Range Weather Forecasts
- EGOPS4 ... End-to-end GNSS Occultation Performance Simulator, Version 4
- EGOPS5 ... End-to-end Generic Occultation Performance Simulator, Version 5
- EPS ... EUMETSAT Polar System
- ESA ... European Space Agency
- ESSP ... Earth System Science Pathfinder (NASA program)
- ESTEC ... European Space Research and Technology Centre
- EUMETSAT ... European Organisation for the Exploitation of Meteorological Satellites
- FAA ... Federal Aviation Administration
- FoMod ... Forward Modeling
- GALILEO ... European Satellite Navigation System
- GCM ... Global Circulation Model
- GFZ ... Geoforschungszentrum Potsdam (Germany)
- GGI ... GPS Geoscience Instrument
- GLONASS ... Russian Global Navigation Satellite System
- GMT ... Greenwich Mean Time
- GNSS ... Global Navigation Satellite System (GPS, GLONASS, and GALILEO together)
- GPS ... U.S. Global Positioning System
- GPS/MET ... GPS Meteorology
- GPSOS ... Global Positioning System Occultation Sensor (developed by SAAB Ericsson)
- GRACE ... Gravity Recovery And Climate Experiment
- GRAS ... GNSS Receiver for Atmospheric Sounding (developed by SAAB Ericsson)
- IDL ... Interactive Data Language

- IEP ... Institute of Environmental Physics, University of Bremen
- IGAM ... Institute for Geophysics, Astrophysics and Meteorology (University of Graz, Austria)
- IGOR ... Integrated GPS Occultation Receiver (improvement of the TRSR Black Jack)
- IGS ... International GPS Science for Geodesy
- IIP ... Instrument Incubator Program
- InRet ... Inversion/Retrieval
- IPCC ... Intergovernmental Panel on Climate Change
- JPL ... Jet Propulsion Laboratory (Pasadena, California)
- LEO ... Low Earth Orbit
- LRO instrument ... LEO-LEO Radio Occultation instrument
- MANPl ... Mission Analysis/Planning
- MetOp ... Meteorological Operational satellite
- MPM ... Millimeter-wave Propagation Model
- MSCE ... Mission operations and Satellite Control Element
- MSIS90 ... Mass-Spectrometer-Incoherent-Scatter-1990 atmosphere model
- NASA ... U.S. National Aeronautics and Space Administration
- NASDA ... National Space Development Agency of Japan
- NCAR ... National Center for Atmospheric Research
- NOAA ... U.S. National Oceanic and Atmospheric Administration
- NPOESS ... National Polar-orbiting Operational Environmental Satellite System
- NSF ... U.S. National Science Foundation
- NSPO ... National Space Program Office (Taiwan)
- NWP ... Numerical Weather Prediction
- ONR ... Office of Naval Research
- OSC ... Orbital Sciences Corporation

- OSMod ... Observation System Modeling
  - PAE ... Processing and Archiving Element
  - POD ... Precise Orbit Determination
- RAOB ... Rawinsonde Observation program
  - RMS ... Root Mean Square
  - Rx ... Receiver
  - SAC ... Satélite de Aplicaciones Científicas
- SUNSAT ... Stellenbosch University Satellite
  - TLE ... Two Line Element
- TRSR ... TurboRogue Space Receiver (TRSR-2/3 BlackJack)
  - Tx ... Transmitter
- UCAR ... University Corporation for Atmospheric Research (Boulder, Colorado)
- UNAVCO ... University Navstar Consortium
  - UTC ... Coordinated Universal Time (=GMT)
- UTCSR ... University of Texas Center for Space Research
  - WATS ... Water Vapour and Temperature in the Troposphere and Stratosphere
- WMO ... World Meteorological Organization

# List of Tables

1.1	Atmospheric composition. . . . .	5
2.1	Missions working with GPS/RO receivers. . . . .	18
3.1	LEO-LEO observational requirements. . . . .	50
3.2	GNSS-LEO observational requirements. . . . .	51
4.1	Specification of the parameters for cloud and turbulence scenarios. .	81



# List of Figures

1.1	Vertical structure of the atmosphere. . . . .	7
1.2	Scheme of the general circulation and resulting horizontal structure of the atmosphere. . . . .	9
1.3	Measured changes of the global-mean near surface temperature from 1880–2000 compared with temperature simulations using climate models. . . . .	12
2.1	LEO-LEO occultation geometry. . . . .	20
2.2	An overview of a simple LEO-LEO retrieval processing chain. . . . .	22
3.1	Exemplary global distribution of the vertical-column water vapour content. . . . .	39
3.2	Exemplary vertical distribution of the specific humidity. . . . .	39
3.3	Exemplary ACE+ satellite constellation concept. . . . .	43
3.4	The GRAS-2 instrument. . . . .	44
3.5	General architecture of the LRO instrument. . . . .	45
3.6	Schematic view of the ACE+ observation geometry. . . . .	46
3.7	ACE+ GNSS-LEO occultation event coverage during one day. . . . .	46
3.8	Illustration of the temperature retrieval performance using GNSS-LEO occultation data. . . . .	47
3.9	Atmospheric absorption coefficients as a function of frequency at three different heights. . . . .	48
4.1	Conceptual view of EGOPS5. . . . .	56
4.2	Modular view of EGOPS5. . . . .	57

4.3	Coverage by LEO-LEO occultation events for baseline ACE+ constellation. . . . .	59
4.4	Humidity and temperature profiles for six representative atmospheric cases of the CIRA86aQ_UoG model. . . . .	62
4.5	Atmospheric loss at the tree ACE+ frequencies. . . . .	62
4.6	Carrier-to-noise density ratio ( $C/N_0$ ) profiles for the three ACE+ frequencies. . . . .	64
4.7	Exemplary realizations of thermal amplitude noise profiles for the three ACE+ frequencies. . . . .	64
4.8	Exemplary realizations of 1/f noise profiles for the three ACE+ frequencies. . . . .	65
4.9	Exemplary realizations of linear amplitude drift profiles for the three ACE+ frequencies. . . . .	65
4.10	Exemplary realizations of total instrumental error profiles for the three ACE+ frequencies. . . . .	66
4.11	Schematic view of the LEO-LEO occultation data processing. . . . .	67
4.12	Exemplary transmission retrieval results for the three ACE+ frequencies. . . . .	74
4.13	Exemplary imaginary refractivity retrieval results for the three ACE+ frequencies. . . . .	75
4.14	Exemplary humidity retrieval results for the mid-latitude summer case. . . . .	76
4.15	Exemplary temperature retrieval results for the mid-latitude summer case. . . . .	76
4.16	Flowchart of the performance analysis steps. . . . .	78
4.17	ACE+ LEO-LEO occultation event locations used in the ECMWF simulations. . . . .	83
4.18	Latitude-height cross sections at $0^\circ$ longitude through various ECMWF analysis fields. . . . .	84
4.19	Vertically integrated liquid water density indicating cloud coverage. . . . .	85
5.1	Humidity and temperature retrieval results for the clear-air, non-turbulent tropical scenario. . . . .	90
5.2	Humidity and temperature retrieval results for the clear-air, non-turbulent subtropical summer scenario. . . . .	91

5.3	Humidity and temperature retrieval results for the clear-air, non-turbulent mid-latitude summer scenario. . . . .	92
5.4	Humidity and temperature retrieval results for the clear-air, non-turbulent mid-latitude winter scenario. . . . .	93
5.5	Humidity and temperature retrieval results for the clear-air, non-turbulent high-latitude summer scenario. . . . .	94
5.6	Humidity and temperature retrieval results for the clear-air, non-turbulent high-latitude winter scenario. . . . .	95
5.7	Humidity and temperature retrieval results for the cloudy and turbulent air tropical scenario. . . . .	98
5.8	Humidity and temperature retrieval results for the cloudy and turbulent air subtropical summer scenario. . . . .	99
5.9	Humidity and temperature retrieval results for the cloudy and turbulent air mid-latitude summer scenario. . . . .	100
5.10	Humidity and temperature retrieval results for the cloudy and turbulent air high-latitude summer scenario. . . . .	101
5.11	Humidity and temperature retrieval results for various clear air scenarios computed applying cloudy air retrieval. . . . .	102
5.12	Humidity and temperature retrieval results for the high-latitude clear air scenario. . . . .	106
5.13	Humidity and temperature retrieval results for the high-latitude cloudy air scenario. . . . .	107
5.14	Humidity and temperature retrieval results for the high-latitude cloudy and turbulent air scenario. . . . .	108
5.15	Humidity and temperature retrieval results for the high-latitude cloudy and turbulent air scenario with horizontal variability. . . . .	109
5.16	Humidity and temperature retrieval results for the mid-latitude clear air scenario. . . . .	111
5.17	Humidity and temperature retrieval results for the mid-latitude cloudy air scenario. . . . .	112
5.18	Humidity and temperature retrieval results for the mid-latitude cloudy and turbulent air scenario. . . . .	113
5.19	Humidity and temperature retrieval results for the mid-latitude cloudy and turbulent air scenario with horizontal variability. . . . .	114
5.20	Humidity and temperature retrieval results for the low-latitude clear air scenario. . . . .	116

5.21	Humidity and temperature retrieval results for the low-latitude cloudy air scenario. . . . .	117
5.22	Humidity and temperature retrieval results for the low-latitude cloudy and turbulent air scenario. . . . .	118
5.23	Humidity and temperature retrieval results for the low-latitude cloudy and turbulent air scenario with horizontal variability. . . . .	119
5.24	Retrieval error to background error ratios for retrieved water vapour and temperature profiles. . . . .	122
5.25	Error correlation coefficients between retrieved water vapour and temperature profiles. . . . .	124

# Bibliography

- [Andrews, 2000] Andrews, D. G. (2000). *An Introduction to Atmospheric Physics*. Cambridge Univ. Press, Cambridge, 1st edition.
- [Bauer, 1997] Bauer, M. (1997). *Vermessung und Ortung mit Satelliten*. H. Wichmann Verlag, Heidelberg, 4th edition.
- [Björck, 1996] Björck, A. (1996). *Numerical Methods for Least Squares Problems*. Society for Industrial and Applied Mathematics, Philadelphia.
- [CHAMP, 2004] CHAMP (2004). [http://op.gfz-potsdam.de/champ/index\\_CHAMP.html](http://op.gfz-potsdam.de/champ/index_CHAMP.html) . Internet.
- [COSMIC, 2004] COSMIC (2004). <http://www.cosmic.ucar.edu/> . Internet.
- [Engler et al., 1997] Engler, E. N., N. Zarraoa, W. Mai, and A. Jungstand (1997). *GLONASS – Russian Global Navigation Satellite System*. Deutsche Forschungsanstalt für Luft- und Raumfahrt e.V., Remote Sensing Ground Station Neustrelitz.
- [Eriksson et al., 2001] Eriksson, P., C. Jiménez, D. Murtagh, G. Elgered, T. Kuhn, and S. Bühler (2001). Assessment of uncertainties in LEO-LEO transmission observations through the troposphere/stratosphere. Res. Rpt. 186/2001 ESTEC Contr.No. 15341/01/NL/SF, Chalmers Univ. of Technol., Göteborg, Sweden.
- [ESA, 1998] ESA (1998). Atmospheric Profiling Mission (7th report of Reports for Assessment: The Nine Candidate Earth Explorer Missions). Spec. Publ. ESA SP-1196(7), ESA Publ. Division, Noordwijk, Netherlands. 58 pp.
- [ESA, 2001] ESA (2001). WATS — Water Vapour and Temperature in the Troposphere and Stratosphere (3rd report of Reports for Assessment: The Five Candidate Earth Explorer Core Missions). Spec. Publ. SP-1257(3), ESA Publ. Division, Noordwijk, Netherlands. 98 pp.
- [ESA, 2004a] ESA (2004a). ACE+ — Atmosphere and Climate Explorer (4th report of Reports for Mission Selection: The Six Candidate Earth Explorer Missions). Spec. Publ. ESA SP-1279(4), ESA Publ. Division, Noordwijk, Netherlands. 60 pp.

- [ESA, 2004b] ESA (2004b). ACE+ — Atmosphere and Climate Explorer Technical and Programmatic Annex (4th report of Reports for Mission Selection: The Six Candidate Earth Explorer Missions). Spec. Publ. Annex to ESA SP-1279(4), ESA Publ. Division, Noordwijk, Netherlands. 39 pp.
- [ESA, 2004c] ESA (2004c). ACE+ Atmosphere and Climate Explorer Mission Requirements Document (for Phase A). ESA Doc. No. ESD/ACE+/MRD/001/TW-Issue 2 rev. 1, ESA/ESTEC, Noordwijk, Netherlands. 51 pp.
- [ESA, 2004d] ESA (2004d). Swarm — The Earth's Magnetic Field and Environment Explorers (6th report of Reports for Mission Selection: The Six Candidate Earth Explorer Missions). Spec. Publ. ESA SP-1279(6), ESA Publ. Division, Noordwijk, Netherlands.
- [Eshleman, 1973] Eshleman, V. R. (1973). The radio occultation method for the study of planetary atmospheres. *Planet. Space Sci.*, 21:1521–1531.
- [Feng et al., 2001] Feng, D. D., S. Syndergaard, B. M. Herman, E. R. Kursinski, T. P. Yunck, and F. W. Romberg (2001). Deriving atmospheric water vapour and ozone profiles from active microwave occultation measurements. In H. Fujisada et al., editor, *Sensors, System and Next-Generation Satellites IV*, volume 4169 of *SPIE Proceedings Series*, pages 299–308.
- [Fischbach, 1965] Fischbach, F. F. (1965). A satellite method for pressure and temperature below 24 km. *Bull. Am. Meteorol. Soc.*, 46(9):528–532.
- [Fjeldbo, 1964] Fjeldbo, G. (1964). Bistatic-radar methods for studying planetary ionospheres and surfaces. Sci. Rpt. No. 2, NsG-377, SU-SEL-64-025, Stanford Electronics Laboratories, Stanford, California.
- [Fjeldbo et al., 1971] Fjeldbo, G., A. J. Kliore, and V. R. Eshelman (1971). The Neutral Atmosphere of Venus as Studied with the Mariner V Radio Occultation Experiment. *Astron. J.*, 76:123–140.
- [Fjeldbo and Eshelman, 1965] Fjeldbo, G. and Eshelman, V. R. (1965). The Bistatic Radar-Occultation Method for the Study of Planetary Atmospheres. *J. Geophys. Res.*, 70:3217–3225.
- [Fjeldbo and Eshelman, 1968] Fjeldbo, G. and Eshelman, V. R. (1968). The atmosphere of Mars analyzed by integral inversion of the Mariner IV occultation data. *Planet. Space Sci.*, 16:1035–1059.
- [Foelsche, 1999] Foelsche, U. (1999). Tropospheric water vapor imaging by combination of ground-based and spaceborne GNSS sounding data. Wissenschaftl. Ber. No. 10, Inst. for Meteorol. and Geophys., Univ. of Graz, Austria. Ph. D. thesis.

- [Foelsche and Kirchengast, 2004a] Foelsche, U. and Kirchengast, G. (2004a). Sensitivity of GNSS Occultation Profiles to Horizontal Variability in the Troposphere: A Simulation Study. In G. Kirchengast, U. Foelsche, and A. K. Steiner, editors, *Occultations for Probing Atmosphere and Climate*, pages 127–136, Graz, Austria. Springer-Verlag, Berlin-Heidelberg.
- [Foelsche and Kirchengast, 2004b] Foelsche, U. and Kirchengast, G. (2004b). Sensitivity of GNSS radio occultation data to horizontal variability in the troposphere. *Phys. Chem. Earth*, 29:225–240.
- [Gershenfeld, 2002] Gershenfeld, N. (2002). *The Nature of Mathematical Modeling*. Cambridge Univ. Press, Cambridge, United Kingdom. First published 1999.
- [Gobiet and Kirchengast, 2004] Gobiet, A. and Kirchengast, G. (2004). Advancement of GNSS Radio Occultation Retrieval in the Upper Stratosphere. In G. Kirchengast, U. Foelsche, and A. K. Steiner, editors, *Occultations for Probing Atmosphere and Climate*, pages 137–148, Graz, Austria. Springer-Verlag, Berlin-Heidelberg.
- [Gorbunov, 2002] Gorbunov, M. E. (2002). Canonical transform method for processing GPS radio occultation data in lower troposphere. *Radio Sci.*, 37:9–19–10. doi:10.1029/2000RS002,592.
- [Gorbunov and Kirchengast, 2004] Gorbunov, M. E. and Kirchengast, G. (2004). Processing X/K Band Radio Occultation Data in Presence of Turbulence. Techn. Rpt. for ESA/ESTEC No. 3/2004, Inst. for Geophys., Astrophys., and Meteorol., Univ. of Graz, Austria.
- [GPS/MET, 2004] GPS/MET (2004). <http://www.cosmic.ucar.edu/gpsmet/>. Internet.
- [GRACE, 2004] GRACE (2004). <http://www.csr.utexas.edu/grace/>. Internet.
- [Gradinarsky et al., 2003] Gradinarsky, L. P., P. Eriksson, and G. Elgered (2003). Analysis of the impact of clouds-rain-turbulence. Techn. Rpt. for ESA/ESTEC, Chalmers Univ. of Technol., Göteborg, Sweden. 29 pp.
- [Gurvich and Krasil'nikova, 1990] Gurvich, A. S. and Krasil'nikova, T. G. (1990). Navigation Satellites for Radio Sensing of the Earth's Atmosphere. *Sov. J. Remote Sensing*, 7(6):1124–1131.
- [Häckel, 1999] Häckel, H. (1999). *Meteorologie*. UTB Verlag, Stuttgart, 4th edition.
- [Hajj et al., 2002] Hajj, G. A., E. R. Kursinski, L. J. Romans, W. I. Bertiger, and S. S. Leroy (2002). A technical description of atmospheric sounding by GPS occultation. *J. Atmos. Sol.-Terr. Phys.*, 64:451–469.

- [Hantel, 2001] Hantel, M. (2001). Klimatologie. In Raith, W., editor, *Erde und Planeten*, volume 7 of *Bergmann-Schaefer: Lehrbuch der Experimentalphysik*, chapt. 4, pages 311–426. W de Gruyter Verlag, Berlin-New York, 2nd edition.
- [Harries, 1997] Harries, J. E. (1997). Atmospheric radiation and atmospheric humidity. *Quart. J. Roy. Meteorol. Soc.*, 123:2173–2186.
- [Hedin, 1991] Hedin, A. E. (1991). Extension of the MSIS Thermosphere Model into the Middle and Lower Atmosphere. *J. Geophys. Res.*, 96:1159–1172.
- [Herman et al., 2004] Herman, B., D. Feng, D. Flittner, E. R. Kursinski, S. Syndergaard, and D. Ward (2004). An Overview of the University of Arizona ATOMS Project. In G. Kirchengast, U. Foelsche, and A. K. Steiner, editors, *Occultations for Probing Atmosphere and Climate*, pages 189–200, Graz, Austria. Springer-Verlag, Berlin-Heidelberg.
- [Høeg and Kirchengast, 2002] Høeg, P. and Kirchengast, G. (2002). ACE+ — Atmosphere and Climate Explorer Based on GPS, GALILEO, and LEO-LEO Radio Occultation. Wissenschaftl. Ber. No. 14, Inst. for Geophys., Astrophys., and Meteorol., Univ. of Graz, Austria.
- [Høeg and Leppelmeier, 2000] Høeg, P. and Leppelmeier, G. (2000). ACE — Atmosphere Climate Experiment (ESA Opportunity Missions Proposal 1998). Sci. Rpt. 00–01, Danish Meteorol. Inst., Copenhagen, Denmark.
- [Hofmann-Wellenhof et al., 2001] Hofmann-Wellenhof, B., H. Lichtenegger, and J. Collins (2001). *Global Positioning System. Theory and Practice*. Springer-Verlag, Wien-New York, 5th edition.
- [Houghton et al., 2001] Houghton, J. T., Y. Ding, D. J. Griggs, M. Noguer, P. J. van der Linden, X. Dai, K. Maskell, and C. A. Johnson, editors (2001). *Climate Change 2001: The Scientific Basis. Contribution of Working Group I to the Third Assessment Report of the Intergovernmental Panel on Climate Change*, Cambridge, United Kingdom and New York, USA. IPCC, Cambridge Univ. Press. 881 pp.
- [Jensen et al., 2003] Jensen, A. S., M. Lohmann, H.-H. Benzon, and A. Nielsen (2003). Full spectrum inversion of radio occultation signals. *Radio Sci.*, 38(3):1040.
- [Kertz, 1995] Kertz, W. (1995). *Einführung in die Geophysik I*. Spektrum, Heidelberg-Berlin-Oxford, unchanged reprint of the 1992’s edition.
- [Kirchengast, 1998] Kirchengast, G. (1998). End-to-end Generic Occultation Performance Simulator overview and exemplary applications. Wissenschaftl. Ber. No. 2/1998, Inst. for Meteorol. and Geophys., Univ. of Graz, Austria.

- [Kirchengast, 2004] Kirchengast, G. (2004). Occultations for Probing Atmosphere and Climate: Setting the Scene. In G. Kirchengast, U. Foelsche, and A. K. Steiner, editors, *Occultations for Probing Atmosphere and Climate*, pages 1–8, Graz, Austria. Springer-Verlag, Berlin-Heidelberg.
- [Kirchengast and Høeg, 2004] Kirchengast, G. and Høeg, P. (2004). The ACE+ Mission: An Atmosphere and Climate Explorer Based on GPS, GALILEO, and LEO-LEO Radio Occultation. In G. Kirchengast, U. Foelsche, and A. K. Steiner, editors, *Occultations for Probing Atmosphere and Climate*, pages 201–220, Graz, Austria. Springer-Verlag, Berlin-Heidelberg.
- [Kirchengast et al., 1999] Kirchengast, G., J. Hafner, and W. Poetzi (1999). The CIRA86aQ\_UoG model: An extension of the CIRA-86 monthly tables including humidity tables and Fortran95 global moist air climatology model. Tech. Rpt. for ESA/ESTEC No. 8/1999, Inst. for Meteorol. and Geophys., Univ. of Graz, Austria. 18 pp.
- [Kirchengast et al., 2002a] Kirchengast, G., J. M. Fritzer, and J. Ramsauer (2002a). End-to-end GNSS Occultation Performance Simulator Version 4 (EGOPS4) Software User Manual (Overview and Reference Manual). Techn. Rpt. for ESA/ESTEC No. 3/2002, Inst. for Geophys., Astrophys., and Meteorol., Univ. of Graz, Austria. 472 pp.
- [Kirchengast et al., 2004a] Kirchengast, G., J. M. Fritzer, M. Schwärz, S. Schweitzer, and L. Kornblueh (2004a). The Atmosphere and Climate Explorer Mission ACE+: Scientific Algorithms and Performance Overview. Techn. Rpt. for ESA/ESTEC No. 2/2004, Inst. for Geophys., Astrophys., and Meteorol., Univ. of Graz, Austria.
- [Kirchengast et al., 1998] Kirchengast, G., M. Gorbunov, N. Jakowski, L. Kornblueh, U. Mallow, A. Rius, C. Rocken, M. Rothacher, G. Schmidtke, M. Sust, J. Ward, and A. Wernik (1998). ACLISCOPE — Atmosphere and Climate Sensors Constellation Performance Explorer (ESA Opportunity Mission Proposal 1998). Wissenschaftl. Ber. No. 4/1998, Inst. for Meteorol. and Geophys., Univ. of Graz, Austria. 60 pp.
- [Kirchengast et al., 2002b] Kirchengast, G., P. Hoeg, G. Elgered, S. Buehler, and others (2002b). ESA-ACEPASS: ACE+ Phase A Scientific Support Study on LEO-LEO Occultation Characterization. Proposal to ESA in Response to RFQ/3-10471/02/NL/FF 123445, Inst. for Geophys., Astrophys., and Meteorol., Univ. of Graz, Austria. 67 pp.
- [Kirchengast et al., 2004b] Kirchengast, G., S. Schweitzer, J. Ramsauer, J. M. Fritzer, and M. Schwärz (2004b). Atmospheric Profiles Retrieved from ACE+ LEO-LEO Occultation Data: Statistical Performance Analysis using Geometric Optics Processing. Techn. Rpt. for ESA/ESTEC No. 1/2004, Inst. for Geophys., Astrophys., and Meteorol., Univ. of Graz, Austria.

- [Kliore et al., 1975] Kliore, A. J., G. Fjeldbo, B. L. Seidel, D. N. Sweetnam, T. T. Sesplaukis, P. M. Woiceshyn, and S. I. Rasool (1975). The Atmosphere of Io from Pioneer 10 Radio Occultation Measurements. *Icarus*, 24:407–410.
- [Kliore et al., 1964] Kliore, A. J., T. W. Hamilton, and D. L. Cain (1964). Determination of some physical properties of the atmosphere of Mars from changes in the Doppler signal in a spacecraft on an earth occultation trajectory. Techn. Rpt. 32-674, JPL, Pasadena, CA.
- [Kraus, 2000] Kraus, H. (2000). *Die Atmosphäre der Erde. Eine Einführung in die Meteorologie*. Vieweg Verlag, Braunschweig/Wiesbaden.
- [Kuhn, 2003] Kuhn, T. (2003). TurbScintModel - the EGOPS scintillation model for LEO-LEO occultations. Draft Rpt. to ESA/ESTEC Oct. 2003, IEP, Univ. of Bremen, Germany. 22 pp.
- [Kursinski et al., 2004] Kursinski, E. R., D. Feng, D. Flittner, G. Hajj, B. Herman, F. Romberg, S. Syndergaard, D. Ward, and T. Yunck (2004). An Active Microwave Limb Sounder for Profiling Water Vapour, Ozone, Temperature, Geopotential, Clouds, Isotopes and Stratospheric Winds. In G. Kirchengast, U. Foelsche, and A. K. Steiner, editors, *Occultations for Probing Atmosphere and Climate*, pages 173–187, Graz, Austria. Springer-Verlag, Berlin-Heidelberg.
- [Kursinski et al., 1997] Kursinski, E. R., G. A. Hajj, J. T. Schofield, R. P. Linfield, and K. R. Hardy (1997). Observing Earth's atmosphere with radio occultation measurements using the Global Positioning System. *J. Geophys. Res.*, 102:23429–23465.
- [Kursinski et al., 2000] Kursinski, E. R., G. A. Hajj, S. S. Leroy, and B. Herman (2000). The GPS Radio Occultation Technique. *Terr., Atmos. and Oceanic Sci.*, 11(1):53–114.
- [Kursinski et al., 2002] Kursinski, E. R., S. Syndergaard, D. Flittner, D. Feng, G. Hajj, B. Herman, D. Ward, and T. Yunck (2002). A Microwave Occultation Observing System to Characterize Atmospheric Water, Temperature, and Geopotential via Absorption. *J. Atmos. Oceanic Technol.*, 19:1897–1914.
- [Landolt-Börnstein, 1984] Landolt-Börnstein (1984). Geophysics of the Solid Earth, the Moon and the Planets — Numerical Data and Functional Relationships. In K. Fuchs and H. Stoffel, editors, *Science and Technology*, volume V/2a, pages 332–336. Springer-Verlag, Berlin-Heidelberg.
- [Lee et al., 2001] Lee, L.-C., C. Rocken, and R. Kursinski, editors (2001). *Applications of Constellation Observing System for Meteorology, Ionosphere and Climate*. Springer-Verlag, Hong Kong. 384 pp.
- [Leick, 1995] Leick, A. (1995). *GPS Satellite Surveying*. Wiley, New York, 2nd edition.

- [Leroy, 2001] Leroy, S. (2001). Amplitude of an occultation signal in three dimensions. Unpublished.
- [Liebe et al., 1993] Liebe, H. J., G. Hufford, and M. Cotton (1993). Propagation modeling of moist air and suspended water/ice particles at frequencies below 1000 GHz. In *52nd Specialists Meeting of the Electromagnetic Wave Propagation Panel*, page 542. AGARD.
- [Liljequist and Cehak, 1984] Liljequist, G. H. and Cehak, K. (1984). *Allgemeine Meteorologie*. Vieweg Verlag, Braunschweig, 3rd edition.
- [Lindal, 1992] Lindal, G. F. (1992). The Atmosphere of Neptune: An Analysis of Radio Occultation Data Acquired with Voyager 2. *Astron. J.*, 103(3):967–982.
- [Lindal et al., 1983] Lindal, G. F., G. E. Wood, H. Hotz, D. N. Sweetnam, V. R. Eshleman, and G. L. Tyler (1983). The Atmosphere of Titan: An Analysis of the Voyager 1 Radio Occultation Measurements. *Icarus*, 53(2):348–363.
- [Lindal et al., 1987] Lindal, G. F., J. R. Lyons, D. N. Sweetnam, V. R. Eshleman, D. P. Hinson, and G. L. Tyler (1987). The atmosphere of Uranus: Results of radio occultation measurements with Voyager 2. *J. Geophys. Res.*, 92:14987–15001.
- [Lusignan et al., 1969] Lusignan, B., G. Modrell, A. Morrison, J. Pomalaza, and S. G. Ungar (1969). Sensing the Earth’s Atmosphere with Occultation Satellites. *Proc. IEEE*, 57(4):458–467.
- [Marouf et al., 1986] Marouf, E. A., G. J. Tyler, and P. A. Rosen (1986). Profiling Saturn’s rings by radio occultation. *Icarus*, 68:120–166.
- [Melbourne et al., 1994] Melbourne, W. G., E. S. Davis, C. B. Duncan, G. A. Hajj, K. Hardy, E. R. Kursinski, T. K. Meehan, L. E. Young, and T. P. Yunck (1994). The Application of Spaceborne GPS to Atmospheric Limb Sounding and Global Change Monitoring. Publ. 94–18, JPL, Pasadena, CA. 147 pp.
- [Melbourne et al., 1988] Melbourne, W. G., T. P. Yunck, L. E. Young, B. H. Hager, G. F. Lindal, C. H. Liu, and G. H. Born (1988). GPS Geoscience Instrument for EOS and space station. Proposal to NASA AO OSSA-1-88, 81 (GGI proposal), JPL, Pasadena, CA. 147 pp.
- [METOP, 2004] METOP (2004). <http://www.esa.int/export/esaME/index.html> . Internet.
- [Nielsen et al., 2003] Nielsen, A. S., M. S. Lohmann, P. Høeg, H.-H. Benzon, A. S. Jensen, T. Kuhn, C. Melsheimer, S. A. Buehler, P. Eriksson, L. Gradinarsky, C. Jiménez, and G. Elgered (2003). Characterization of ACE+ LEO-LEO Radio Occultation Measurements. Contr.No. 16743/02/NL/FF, ESTEC.

- [ØRSTED, 2004] ØRSTED (2004). <http://web.dmi.dk/fsweb/projects/oersted/homepage.html> . Internet.
- [Phinney and Anderson, 1968] Phinney, R. A. and Anderson, D. L. (1968). On the radio occultation method for studying planetary atmospheres. *J. Geophys. Res.*, 73:1819–1827.
- [Reuter, 2001] Reuter, H. (2001). Meteorologie. In Raith, W., editor, *Erde und Planeten*, volume 7 of *Bergmann-Schaefer: Lehrbuch der Experimentalphysik*, chapt. 3, pages 131–310. W de Gruyter Verlag, Berlin-New York, 2nd edition.
- [Rocken et al., 1997] Rocken, C., R. Anthes, M. Exner, D. Hunt, S. Sokolovsky, R. Ware, M. Gorbunov, W. Schreiner, D. Feng, B. Hermann, Y.-H. Kuo, and X. Zou (1997). Analysis and Validation of GPS/MET Data in the Neutral Atmosphere. *J. Geophys. Res.*, 102:29849–29860.
- [Rodgers, 2000] Rodgers, C. D. (2000). *Inverse Methods for Atmospheric Sounding: Theory and Practice*, volume 2 of *Series on Atmospheric, Oceanic and Planetary Physics*. World Scientific Publishing, Singapore.
- [Roedel, 2000] Roedel, W. (2000). *Physik unserer Umwelt: Die Atmosphäre*. Springer-Verlag, Berlin-Heidelberg, 3rd edition.
- [Salby, 1996] Salby, M. L. (1996). *Fundamentals of Atmospheric Physics*. Academic Press, San Diego.
- [Schanda, 1986] Schanda, E. (1986). *Physical Fundamentals of Remote Sensing*. Springer-Verlag, Berlin-Heidelberg.
- [Schönwiese, 2003] Schönwiese, C. D. (2003). *Klimatologie*. UTB Verlag, Stuttgart, 2nd edition.
- [Schweitzer et al., 2003] Schweitzer, S., G. Kirchengast, J. Ramsauer, and M. Schwärz (2003). Atmospheric Profiles Retrieved from ACE+ LEO-LEO Occultation Data: Performance Analysis for Instrumental Errors using Geometric Optics Processing. Techn. Rpt. for ESA/ESTEC No. 2/2003, Inst. for Geophys., Astrophys. and Meteorol., Univ. of Graz, Austria. 76 pp.
- [Sokolovskiy, 2000] Sokolovskiy, S. V. (2000). Inversions of radio occultation amplitude data. *Radio Sci.*, 35(1):97–105.
- [Sokolovskiy, 2004] Sokolovskiy, S. V. (2004). Effect of superrefraction on inversions of radio occultation signals in the lower troposphere. *Radio Sci.*, 38(3):Art. No. 1058.
- [Steiner, 1998] Steiner, A. K. (1998). High-resolution sounding of key climate variables using the radio occultation technique. Wissenschaftl. Ber. No. 3/1998, Inst. for Meteorol. and Geophys., Univ. of Graz, Austria. Ph. D. thesis.

- [Steiner et al., 1999] Steiner, A. K., G. Kirchengast, and H. P. Ladreiter (1999). Inversion, error analysis, and validation of GPS/MET occultation data. *Ann. Geophys.*, 17:122–138.
- [Steiner et al., 2001] Steiner, A. K., G. Kirchengast, U. Foelsche, L. Kornblueh, E. Manzini, and L. Bengtsson (2001). GNSS Occultation Sounding for Climate Monitoring. *Phys. Chem. Earth (A)*, 26(3):113–124.
- [Steiner and Kirchengast, 2004] Steiner, A. K. and Kirchengast, G. (2004). Ensemble-Based Analysis of Errors in Atmospheric Profiles Retrieved from GNSS Occultation Data. In G. Kirchengast, U. Foelsche, and A. K. Steiner, editors, *Occultations for Probing Atmosphere and Climate*, pages 149–160, Graz, Austria. Springer-Verlag, Berlin-Heidelberg.
- [Syndergaard, 1998] Syndergaard, S. (1998). Modeling the impact of the Earth’s oblateness on the retrieval of temperature and pressure profiles from limb sounding. *J. Atmos. Terr. Phys.*, 60:171–180.
- [Syndergaard, 1999] Syndergaard, S. (1999). Retrieval Analysis and Methodologies in Atmospheric Limb Sounding Using the GNSS Radio Occultation Technique. Sci. Rpt. 99–6, Danish Meteorol. Inst., Copenhagen.
- [Thompson, 1998] Thompson, R. D. (1998). *Atmospheric Processes and Systems*. Routledge, London-New York.
- [Tyler, 1987] Tyler, G. J. (1987). Radio propagation experiments in the outer solar system with Voyager. *Proc. IEEE*, 75(10):1404–1431.
- [von Storch, H. et al., 1999] von Storch, H., S. Güss, and M. Heimann (1999). *Das Klimasystem und seine Modellierung. Eine Einführung*. Springer-Verlag, Berlin-Heidelberg-New York.
- [Vorob’ev and Krasnil’nikova, 1994] Vorob’ev, V. V. and Krasnil’nikova, T. G. (1994). Estimation of the accuracy of the atmospheric refractive index recovery from Doppler shift measurements at frequencies used in the NAVSTAR system. *Phys. of Atmos. and Oceans.*, 29:602–609.
- [Wickert, 2004] Wickert, J. (2004). The radio occultation experiment aboard champ: Operational data analysis and validation of vertical atmospheric profiles. *J. Met. Soc. Japan*, 82(1B):381–395.
- [Yakovlev et al., 1991] Yakovlev, O. I., S. S. Matyugov, and V. N. Gubenko (1991). Verena-15 and -16 middle atmosphere profiles from radio occultations: Polar and near-polar atmosphere of Venus. *Icarus*, 94:493–510.
- [Yunck et al., 2000] Yunck, T. P., Chao-Han L., and R. Ware (2000). A History of GPS Sounding. *Terr., Atmos. and Oceanic Sci.*, 11(1):1–20.